ULB FACULTÉ DES SCIENCES

UNIVERSITÉ LIBRE DE BRUXELLES

Search for dark matter from the centre of the Earth with ten years of IceCube data

Thesis presented by Giovanni RENZI

in fulfilment of the requirements of the PhD Degree in physical science ("Docteur en sciences physiques")

Année académique 2022-2023

Supervisor: Professor Juan Antonio AGUILAR SÁNCHEZ

Inter-University Institute For High Energies

Thesis jury:

Barbara CLERBAUX (Université Libre de Bruxelles, Chair)
Laura LOPEZ HONOREZ (Université Libre de Bruxelles, Secretary)
Krijn DE VRIES (Vrije Universiteit Brussel)
Carlos PÉREZ DE LOS HEROS (Uppsala Universitet)
Juan de Dios ZORNOZA GÓMEZ (Universitat de València)

ABSTRACT

While experimental evidence for the presence of dark matter, one of the main components of the Universe, has strengthened for over a century, its nature yet remains unknown. Some models predict that dark matter is made up of particles which interact only weakly with the Standard Model. This connection with the Standard Model, albeit weak, opens the possibility of detecting dark matter with different experimental techniques. Neutrino telescopes, such as the one-cubic-kilometre IceCube Neutrino Observatory at the South Pole, can detect neutrinos produced in dark matter self-annihilation or decay towards Standard Model particles as secondary products of these interactions. In particular, dark matter particles can scatter off nuclei of celestial bodies, lose velocity and become gravitationally trapped in the centre of these bodies, such as the Earth. The accumulation of dark matter in the centre of the Earth would induce dark matter self-annihilation into Standard Model pairs of quarks or leptons which would lead to a flux of neutrinos that might be observed from the South Pole by IceCube.

This work presents an analysis of the search for dark matter from the centre of the Earth with ten years of IceCube data. The development of a dedicated event selection which relies heavily on Monte-Carlo simulations has been necessary to address the unique position in local coordinates of the centre of the Earth. The selection was split into two distinct low- and high-energy parts due to differences in the signal signatures at different dark matter masses. Using the zenith angle and energy distributions of data as observables, a 2D statistical analysis based on a method of maximisation of the Poisson likelihood has been developed and performed. As no significant neutrino excess was found, upper limits were set on the spin-independent dark matter-nucleon scattering cross-section $\sigma^{\mathrm{SI}}_{\chi N}$. Limits were also set on the coupling constants for the effective field theory of dark matter. $\sigma^{\mathrm{SI}}_{\chi N}$ limits show a significant improvement compared to the previous one-year search and the world's best limits for the Earth at dark matter masses $m_\chi > 100$ GeV.

RÉSUMÉ

Recherche de matière noire au centre de la Terre avec dix ans de données de IceCube

Alors que les preuves expérimentales de la présence de la matière noire, l'un des principaux composants de l'Univers, se sont renforcées depuis plus d'un siècle, sa nature reste encore inconnue. Certains modèles prédisent que la matière noire est composée de particules qui n'interagissent que faiblement avec le modèle standard. Cette interaction avec le Modèle Standard, bien que faible, ouvre la possibilité de détecter la matière noire par le biais de différentes techniques expérimentales. Les télescopes à neutrinos, tels que l'observatoire à neutrinos IceCube qui mesure un kilomètre cube et est situé au pôle Sud, peuvent détecter les neutrinos produits en tant que particules secondaires lors de l'auto-annihilation de la matière noire ou sa désintégration en particules du Modèle Standard. En particulier, les particules de matière noire peuvent être diffusées par les noyaux des molécules de corps célestes (tel que la Terre), perdre leur vitesse et être piégées gravitationnellement au centre de ces corps. L'accumulation de matière noire au centre de la Terre pourrait induire l'auto-annihilation de cette matière noire en paires de quarks ou de leptons du modèle standard, ce qui entraînerait un flux de neutrinos qui pourrait être observé par IceCube depuis le Pôle Sud.

Ce travail présente une analyse de la recherche de matière noire au centre de la Terre avec dix ans de données d'IceCube. Le développement d'une sélection d'événements dédiée qui s'appuie fortement sur des simulations Monte-Carlo a été nécessaire pour prendre en compte la position unique du centre de la Terre en coordonnées locales. La sélection a été divisée en deux parties distinctes, l'une à basse énergie et l'autre à haute énergie, en raison des différences de signatures du signal à différentes masses de matière noire. En utilisant comme observables les distributions d'angle zénithal et d'énergie des données, une analyse statistique 2D basée sur la méthode de maximum de vraisemblance de Poisson a été développée et mise en place. Comme aucun excès significatif de neutrinos n'a été observé , des limites supérieures sur la section efficace de diffusion

matière noire-nucléon indépendante du spin $\sigma^{\mathrm{SI}}_{\chi N}$ ont été fixées. Des limites ont également été fixées pour les constantes de couplage de la théorie efficace des champs de la matière noire. Les limites $\sigma^{\mathrm{SI}}_{\chi N}$ montrent une amélioration notable en comparaison avec la recherche précédente exploitant un an de données, ainsi que les meilleures limites mondiales pour le centre de la Terre pour les énergies $E > 100$ GeV.

ACKNOWLEDGEMENTS

When I decided to apply for this PhD five years ago, I simply could not know the amazing journey I was about to embark on. This work, along with my entire stay in Belgium, was an endless surprise, which could not have been possible without all the wonderful people I met on this journey.

Firstly, I would like to thank Juanan for his support and patience. You made me feel at home and at ease from the very beginning and throughout these years. Our meetings were a precious help to give order to ideas and priorities. Your guidance and attention to detail have been certainly crucial for this accomplishment. I would like to thank all the jury members for accepting this task and for actually being part, in one way or another, of the path that led me to this moment. In particular, I would like to express my gratitude to Barbara and Laura for their involvement over the last four years.

To all the colleagues with whom I shared these years at the IIHE, but also at conferences and sometimes just for a beer: thank you! You made work a pleasure. A particular acknowledgement goes to Chris, for introducing me to the wonderful world of the IceCube software, to Sebastian for his precious contribution always given with contagious enthusiasm, and to Nadège for basically everything, especially for the support and advice in the very last months.

A special thank you goes to all the friends, or better say, brothers, with whom I shared a home over the past five years. Because of the presence of Sebastian, Francesco and Nicola I can say that even the tough times of lockdown have been a memory I will always carry in my heart. A big thank you also goes to Michał: sharing the time when we both were writing our theses made it all much lighter. Muchas gracias también a tí, Daniel, por tu alegría. Je veux aussi remercier tout les frères et sœrs que j'ai trouvé à Bruxelles, qui m'ont fait sentir partie d'une famille dès le premier jour.

Grazie alla mia famiglia, e in special modo alla mia mamma, per essermi stati vicino nei momenti più importanti e nei momenti più bui. Un grazie va, di dovere, alla mia sorellina Alessia Maria per il preziosissimo contributo grafico. Grazie anche a tutti gli amici a Roma per l'appoggio o anche solo per una risata

o una chiacchierata condivisa.

The whole IceCube collaboration certainly deserves my acknowledgement, too, for creating a friendly and supportive environment, which made working within the collaboration much easier. It is indeed true that ”we made the impossible look easy”! A particular mention goes to Dima and Alex for their precious review work.

I must give the final thanks to God, who lighted the way and was by my side all along and without whom none of this would have been possible at all for me.

God, my Lord, is my strength;
he makes my feet swift as those of hinds
and enables me to go upon the heights
Hab 3,19

CONTENTS

LIST OF FIGURES

LIST OF TABLES

LIST OF ABBREVIATIONS

BDT - Boosted decision tree
CC - Charged current
C.L. - Confidence level
CMB - Cosmic Microwave Background
DIS - Deep-inelastic scattering
DM - Dark matter
DOM - Digital Optical Module
dSphs - Dwarf spheroidal galaxies
EFT - Effective field theory
GC - Galactic centre
HE - High energy
HESE - High Energy Starting Tracks
KDE - Kernel Density Estimation
KK - Kaluza-Klein
LE - Low energy
LHC - Large Hadron Collider
LSP - Lightest Kaluza-Klein particle
LSP - Lightest supersymmetric particle
MSSM - Minimal Supersymmetric Standard Model
MSW - Mikheyev-Smirnov-Wolfenstein
NC - Neutral current
NMH - Neutrino Mass Hierarchy
PBH - Primordial black hole
PDF - Probability density function
PMNS - Pontecorvo-Maki-Nakagawa-Sakata
PMT - Photo-multiplier tube
SHM - Standard Halo Model
SM - Standard Model
SUSY - Supersymmetry
UHECR - Ultra-high-energy cosmic rays

WIMP - Weaky Interacting Massive Particle
Λ**-CDM** - Lambda Cold Dark Matter

INTRODUCTION

Cosmological measurements and astronomical observations provide evidence of the existence of a large ($\sim 22\%$) massive component of the Universe interacting almost exclusively via gravitation. Since the first hints of its existence were observed in the Coma cluster by R. Zwicky in 1933, physicists -theoreticians and experimentalists alike- have embarked on the quest to unravel this mystery. *Dark matter* is generally thought to be made of particles, though other interpretations invoking modifications to gravity cannot be excluded yet. *Weakly Interacting Massive Particles* are one of the most relevant dark matter candidates and these particles have been extensively sought after through the last decades. However, their discovery remains elusive. Signatures of particle dark matter can be obtained via indirect detection, direct detection and production at colliders. Indirect detection aims at detecting the products of dark matter self-annihilation or decay. Direct detection, on the other hand, focuses on observing the scattering of dark matter particles off Standard Model particles. Finally, dark matter can be produced at large particle colliders and detected as some form of missing energy in the observation of these collisions. The current astronomical observations indicate that dark matter forms halos surrounding galaxies, like the Milky Way, and extends radially up to $\sim$100 000 light-years. At the solar system level, the distribution of galactic dark matter opens the possibility for dark matter particles to scatter off Standard Model particles in the vicinity of a massive celestial body such as the Sun or the Earth, lose velocity and gravitationally fall towards the centre of the object where an overdensity of dark matter will be generated. This thesis is focused on the search for a dark matter signature coming from the centre of the Earth. Accumulated dark matter in the centre of the Earth will trigger the process of dark matter particles self-annihilation into Standard Model particles, among which neutrinos will be emitted both as primary or secondary products of the interactions. Because of their peculiar properties and, in particular, their extreme elusiveness, neutrinos can travel through the Earth up to the surface and be detected by large neutrino telescopes such as the IceCube detector.

The IceCube Neutrino Observatory is an experiment based at the geographical South Pole that can detect neutrinos interacting in, or in proximity to its one-cubic-kilometre volume via observation of the so-called *Cherenkov effect*. IceCube was the first experiment to detect a flux of neutrinos originating in astrophysical phenomena and has provided world-leading constraints on the atmospheric neutrino oscillations parameters. While not being its primary purpose, IceCube has been involved in the search for dark matter since its beginnings with very competitive results in the field of indirect detection of dark matter.

In the context of this work, an IceCube selection of events has been developed by

selecting events appearing as quasi-vertical and up-going. The particular local direction of the signal does not allow for estimating the background from right-ascension scrambling of the real data as it is usually done in neutrino telescopes, hence, we had to rely on Monte-Carlo simulations. The main background I had to filter out was the muons generated in cosmic ray interactions in the Earth's atmosphere. Though these muons are down-going (they cannot traverse the Earth), a large fraction of them are mis-reconstructed as up-going. A machine learning algorithm helped to discriminate efficiently down-going muons from up-going neutrinos. At the last stage of the selection, when muons constitute only $\sim 10\%$ of the total of the events, neutrinos originated in the cosmic ray interactions in the atmosphere and that have traversed the Earth remain as the dominant background. These background characteristics make it indistinguishable from the dark matter signal. However, the distribution of the zenith angle and energy can be used to discriminate the atmospheric background from a possible dark matter signature. Neutrinos coming from dark matter annihilation cannot have energy larger than the dark matter particle mass and they have their direction close to the vertical at zenith angles $\theta \sim 180^{\circ}$.

A binned Poisson likelihood maximization analysis has been developed. The probability density functions (PDFs) for this analysis use the 2D zenith angle-energy distributions for background and different signal models estimated with simulations after the whole event selection chain. A series of nuisance parameters in the likelihood formulation and a study of possible systematic effects were implemented in order to reduce the effect of the *unknown* uncertainties in the simulation.

This introduction is followed by the structure of this thesis presentation. Chapter 1 is a review of the current dark matter theoretical and experimental state-of-art. Chapter 2 aims at presenting the characteristics of neutrinos and their detection in big instrumented water volumes, such as IceCube. The latter will be presented, from a technical and scientific point of view in Chapter 3. The event selection and analysis method I developed for the search for dark matter from the centre of the Earth will be described in Chapters 4 and 5, respectively. Finally, the results obtained with the work prepared in the previous chapters will be presented in Chapter 6.

CHAPTER 1

DARK MATTER

There's a sign on the wall, but she wants to be sure
Cause, you know, sometimes words have two meanings[117]

Dark matter (DM) is one of the most intriguing unresolved puzzles in modern physics. Strong evidence for its existence has arisen throughout the last century from astronomical and cosmological observations, yet its nature remains unknown.
The dynamics of observed galaxies and galaxy clusters show gravitational fields that cannot be described by their visible content only. Instead, observations seem to suggest the presence of an invisible mass component, where the average total mass of these objects is estimated to be hundreds of times larger than the visible mass. The currently most accepted cosmological model, extraordinarily probed by the study of the Cosmic Microwave Background (CMB), implies dark matter constitutes $\sim 85\%$ of the total matter content of the Universe and $\sim 22\%$ of the Universe composition [30].

A variety of models propose a dark matter component made of new beyond the Standard Model particles. Most of these models explain the relic abundance of dark matter via thermal production which requires that these particles have weak coupling with the Standard Model (SM). Starting from simple extensions of the SM, new stable particles have been postulated such as neutralinos and axions. The former would arise from supersymmetric (SUSY) extensions of the SM, while the latter is a hypothesised particle that would explain the so-called *strong CP problem*. Other particle candidates have also been considered, such as the SM neutrino and its theorised counterpart, the sterile neutrino. Dark matter could also, to some extent, be composed of baryonic matter or other macroscopic objects that could account for a part of the missing matter in the Universe.

The connection of DM with SM opens the possibility of detecting DM via the emission of cosmic rays, gamma-rays, and neutrinos. Looking for an excess of these messengers from regions with an over-density of DM is the strategy followed by the so-called *indirect detection* of dark matter.

The following sections of this chapter will develop the subjects introduced above.

The evidence for dark matter will be presented in section 1.1. The cosmological model and the latest measurements of the Cosmic Microwave Background (CMB) will be discussed in section 1.2. Section 1.3 will expose the currently most valid DM candidates. The distribution of DM in the Universe and the Milky Way, in particular, will be presented in section 1.4. DM interactions, and in particular its capturing at the centre of the Earth, will be discussed in section 1.5. Finally, an overview of the latest DM experimental results will be given in section 1.6.

1.1 Evidence for dark matter

Relevant evidence for the existence of dark matter comes from the estimation of the mass of galaxies and galaxy clusters. These estimations show that the mass content of these objects is far larger than their luminous mass (i.e. the mass of the stars). Such observations can be obtained by measuring the distribution of the rotational velocity depending on the distance from the centre of gravity or by observing the gravitational lensing effect (see below) on objects at nearby angles. Strong evidence for DM also comes from the observation of the Cosmic Microwave Background. Its small temperature anisotropies are a powerful tool for measuring the amount of DM in the Universe. The Planck CMB mission provided outstanding results on the CMB anisotropies. More details on this evidence will be given in 1.2.

1.1.1 Gravitational lensing

Before entering the details of the mass deficit observations, it is important to explain how matter is estimated in astronomical observations. One of the most interesting predictions of general relativity is the effect of *gravitational lensing* [128]. The gravitational field of a massive object curves the trajectory of the photons passing through the field. As a consequence, background objects appear deformed or displaced, as if they were passing through an optical lens.

For a cylindrical symmetrical gravitational potential, the deflection angle for a photon incoming at a distance b from the centre of gravity of the lens can be expressed as [128]:

$$\alpha = \frac{4GM(b)}{bc^2}, \tag{1.1}$$

where G is the gravitational constant and $M(b)$ is the mass in a sphere of radius b. Therefore, the deflection is proportional to the mass of the lens object.

A fascinating effect can be seen in the case where the source, the lens, and the observer are perfectly aligned. A so-called *Einstein ring* is formed: the background galaxy appears as a ring around the lens. Perfect Einstein rings are rare due to the extreme precision of the needed alignment while, more often, background galaxies appear displaced or distorted in shape. When the deflection is significantly large and two or more images of the background object can be observed the effect is called *strong lensing*. The latter is opposed to the more frequent *weak lensing* when background objects appeared sheared and distorted.

Another relevant lensing effect, called *microlensing*, can be observed in the Milky Way. Considering a compact massive object as a point-like lens, the flux of a background

Figure 1.1 – Deep field image from the James Webb Telescope. The effects of gravitational lensing are visible in multiple arcs and distorted objects.

star will be amplified compared to the flux expected without lensing: stray light will be curved towards the observer during the passage of the compact object. Microlensing has been used to search for dark massive compact objects as an explanation of dark matter.

Gravitational lensing is, hence, a valuable tool for estimating the mass of cosmological objects such as galaxy clusters and galaxies in the search for dark matter.

1.1.2 Galaxy clusters

Galaxy clusters are groups of gravitationally bound galaxies. The largest known objects of this type can contain as many as thousands of galaxies. The estimation of their mass provides compelling evidence for the presence of non-baryonic mass [128].

The first observation of a large mass-to-light ratio in galaxy clusters comes from the study of the velocity dispersion in the Coma cluster by R. Zwicky [149] in 1933. The mass-to-light ratio is the ratio between the estimated mass of an object and its luminosity. Using the Sun as a baseline of $M_\odot/L_\odot = 1$, larger values than one indicate that the mass of these objects does not reside on stars but in some form of dark matter.

To estimate the velocity dispersion of the Coma cluster, R. Zwicky used the virial theorem. Under dynamic equilibrium, the virial theorem is valid and can be written in the form:

$$\langle T \rangle = -\frac{1}{2}\langle U \rangle, \tag{1.2}$$

being T and U the kinetic and potential energies of the system, respectively. For a galaxy

orbiting the centre of gravity of a cluster at a distance r with velocity $v(r)$, Eq. (1.2) translates into:

$$v^2(r) = \frac{M(r)G}{r}, \tag{1.3}$$

where G is the gravitational constant and $M(r)$ is the cluster mass included in a radius r from the centre.
For the Coma cluster, the measured velocity dispersion implied a far bigger mass content than the one supposed by light observations. Zwicky's study alone, updated with the current estimations of the Hubble constant value, indicates a mass-to-light ratio $M/L \sim 60$, meaning that the mass of the cluster galaxies is far beyond the mass which can be inferred from visible stars.

In modern days, the baryonic content of a cluster mass can be estimated via X-ray observations of the temperature of the gas component of the cluster. The total mass of a galaxy cluster is either assessed by the measure of the velocity dispersion of the galaxies, by the X-ray temperature, or by gravitational lensing. Searches led to the result [128]:

$$\frac{M_{\rm baryons}}{M_{\rm total}} \sim 0.16 h_0^{-3/2} \simeq 1/6. \tag{1.4}$$

where $h_0 = H_0/100$ km/s/Mpc is the dimensionless Hubble parameter. This measurement represents strong evidence that galaxy clusters are embedded in a DM halo.

Bullet cluster

Striking evidence of the existence of dark matter is the so-called *Bullet cluster* [67] . The system really consists of two galaxy clusters, the sub-cluster (1E 0657-558) which collided with the main cluster (1E 0657-56) at redshift $z = 0.296$ [139]. In a collision between clusters, their galaxies, having a small cross-section and interacting via the gravitational force only, are not affected by the collision, so the galaxy components of the clusters remain unaltered and pass through each other. In the gas of the inter-cluster medium ionised particles are subject to electromagnetic interactions and are slowed down. Fig. 1.2 shows the optical (galaxies) and X-ray (tracing the gas component) observations of the system, along with the gravitational contours obtained via weak gravitational lensing computations. The X-ray picture shows how the gas clouds of the clusters have been "left behind" by the galaxies. An important characteristic of this system is the high mass-to-light ratio. In an only baryonic model, the majority of the mass should, thus, reside in the gas clouds. The gravitational contours in fig. 1.2 show however that the mass is rather concentrated in the regions where the galaxies are, after having passed without interacting through the gravitational potential of the other cluster favouring the idea that a third component made up of dark matter also went through unaffected by the collision. The observation of the bullet cluster is, hence, a strong, "photographic" indication of the presence of DM halos as the main matter component of clusters.

1.1.3 Galaxies

Apart from the large clusters of galaxies, individual galaxies also hint at the presence of dark matter based on the estimation of their masses. The latter can be computed from

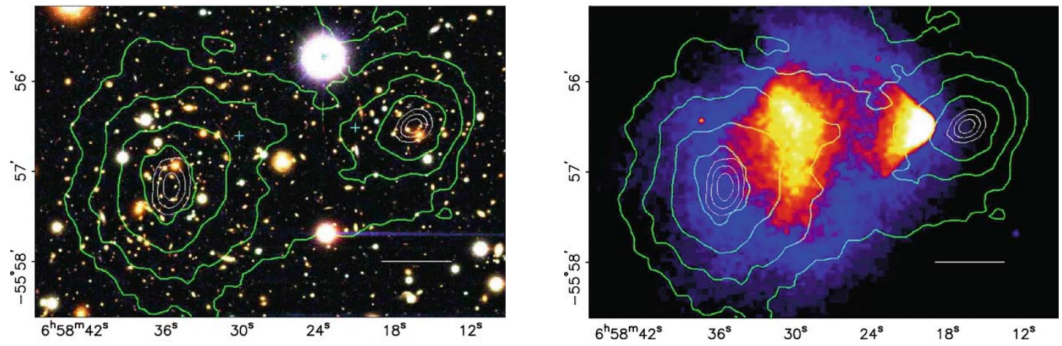

Figure 1.2 – Bullet cluster. Left: Optical map from the Magellan images for this cluster. Right: 500 *ks Chandra X-ray map. The green contours are the gravitational lensing mass distribution map. From [67].*

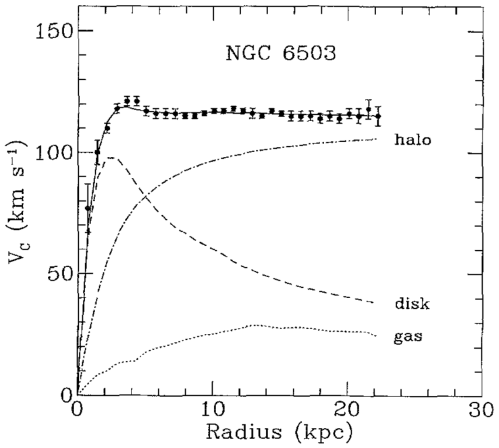

Figure 1.3 – Radial velocity distribution in function of r *for galaxy NGC 6503. Data indicate the presence of a dark halo extending to* $r \gg r_{\rm disk} \simeq 5$ *kpc. From [101].*

the rotation curve of spiral galaxies [101]. The circular velocity as a function of the distance r from the centre of the galaxy assumes a constant value out to much further extents than the radius of the stellar disk. Following Newton's law, the mass interior to r is $M(r) \propto r$, implying the existence of a much larger than the visible mass content, which can be described as a dark spherical halo surrounding the galaxy. The rotational velocity can be estimated by observing stars or gas clouds. The first measurement of this kind was a study by V. Rubin and W. K. Ford [130] of the rotational curve of the Andromeda Galaxy (M31) in 1970. Rubin's pioneering work over the seventies was the first evidence of a DM halo in galaxies and opened the ground for all the subsequent astronomical observations. A precise measurement of the rotational curves of the galaxies comes from the Doppler effect on the 21cm H-line [128]. Figure 1.3 shows how, for an only baryonic mass galaxy, the velocity would rapidly drop, not reflecting the observed behaviour.

The study of weak gravitational lensing is also a useful tool for measuring the total

mass of a galaxy. A foreground galaxy causes small distortions in the shape of background galaxies. Since the shape of a galaxy is a-priori unknown and the effect is as small as 1%, the lensing can be put in evidence by averaging over numerous background galaxies, searching for systematic distortions of their shapes towards the direction of the foreground galaxy centre. The effect must be studied on multiple foreground galaxies. The galaxy mass-to-light ratio estimated in this way is of the order of $M/L \sim 60$ [128].

1.2 The cosmological model

In this section, I will describe the salient points of the currently most accepted cosmological model: the Lambda Cold Dark Matter (Λ-CDM) model, with an emphasis on the dark matter role and on how the cosmological properties of dark matter have been experimentally probed by recent results of Planck [30]. In 1.2.1 we present the cosmological model. Results from Planck and the way they constrain the cosmological parameters will be discussed in 1.2.2. The role of dark matter as indicated by the Planck results will be explained in 1.2.3

1.2.1 The Λ-CDM model

As previously mentioned, the most supported theory to describe the evolution of the Universe is currently the Λ-CDM model [60]. By observing the CMB temperature anisotropies (more details will be given in 1.2.2), we can deduce that the space is the same for every direction we observe, namely, it is isotropic. The Copernican principle, stating that we are not at a special point in the Universe, suggests that the space should look the same from every point of observation, i.e. it is homogeneous. The Universe is, thus, a spherically symmetric space which evolves in time. This homogeneous, isotropic, and expanding Universe can be described by the Robertson-Walker metric, which can be expressed as [128]:

$$ds^2 = -dt^2 + a^2(t)\left[\frac{dr^2}{1-\kappa r^2} + r^2 d\Omega^2\right], \tag{1.5}$$

where t is the time coordinate, r is the radial coordinate and Ω is the solid angle coordinate. The term $a(t)$ is known as the scale factor and κ is the curvature parameter. The spatial part of the metric can be expressed in spherical coordinates for the properties explained above. It is worth mentioning the three possible scenarios given the value of κ:

- $\kappa < 0$: negative curvature, the Universe is *open*;
- $\kappa = 0$: no curvature, the Universe is flat;
- $\kappa > 0$: positive curvature, the Universe is *closed*;

The most recent results (see 1.2.2) point at a flat Universe with $\kappa \sim 0$.
Being ρ and p the density and pressure, respectively, the energy-momentum tensor of a uniform and isotropic Universe can be described as a perfect fluid:

$$T_{\mu\nu} = (\rho + p)(U_\mu U_\nu + p g_{\mu\nu}), \tag{1.6}$$

which, by raising an index, becomes:

$$T^\mu{}_\nu = diag(-\rho, p, p, p), \tag{1.7}$$

thus, the trace is:

$$T = -\rho + 3p. \tag{1.8}$$

The Einstein equation applied to these metric and tensor leads to the two so-called Friedmann equations which describe the evolution of the scale factor:

$$\left(\frac{\dot{a}}{a}\right)^2 = \frac{8\pi G}{3}\rho + \frac{\Lambda}{3} - \frac{\kappa}{a^2}, \tag{1.9}$$

$$\frac{\ddot{a}}{a} = -\frac{4\pi G}{3}(\rho + 3p) + \frac{\Lambda}{3}, \tag{1.10}$$

where Λ is the cosmological constant describing the vacuum energy component of the Universe and the Hubble rate H is defined as

$$H = \frac{\dot{a}}{a}, \tag{1.11}$$

and its current value is H_0, or Hubble constant, which is often expressed as $H_0 = 100h$ km/s/Mpc.
Friedmann equations can be rewritten by introducing the definition of a density parameter:

$$\Omega = \frac{\rho}{\rho_c} = \frac{8\pi G}{3H^2}\rho, \tag{1.12}$$

where $\rho_c = 3H^2/8\pi G$ is the so-called *critical density*. At present, the critical density assumes the value $\rho_c^0 = 3H_0^2/8\pi G$.
We can now re-formulate (1.9) as:

$$\Omega - 1 = \frac{\kappa}{H^2 a^2}. \tag{1.13}$$

When considering a flat Universe, the curvature parameter has a value $\kappa = 0$. Eq. (1.9) can then be simplified as:

$$1 = \sum_i \Omega_i, \tag{1.14}$$

where i are the different energy density parameters for the radiation (Ω_R), matter (Ω_M) and vacuum (Ω_Λ) content of the Universe, each of which will evolve differently with the Universe's expansion. The radiation density accounts for the density of the relativistic particles mostly accounted for by the CMB, while the matter density includes all matter that is non-relativistic including dark matter, Ω_χ.

1.2.2 The Cosmic Microwave Background

The Cosmic Microwave Background (CMB) is an isotropic signal in the microwave sky. It is the best measured black body spectrum [125] and is one of the furthest observables in the Universe It consists of light emitted at the epoch of recombination, i.e. when ions in the early Universe recombined to form atoms and photons traveled freely without interacting with matter, when the Universe was aged $t_{\rm CMB} \sim 380\ 000$ y. For an observer today, the CMB is seen as a distribution of temperatures with an average temperature that has been measured with extreme precision at $T_{\rm CMB} = 2.72548 \pm 0.00057$ K [82]. This temperature is remarkably isotropic all over the sky, however it has shown to have

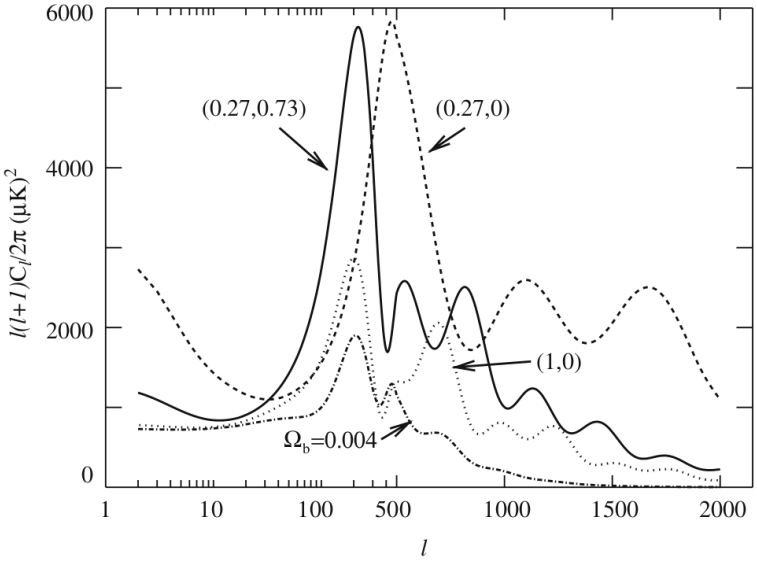

Figure 1.4 – CMB spectrum as a function of the angular scale ℓ. The solid line represents the model with $\Omega_M, \Omega_\Lambda = (0.27, 0.73)$. Other combinations represented are $(0.27, 0)$ (dashed line) and $(1, 0)$ (dotted line). The dash-dotted curve is given by the combination $\Omega_M, \Omega_\Lambda, \Omega_b = (1, 0, 0.004)$.

small anisotropies, of the order of $\Delta T_{\rm CMB} \sim 10^{-5}$ K, which are a powerful tool to probe the cosmological model.
Temperature anisotropies can be decomposed over the bases of spherical harmonics, so that:

$$\frac{\delta T}{T}(\theta, \phi) = \sum_{\ell=2}^{\inf} \sum_{m=-\ell}^{+\ell} a_{\ell m} Y_{\ell m}(\theta, \phi), \tag{1.15}$$

where $Y_{\ell m}(\theta, \phi)$ are the spherical harmonics. The variance C_ℓ of $a_{\ell m}$ is defined [54] as:

$$C_\ell \equiv \langle |a_{\ell m}|^2 \rangle \equiv \frac{1}{2\ell + 1} \sum_{m=-\ell}^{+\ell} |a_{\ell m}|^2, \tag{1.16}$$

which, in plots, is generally shown as $\ell(\ell + 1)C_\ell/2\pi$.
The shape and features of the CMB anisotropies spectrum are strong indicators of the different cosmological parameters [128]:

- $\kappa \neq 0$ makes the low ℓ region less flat while $\Omega_\Lambda \neq 0$ mildly affects the same region in the same way;
- $\Omega_M h^2$ affects the position of the first peak and the amplitude of the peaks;
- the density of dark matter, $\Omega_\chi h^2$, affects the ratio between the heights of the second and third peaks. Therefore a relatively high third peak is an indication of the presence of DM;

- $\Omega_b h^2$ affects the overall height of the peaks.

Fig. 1.4 shows the CMB spectrum for different combinations of the parameters.

The CMB was first discovered [122] in 1964 by the radio astronomers Arno Penzias and Robert Wilson as an excess in the radio signal noise of their antenna. In the following years, many (including balloon and space satellite) experiments observed and measured the CMB. Data from the Planck satellite mission provided an extremely precise measurement of the CMB temperature anisotropies, which allowed for an accurate estimation of the parameters of the Λ-CDM cosmological model (see 1.2.1). A map of the CMB anisotropies measured by Planck can be seen in fig.1.5. The Planck temperature power spectrum as a function of the angular scale ℓ is shown in fig.1.6.

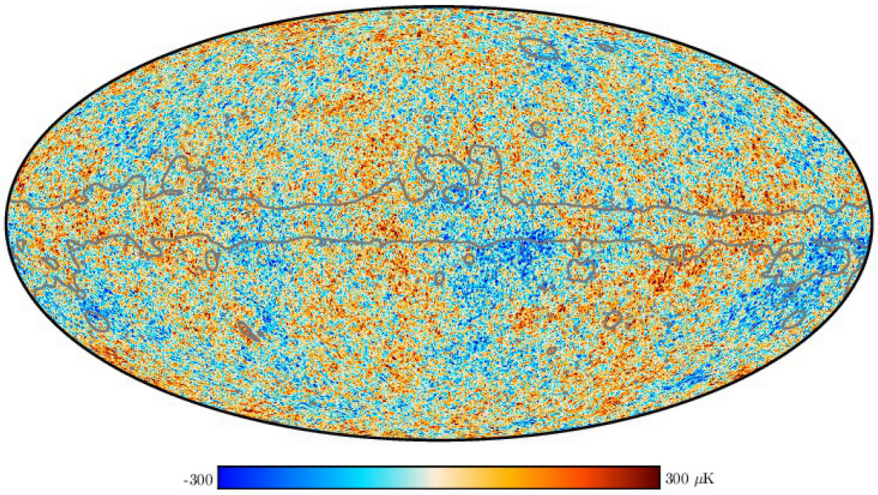

Figure 1.5 – Full sky map of the CMB temperature anisotropies by Planck [125].

Results from Planck [30] are consistent with a flat universe with a low radiation contirbution $\Omega_R \ll \Omega_M$, and $\Omega_M \simeq 0.31$, $\Omega_\Lambda \simeq 0.69$. This means we are in a vacuum dominated epoch where, nonetheless, matter still has a relevant role. Furthermore, if Ω_Λ is constant in time, we are in a Universe that will continue expanding. The current value of the Hubble parameter is $H_0 \simeq 67.66$ km/s/Mpc.
We can consider Ω_M to be the sum of a baryonic (Ω_b) and a non-baryonic (Ω_χ) component of the matter. Planck results [30] give $\Omega_b/\Omega_\chi \simeq 0.18$, meaning that there is a matter component, beyond the baryonic one, which constitutes the majority of the matter content in the Universe. This is possibly the most compelling evidence for the existence of dark matter.

1.2.3 Thermal dark matter

Let us consider a model that assumes there was an equilibrium between the creation and annihilation of dark matter when the Universe was dense enough. As the Universe expands, the rate of DM annihilation decreases (dark matter particles are separated from each other and they cannot self-annihilate) and this equilibrium is lost leaving behind a frozen density of DM that still exists today. This time is called the *freeze-out*

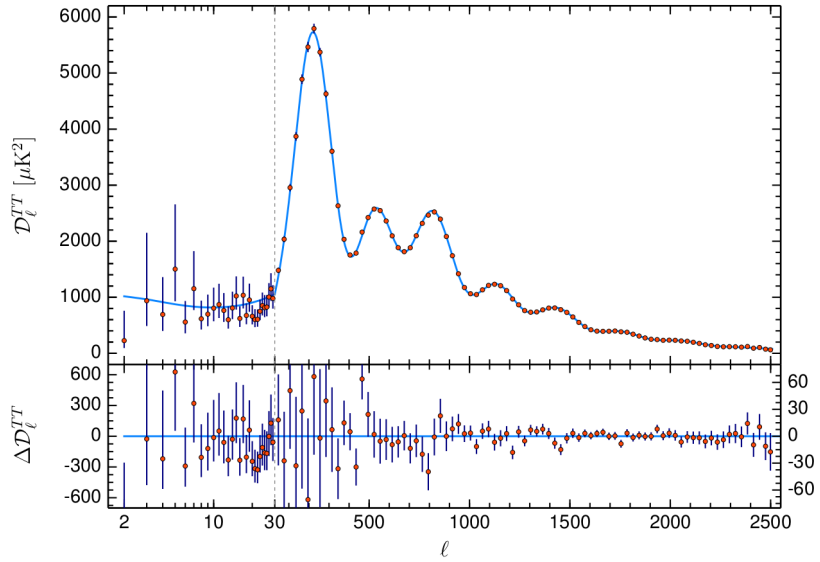

Figure 1.6 – Planck temperature power spectrum. The blue line is the best fit cosmological model. The horizontal scale changes from logarithmic to linear after $\ell > 30$. From [30].

of dark matter. The time of freeze-out is defined as the time when the annihilation rate becomes of the order of the Hubble rate [106]:

$$\Gamma_{\rm A} = n_\chi \langle \sigma_{\rm A} v \rangle \sim H, \tag{1.17}$$

where n_χ is the DM number density which, for cold (non-relativistic) dark matter depends on the temperature T (or Universe expansion) as a Maxwell-Boltzmann distribution:

$$n_\chi \sim T^{3/2} e^{-m_\chi/T}, \tag{1.18}$$

where m_χ is the DM particle mass. Hot dark matter will have a different dependence with the temperature.
Assuming there is *kinetic equilibrium*, given by interactions of the type $\chi SM \rightarrow \chi SM$, and according to the Boltzmann equation, in an expanding Universe the moment of the freeze-out (at the temperature T_{fo}) is given by the condition:

$$n_\chi(T_{fo}) \langle \sigma_{\rm A} v \rangle = 3H(T_{fo}), \tag{1.19}$$

and a relation between the DM density Ω_χ and the annihilation cross-section $\langle \sigma_{\rm A} v \rangle$ can be estimated [101]:

$$\Omega_\chi h^2 \simeq \frac{3 \times 10^{-27}\ {\rm cm\ s^{-1}}}{\langle \sigma_{\rm A} v \rangle}. \tag{1.20}$$

The constrain on Ω_χ presented in 1.2.2 can be applied to (1.20), to obtain an estimate on the annihilation cross-section for thermal dark matter of the order of $\langle \sigma_{\rm A} v \rangle \simeq 3 \times 10^{-26}$ cm^3 s $^{-1}$. Coincidentally, the value of $\langle \sigma_{\rm A} v \rangle$ that explains the observed DM relic density that we observe, is in the range of the weak-force interactions, a coincidence that is commonly known in the literature as the "WIMP miracle".

1.3 Dark Matter candidates

As we have seen, astronomical and cosmological observations support the idea that the matter deficit is indeed caused by unseen matter. One of the most supported theories to explain DM is that it is made of particles. As stated in 1.2, a cold DM model implies that these particles were non-relativistic at the time when galaxy formation started. Many candidates have been proposed to explain DM [54]. Results from Planck (see 1.2) indicate that the majority of the matter in the Universe must be non-baryonic. Non-baryonic particle candidates are, thus, among the most interesting DM theories. The most popular non-baryonic candidates are Weakly Interacting Massive Particles (WIMPs) and axions. WIMPs arise from extensions of the Standard Model. The most popular WIMP candidate is the neutralino which arises from supersymmetric extensions of the SM. The neutralino mass ranges from a few GeV to a few TeV. Axions were postulated to explain the strong CP problem and have mass $m_a \ll$ eV. Alternative DM theories have also been proven valuable, including the Kaluza-Klein WIMP model and dark objects like primordial black holes (PBHs). In the following paragraphs, I will present the most relevant dark matter candidates.

1.3.1 WIMPS

Supersymmetry

In the Standard Model (SM) of particles, bosons are the mediators of interactions and carry integer spin, while fermions are the constituents of matter and have half values of spin. Supersymmetry (SUSY) [101] is a theory which aims at a unified representation of bosons and fermions, introducing a new symmetry which links them. The lightest of these supersymmetric particles constitute a good DM candidate. SUSY provides a technically natural extension of the SM.

The minimal supersymmetric standard model (MSSM) is the simplest possible supersymmetric theory as it only requires an extra Higgs doublet and the supersymmetric partners of the known particles, which differ from their standard partners by one-half spin. Interaction are the ones permitted by the SM gauge symmetry $\mathrm{SU}(3)\times\mathrm{SU}(2)\times\mathrm{U}(1)$. The most interesting characteristic of this theory is the conservation of R-parity, defined as [101]:

$$R = (-1)^{3(B-L)+2S}, \tag{1.21}$$

where B and L are the baryonic and leptonic number operators, respectively, and S is the spin. $R = +1$ for SM particles and $R = -1$ for their supersymmetric partners. SUSY particles cannot thus decay into SM particles, meaning that the lightest SUSY particle is stable. The lightest supersymmetric particle (LSP) is a well-motivated candidate for cold dark matter. In this model, Z^0 and the neutral Higgs boson carry the same quantum numbers so that at the breaking of the electroweak symmetry they form four mass eigenstates called *neutralinos*. The lightest neutralino is the best candidate to be the LSP and can thus be written as a linear combination [101]:

$$\chi = N_{10}^{*}\tilde{B} + N_{20}^{*}\tilde{W}^3 + N_{30}^{*}\tilde{H}_1^0 + N_{40}^{*}\tilde{H}_2^0, \tag{1.22}$$

where $\tilde{B}$ and $\tilde{W}^3$ are the SUSY partners of the gauge fields B and W^3 which form the photon and Z_0 and $\tilde{H}_1^0$ and $\tilde{H}_2^0$ are the two neutral higgsinos. The neutralino can only

interact weakly with SM particles and would be highly non-relativistic at the current epoch. It can be referred to as a weakly interacting massive particle (WIMP) and is a good DM particle candidate.

Kaluza-Klein dark matter

Another interesting WIMP dark matter candidate arises from models with universal extra dimensions [62]. In such models, all the SM particles propagate into compact extra-dimensions. The momentum conservation is described by the conservation of the Kaluza-Klein (KK) number. KK-parity implies the existence of a lightest Kaluza-Klein particle (LKP) [132], which is stable and interacts with the SM particles. Many hypotheses have been proposed on the nature of the LKP. The simplest extensions, including one extra-dimension, can give rise to LKP candidates such as the KK-photon and KK-neutrino. One of the advantages of the KK theory is that it generally needs a low number of assumptions, including essentially one free parameter, which is the mass of the LKP. For the latter being in the hundreds of GeV range, KK dark matter fulfills the dark matter relic density measured in cosmological observations [132].

1.3.2 Axions

The mathematical formulations of the quantum-chromo-dynamics (QCD) include the possibility of breaking the CP-symmetry [147], but no experimental evidence for this violation has been found so far. This puzzle is referred to as the *strong CP problem*. Axions were introduced by Peccei and Quinn (PQ) [120] to resolve the strong CP problem. The PQ scheme is, in fact, an appealing way of preserving the CP-symmetry in QCD.

Axions [150] are pseudo-scalars which acquire a mass via a small explicit symmetry breaking. The scale of their interaction must be much bigger than the electroweak symmetry-breaking scale: $f_a \gg v_{EW}$. The relation between the mass of the axion and its interaction strength is fixed by the mixing with π_0. A more general variety of axion-like particles (ALPs) arises when considering the mass and coupling as independent parameters.

Axions are very weakly coupled light particles. Their characteristics make them a good DM candidate and the chances of discovering them are considered realistic. Searches for axions/ALPs include observation of axion dark matter and solar axions. Typical laboratory experiments attempt at the detection of light shining through a wall.

1.3.3 Neutrinos

As neutrinos are only weakly interacting particles, they have been considered possible dark matter candidates. We can estimate their contribution to the total content of the Universe with [150]:

$$\Omega_\nu \simeq \frac{\sum_i m_i}{93h^2 \text{ eV}}, \tag{1.23}$$

which, assuming the Planck results [125], gives a limit of:

$$\Omega_\nu \lesssim 0.002. \tag{1.24}$$

The result in (1.24) indicates that neutrinos cannot account for the entirety of dark matter.

The existence of the so-called *sterile* neutrino [141] have been proposed to explain some characteristics of *active* neutrinos. It is known that neutrinos have left-handed chirality and have mass. Hence, a motivation for sterile neutrinos comes simply from the observation that every other left-handed lepton has a right-handed companion. Also, the presence of sterile neutrinos brings a natural explanation to the neutrino mass. Sterile neutrinos could also explain some anomalies observed in neutrino oscillation patterns in various experiments. Sterile neutrinos only interact with SM particles gravitationally and via mixing with the other neutrino flavours. Light mass candidates have been excluded for the same reasons as SM neutrinos, but heavy sterile neutrinos are still viable dark matter candidates.

1.3.4 Macroscopic dark matter candidates

Although strong constraints were put on the mass of a baryonic dark matter hypothesis, a space for a class of macroscopic objects which, possibly made of baryonic matter, could be a part of the invisible content of the Universe still remains open. Massive compact halo objects (MACHOs) such as brown dwarfs and planets were constrained by microlensing observations in the Magellanic clouds [138]. Cosmological observations related to the Big-Bang Nucleosynthesis (BBN) strongly constrained the baryonic content of the Universe. The last interesting macroscopic dark matter candidate currently under investigation is primordial black holes (PBH). PBHs would have formed in the early Universe. An example of formation is that interaction of fragments of a scalar condensate called Q-balls [70] leads to the formation of PBHs. This phenomenon is predicted in many SUSY models [90]. The mass of these black holes could account for a part of DM. PBHs could also explain some of the events detected with the LIGO experiment. Future gravitational waves detectors will be sensitive to gravitational wave events originated from PBHs up to $M_{\rm PBH} \simeq 10^{-12} M_{\odot}$ [50].

1.4 Dark matter distribution

As written in 1.1, dark matter effects are visible from the largest to the local scales. In this section I will expose how DM is distributed, starting from the overall distribution in the Universe (1.4.1), then zooming in to the distribution in the Galaxy (1.4.2).

1.4.1 The Universe

The dark matter distribution in the Universe can be estimated via complex numerical simulations [133]. The structure of DM appears non-homogeneous at small scales. In fact, following the initial fluctuations observed in the CMB [38], it would form a sort of web, with filaments and sheets. In the Λ-CDM model, matter collapses into bigger and bigger clusters to form halos. Galaxies would form at the gravitational centre of those halos and clusters of galaxies would form subsequently to even further aggregation. Simulations are in agreement with the large-scale structure of the observable Universe. The map [89] in figure 1.7 shows the structure of the Universe around the Earth up to a

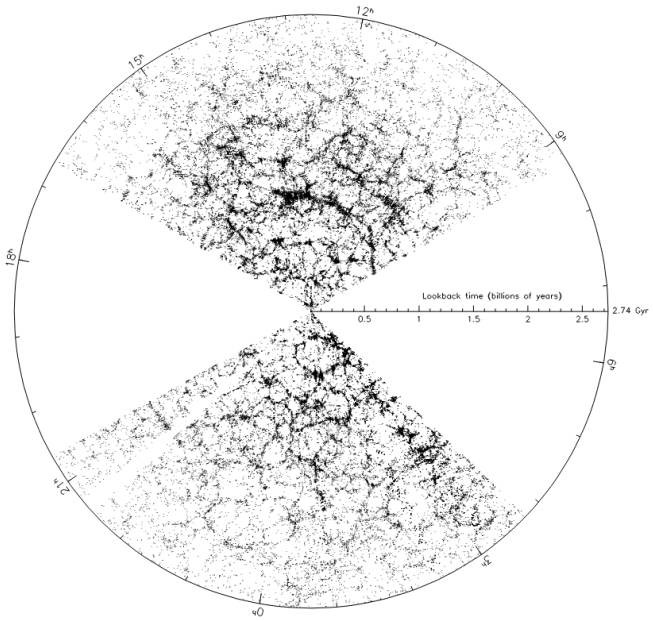

Figure 1.7 – Projected map of the sky, showing SDSS galaxies up to a distance of 2.74 Gly. From [89].

distance of 2.74 billion light-years. The map gives a glance at the aggregation processes of the Universe: the further we look, the younger is the Universe and the less structure is visible.

1.4.2 The Milky Way

The distribution of DM in galaxies can be modelled from the observation of the rotation speed and simulations. A spherical halo formed as explained in 1.4.1, and its density increases towards the centre. The Milky Way is a typical spiral galaxy so that, with measures of the rotation speed, for example, of the satellite galaxies, we can infer the parameters better describing its DM distribution. The Standard Halo Model (SMH) is the most accepted model, and it assumes a Maxwellian velocity distribution. The velocity parameters assumed in this work are the average velocity $v = 220$ km s^{-1} and the velocity dispersion $v_{\rm RMS} = 270$ km s^{-1}. It must be noted that the recent GAIA results indicate the presence [115], at least locally, of non-trivial substructures in the velocity distribution due to particles that are not in equilibrium. The local halo DM density cannot be stated with certainty and is expected to be in the range $0.1 < \rho_{\rm DM}/{\rm GeV\ cm^{-3}} < 0.5$ [115]. The value assumed conventionally and used for the analysis presented in this work is $\rho_{\rm DM} = 0.3$ GeV cm^{-3}. Many uncertainties are still unresolved, especially in the description of the inner distribution of the halo. Some profiles, like the Navarro-Frank-White (NFW) [114], predict a more peaked distribution in the centre of the Galaxy than others, like the Burkert [59] one. The solar system, located at $r_\odot \simeq 8.5$ kpc, is well inside the DM halo. Models are in good agreement outside the solar circle, as shown in fig. 1.8. The following section will focus on the mechanisms that could enhance the

concentration of DM in peculiar sites such as the centre of massive bodies.

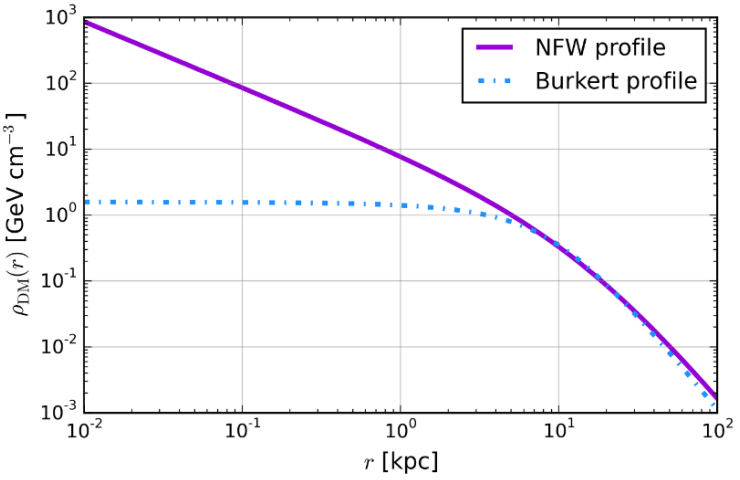

Figure 1.8 – Dark matter galactic distribution for the NFW and Burkert profiles. From [41]

1.5 Dark matter interactions

The aim of this section is to describe the possible types of interactions that link dark matter with the Standard Model. Firstly, dark matter particles can scatter off SM nuclei, producing a nuclear recoil. A wider ensemble of interactions is possible in general depending on the DM model. The effective field theory of dark matter allows for constraining the interaction couplings independently of the model. Dark matter particles also can, if they are Maiorana particles, self-annihilate. A possibility is, as well, left open for DM particles to decay into SM particles. Scattering and annihilation are the basic ingredients in the process of capture and annihilation in the centre of celestial objects such as the Sun and the Earth. This section is, thus, key to the understanding of the work developed for this thesis, which will be described in chapters 4 and 5.

1.5.1 Scattering off Standard Model particles

Dark matter particles can scatter off Standard Model particles although the coupling is expected to be weak, so the cross-section for this process is small. The cross-section for dark matter scattering off Standard Model nuclei can be generally described [56] with:

$$\frac{d\sigma(E_r)}{dE_r} = \frac{m_N}{2v^2\mu^2}\left[\sigma^{\mathrm{SI}}F^2_{\mathrm{SI}}(E_r) + \sigma^{\mathrm{SD}}F^2_{\mathrm{SD}}(E_r)\right], \tag{1.25}$$

where E_r is the nuclear recoil energy and μ is the reduced mass of the DM-nucleus system. The former term in brackets represents the spin-independent (SI) component, which is a scalar interaction. The latter is the spin-dependent (SD) component, which is

an axial-vector interaction. $F_{\rm SI}$ and $F_{\rm SD}$ are the form factors for spin-independent and spin-dependent scattering, respectively.

The spin-independent WIMP-nucleus cross section, relative to a nucleon n of the considered nucleus, can be reduced [56] to:

$$\sigma^{\rm SI} = \frac{\mu}{\mu_n}\sigma_{\chi n}A^2, \tag{1.26}$$

where μ_n is the reduced mass of the DM-nucleon system and $\sigma_{\chi n}$ is the WIMP-nucleon cross-section. The proportionality to the square of the atomic number A^2 indicates that spin-independent scattering is favoured for heavier compositions.

The spin-dependent WIMP-nucleus cross-section can be expressed [56] as:

$$\frac{d\sigma^{\rm SD}}{d|\overrightarrow{q}|^2} = \frac{8G_F}{\pi v^2}\left[a_p\langle S_p\rangle + a_n\langle S_n\rangle\right]^2 \frac{J+1}{J}\frac{S(|\overrightarrow{q}|)}{S(0)}, \tag{1.27}$$

where $|\overrightarrow{q}|$ is the total momentum transfer, and $\langle S_p\rangle$ and $\langle S_n\rangle$ are the expectation values of the spin operators for protons and neutrons, respectively. $S(|\overrightarrow{q}|)$ is the spin-structure function and J is the nuclear spin of the target.

1.5.2 Effective field theory

An effective field theory (EFT) for dark matter arose in an attempt to loosen the tension between results in dark matter direct detection experiments [81] (see 1.6.2). Nonetheless, an EFT for dark matter is appealing because it considers a wide range of possible interactions, including momentum-dependent ones. The different approach consists in not probing a particular model. Instead, the aim is to explore the leading non-relativistic coupling operators between DM and SM nuclei. The operators arising in the construction of this EFT include spin-independent (SI), spin-dependent (SD), angular momentum-dependent (LD) and spin and angular momentum-dependent (LSD) interactions.

The form of the interactions is constrained by multiple symmetries[81]. The Galilean invariance, in particular, can be described by two invariants: the momentum transfer $\overrightarrow{q} = p' - p$ and the relative incoming velocity between the DM particle and the SM nucleus $\overrightarrow{v} = \overrightarrow{v}_{\chi,in} - \overrightarrow{v}_{N,in}$. If we consider that the interactions must be Hermitian, the complete set of variables with which the interaction operators can be described is $i\overrightarrow{q}$, $\overrightarrow{v}^{\perp} = \overrightarrow{v} + \overrightarrow{q}/2\mu_N$ and the two spin operators S_χ and S_N for the DM particle and the SM nucleus, respectively. μ_N is the reduced mass of the nucleus-DM system.
The general Lagrangian for non-relativistic elastic scattering interactions is composed of four-field operators in the form:

$$\mathcal{L}_{int} = \sum_{N=n,p}\sum_i c_i^N \mathcal{O}_i \chi^+\chi^- N^+ N^-, \tag{1.28}$$

where $\chi^\pm$ and $N^\pm$ are the four fields, two for DM and two for SM, respectively. c_i^N are the coupling constants, for neutrons n and protons p. Usually results are presented in the form of iso-scalar $c_i^0 = c_i^p + c_i^n$ and iso-vector $c_i^1 = c_i^p - c_i^n$ coupling constants [124]. Table 1.1 resumes the set of operators $\mathcal{O}_i$ from [61]. The first 12 operators are the basic set. Further operators can be obtained as products of the type $\mathcal{O}_i\mathcal{O}_j$ of the first 12 [81]. Usually, each operator is probed singularly by setting all the other coupling constants to 0.

$\mathcal{O}_1 = \mathbb{1}_{\chi N}$	$\mathcal{O}_9 = i\,\overrightarrow{S}_\chi \cdot \left(\overrightarrow{S}_N \times \frac{\vec{q}}{m_N}\right)$
$\mathcal{O}_3 = i\,\overrightarrow{S}_N \cdot \left(\frac{\vec{q}}{m_N} \times \overrightarrow{v}^\perp\right)$	$\mathcal{O}_{10} = i\,\overrightarrow{S}_N \times \frac{\vec{q}}{m_N}$
$\mathcal{O}_4 = \overrightarrow{S}_\chi \cdot \overrightarrow{S}_N \cdot$	$\mathcal{O}_{11} = i\,\overrightarrow{S}_\chi \times \frac{\vec{q}}{m_N}$
$\mathcal{O}_5 = i\,\overrightarrow{S}_\chi \cdot \left(\frac{\vec{q}}{m_N} \times \overrightarrow{v}^\perp\right)$	$\mathcal{O}_{12} = i\,\overrightarrow{S}_\chi \cdot \left(\overrightarrow{S}_N \times \overrightarrow{v}^\perp\right)$
$\mathcal{O}_6 = \left(\overrightarrow{S}_\chi \cdot \frac{\vec{q}}{m_N}\right)\left(\overrightarrow{S}_N \cdot \frac{\vec{q}}{m_N}\right)$	$\mathcal{O}_{13} = i\left(\overrightarrow{S}_\chi \cdot \overrightarrow{v}^\perp\right)\left(\overrightarrow{S}_N \cdot \frac{\vec{q}}{m_N}\right)$
$\mathcal{O}_7 = \overrightarrow{S}_N \cdot \overrightarrow{v}^\perp$	$\mathcal{O}_{14} = i\left(\overrightarrow{S}_\chi \cdot \frac{\vec{q}}{m_N}\right)\left(\overrightarrow{S}_N \cdot \overrightarrow{v}^\perp\right)$
$\mathcal{O}_8 = \overrightarrow{S}_\chi \cdot \overrightarrow{v}^\perp$	$\mathcal{O}_{15} = -\left(\overrightarrow{S}_\chi \cdot \frac{\vec{q}}{m_N}\right)\left[\left(\overrightarrow{S}_N \times \overrightarrow{v}^\perp\right) \cdot \frac{\vec{q}}{m_N}\right]$

Table 1.1 – Set of effective field theory operators appearing in (1.28) *for a single nucleon N of mass m_N. From [61]. The standard SI and SD operators are [124] $\mathcal{O}_1$ and $\mathcal{O}_4$, respectively.*

1.5.3 Self-annihilation and decay

Dark matter particles can produce SM particles mainly in two ways: by self-annihilation and by decay. The flux of neutrinos from self-annihilation of dark matter from a source is:

$$\frac{d\Phi}{dE} = \frac{1}{4\pi}\left(\frac{\rho_{\rm DM}}{m_{\rm DM}}\right)^2 \frac{\langle\sigma_{\rm A} v\rangle}{2} \sum_F B_F \left(\frac{dN_\nu}{dE_\nu}\right)_F , \tag{1.29}$$

while for decay we can write:

$$\frac{d\Phi}{dE} = \frac{1}{4\pi}\frac{\rho_{\rm DM}}{m_{\rm DM}}\Gamma_{\rm D} \sum_F B_F \left(\frac{dN_\nu}{dE_\nu}\right)_F . \tag{1.30}$$

For both equations (1.29) and 1.30 $\rho_{\rm DM}$ is the dark matter density at the source and B_F denotes the F branching fraction into a specific annihilation/decay channel. $\langle\sigma_{\rm A} v\rangle$ is the velocity-averaged annihilation cross-section, while $\Gamma_{\rm D}$ is the inverse lifetime of the dark matter particle.

In a more general fashion, the dark matter density $\rho_{\rm DM}$ in equations (1.29) and (1.30) can be substituted with the so-called J-factor, which is an integral of $\rho_{\rm DM}$ ($\rho^2_{\rm DM}$ for the annihilation case) over the angular extension of the source and the line of sight. This factor accounts for the fact that the Galactic Halo, which surrounds the Solar System, is itself a source, and some sources cannot be considered point-like.

1.5.4 Capture in celestial bodies

The work described in this thesis follows the theorised process of accumulation of dark matter in the centre of celestial bodies, which will be described in detail in this section. Dark matter particles can scatter off nuclei in the vicinity of a massive celestial body, lose velocity and become gravitationally trapped in the centre of the object. The process could be led by either the spin-independent or spin-dependent scattering interactions, depending on the elements on which there is a higher chance of scattering off. An accumulation of dark matter in the region of the centre of the body can trigger dark matter self-annihilation into SM particles. If N_χ is the DM density in the centre of a celestial body, the evolution is described by the following equation [92]:

$$\dot{N}_\chi = C_\mathrm{C} - C_\mathrm{A} N_\chi^2 - C_\mathrm{E} N_\chi, \tag{1.31}$$

where C_C is the capture rate, which is proportional to $\sigma_{\chi n}$, $C_\mathrm{A} N^2 = \Gamma_\mathrm{A}/2$ is the annihilation term, where Γ_A is the annihilation rate, and $C_\mathrm{E} N$ is the evaporation term. Evaporation describes the case where a DM particle gains energy by scattering and escapes the gravitational field to which it is subject.

Capture

The capture rate C_C depends on whether the axial-vector (spin-dependent) or scalar (spin-independent) interaction is considered. For the axial-vector case we can write [101]:

$$C_\mathrm{C}^{ax} \propto \frac{\rho_\chi \sigma_{spin}^{\chi p}}{m_\chi \bar{v}}, \tag{1.32}$$

where ρ_χ is the local halo dark matter density, m_χ is the dark matter mass and $\sigma_{\chi p}$ is the DM-proton cross-section. For the scalar case we can write [101]:

$$C_\mathrm{C}^{sc} = c \frac{\rho_\chi}{m_\chi \bar{v}} \sum_i F_i(m_\chi) \sigma_{scalar}^{\chi p} f_i \phi_i \frac{S(m_\chi / m_{N_i})}{m_{N_i}}, \tag{1.33}$$

where i denotes an element and the sum over i is the sum over all the relevant elements for capture. The terms $\sigma_{scalar}^{\chi p}$, f_i, and ϕ_i are the DM-nucleus cross-section, the abundance fraction and distribution, respectively, of the i-th element. $F_i(m_\chi)$ are the branching fractions of the various annihilation channels. The term $S(m_\chi/m_{N_i})$ is the kinematic suppression factor for a dark matter particle of mass m_χ scattering off a nucleus i of mass m_{N_i}. The term tends to 1 when the DM mass m_χ is close to m_{N_i}. Please note that all the masses in equations (1.32) and (1.33) are in a unitless form of the type $m/(1\ \mathrm{GeV})$.

Capture in EFT In the EFT frame, the interaction cross-section depends on the coupling constants defined in 1.5.2. Following [61], the differential cross-section for a nuc-

leus T is defined:

$$\frac{d\sigma_{\chi T}(q^2,w^2)}{dq^2} = \frac{1}{(2J+1)w^2}\sum_{\tau\tau'}\left[\sum_{k=M,\Sigma',\Sigma''} R_k^{\tau\tau'}\left(v_T^{\perp\,2},\frac{q^2}{m_N^2}\right)W_k^{\tau\tau'}(q^2) + \frac{q^2}{m_N^2}\sum_{k=\Phi'',\Phi'',M,\tilde{Phi}',\Delta,\Delta\Sigma'} R_k^{\tau\tau'}\left(v_T^{\perp\,2},\frac{q^2}{m_N^2}\right)W_k^{\tau\tau'}(q^2)\right], \quad (1.34)$$

where $R_k^{\tau\tau'}$ depend on the coupling constants c_j^τ. $W_k^{\tau\tau'}$, namely Φ'', M, $\tilde{\Phi}'$, Δ, Σ' and Σ'', are the nuclear response operators [81]. w is the relative velocity between the DM particle and the nucleus. J is the target nucleus spin. The other parameters were defined in 1.5.2.
A more general expression for the capture rate is given by [61]:

$$C_{\rm C} = \sum_T n_T \int_0^R dr 4\pi r^2 \int_0^\infty du \frac{f(u)}{u} w^2 \Theta\left(\frac{\mu_T}{\mu_{+,T}^2} - \frac{u^2}{w^2}\right)\int_{E_{min}}^{E_{max}} dE_r \frac{d\sigma_{\chi T}(E_r,w^2)}{dE_R}, \quad (1.35)$$

where the sum is over all the T elements contributing to the capture process, r is the distance from the centre of gravity. The value of R is the radius of the capturing object, i.e. $R_\oplus$ and $R_\odot$ for the Earth and the Sun, respectively. u is the velocity of the DM particle at infinity, and w is defined as $w = \sqrt{u^2 + v_{esc}(r)^2}$, with $v_{esc}(r)$ being the escape velocity at a distance r. $\mu_T \equiv \mu_\chi/\mu_T$ and $\mu_{\pm,T} \equiv (\mu_T \pm 1)/2$ are dimensionless parameters. $d\sigma_{\chi T}/dE_r$ can be obtained from (1.34) knowing that $q^2 = 2m_T E_r$. The energy integration is computed over all the allowed nuclear recoil energies E_r, for which it is $[E_{min}, E_{max}] = [Eu^2/w^2, E\mu_T/\mu_{+,T}^2]$.

Annihilation

The annihilation term $C_{\rm A}$ depends [101] on the velocity averaged annihilation cross-section $\langle\sigma_{\rm A} v\rangle$:

$$C_{\rm A} = \langle\sigma_{\rm A} v\rangle\left(\frac{m_\chi \rho}{3m_{\rm P}^2 T}\right)^{\frac{3}{2}}, \quad (1.36)$$

where $m_{\rm P}$ is the Planck mass, T and ρ are, respectively, the temperature and the core density of the object. m_χ is the DM particle mass. For the mass values considered in this work, in the equation (1.31) describing the evolution of the dark matter concentration in the centre of a celestial body we can neglect the evaporation term [85], which is only relevant for masses $m_\chi \lesssim 4$ GeV. Solving the resulting equation for N we find:

$$\Gamma_{\rm A}(t) = \frac{1}{2} C_{\rm C} \tanh^2\left(\frac{t}{\tau}\right), \quad (1.37)$$

where $\tau = (C_{\rm C} C_{\rm A})^{-1/2}$ is the time scale for the capture and annihilation processes to reach equilibrium. The equilibrium condition is described by $t \gg \tau$, so that (1.37) becomes $C_{\rm C} = \frac{1}{2}\Gamma_{\rm A}$ and the subsequent annihilation rate is at its maximum.

Self-annihilation of dark matter particles generates SM particles. Neutrinos can be directly produced by the annihilation mechanism or be among the secondary products of these interactions. The neutrino flux arising from this process can be detected by a neutrino detector. The flux of neutrinos can be described [101] by:

$$\Phi_\nu = \frac{\Gamma_{\rm A}}{4\pi R^2} \sum_F B_F \left(\frac{dN_\nu}{dE_\nu}\right)_F , \tag{1.38}$$

with R being the source-target distance, B_F the branching fraction for the channel F and $(dN_\nu/dE_\nu)_F$ the neutrino spectrum for the channel F. A channel F is the SM channel to which dark matter self-annihilate (e.g. $\chi\chi \to \tau^+\tau^-$ or $\chi\chi \to b\bar{b}$). Usually, each channel is analysed separately assuming 100% branching fraction.

The relevant cases of capture and annihilation in the Earth, which is the topic of this work, and the Sun will be subsequently analysed more in detail.

Earth

The Earth's composition is heavier than the Sun's and the most abundant elements on Earth do not carry spin. Searches for self-annihilation in the Earth are, hence, more sensitive to spin-independent scattering processes.
Dark matter accumulation in the Earth is well described by (1.31). As from the definition in (1.33), the capture rate for the Earth depends on the mass of the DM particle: resonance scattering happens in correspondence to the most abundant elements in the Earth, enhancing the probability of scattering. Table 1.2 resumes [109] the Earth composition in the core and mantle of the planet. Fig. 1.9 shows the relation between the capture rate and the DM mass, where peaks are visible corresponding to the masses of the elements O, Mg, Si and Fe. It is worth reminding that the evaporation process can be neglected, in the case of the Earth, for masses larger than a few GeV [85]. For the term $C_{\rm A}$ we can write $C_{\rm A} \propto \rho_\chi^2$. For the case of the Earth, $C_{\rm A}$ can be derived from equation (1.36) and can be expressed in the form:

$$C_{\rm A} = \frac{\langle \sigma_{\rm A} v \rangle}{4\sqrt{2} \times 10^{25}\ \text{cm}^3} \left(\frac{m_\chi}{10\ \text{GeV}}\right)^{3/2} . \tag{1.39}$$

Element	Atomic number	Core fraction	Mantle fraction
O	16	0	0.440
Si	28	0.06	0.210
Mg	24	0	0.228
Fe	56	0.855	0.063
Ca	40	0	0.025
P	30	0.002	9×10^{-5}
Na	23	0	0.003
S	32	0.019	2.5×10^{-4}
Ni	59	0.052	0.002
Al	27	0	0.024
Kr	52	0.019	0.003

Table 1.2 – Distribution of elements on Earth [109].

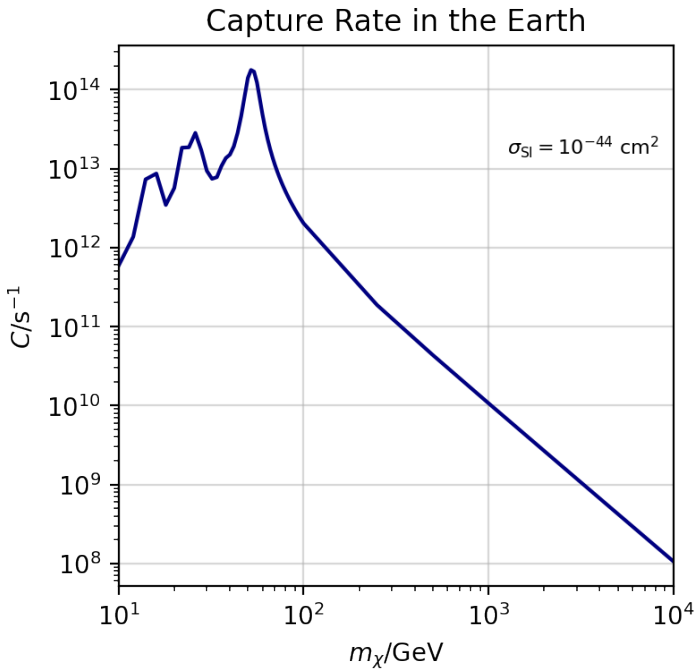

Figure 1.9 – Capture rate for the Earth in function of the WIMP mass, assuming $\sigma_{\mathrm{SI}} = 10^{-44}$ cm^2. The peaks indicate resonance capture with the Earth most abundant elements (O, Mg, Si, Fe). Computed using DarkSusy [58] [88] [75].

In the EFT, the capture rate depends strongly on which operator is chosen for analysis. All the other operators are set to zero. Capture rates can be computed using (1.35). The values used in this work are taken from tabulated versions of the computed rates in [61]. Fig. 1.10 shows some examples for selected operators.
Considering the age of the solar system $t_\oplus \simeq 4.9 \times 10^9$ y, for the Earth we can write [101]

$$\frac{t_\oplus}{\tau} = t_\oplus C_\mathrm{C} C_\mathrm{A} = 1.9 \times 10^{-4} \left(\frac{C_\mathrm{C}}{\mathrm{s}^{-1}}\right)^{-1/2} \left(\frac{\langle \sigma_\mathrm{A} v \rangle}{\mathrm{cm}^3 \mathrm{s}^{-1}}\right)^{-1/2} \left(\frac{m_\chi}{10\ \mathrm{GeV}}\right)^{3/4}. \tag{1.40}$$

The current value assumed by (1.40) is $\frac{t_\oplus}{\tau} = \mathcal{O}(1)$. Equilibrium cannot, hence, be stated with certainty.

Sun

Searches for DM annihilation in the Sun are more sensitive to spin-dependent scattering, mainly because of its light nuclear composition and the dominant contribution of H ions. The capture rate is, both for SI and SD interactions, several orders of magnitude higher than the values for the Earth. For the case of the Sun we can assume, in (1.37), $\tanh^2(t/\tau) \sim 1$, since we have:

$$\frac{t_\odot}{\tau} = t_\odot C_\mathrm{C} C_\mathrm{A} = 330 \left(\frac{C_\mathrm{C}}{\mathrm{s}^{-1}}\right)^{-1/2} \left(\frac{\langle \sigma_\mathrm{A} v \rangle}{\mathrm{cm}^3 \mathrm{s}^{-1}}\right)^{-1/2} \left(\frac{m_\chi}{10\ \mathrm{GeV}}\right)^{3/4}. \tag{1.41}$$

Hence, for the Sun, equation (1.31) becomes:

$$C_\mathrm{C} = \frac{1}{2}\Gamma_\mathrm{A}, \tag{1.42}$$

The process of capture and annihilation is thus in equilibrium and the annihilation rate is at its maximum.

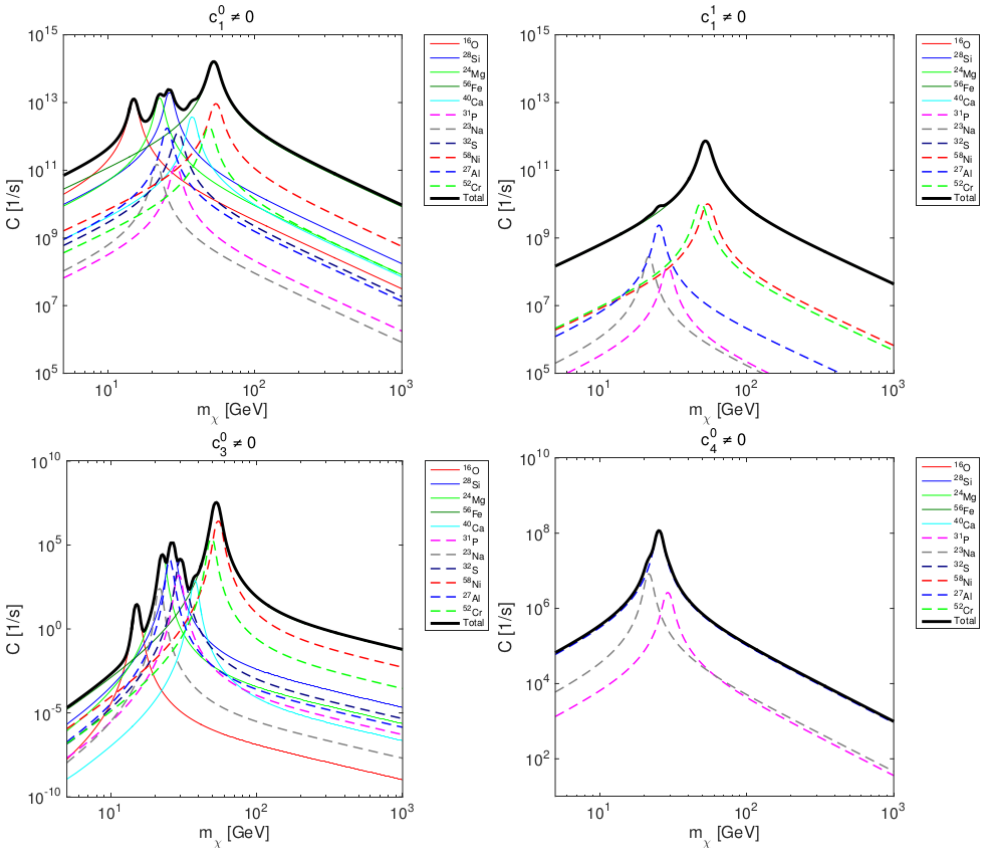

Figure 1.10 – Earth capture rates for selected EFT operators. Showed here are the iso-scalar and iso-vector components of $\mathcal{O}_1$ (top left and right, repsectively), and the iso-scalar components for $\mathcal{O}_3$ (bottom left) and $\mathcal{O}_4$ (bottom right). From [61]. The complete set of EFT capture rate plots can be found at [61].

1.6 Dark matter detection

For dark matter to be detectable, some kind of interaction between DM and SM matter is needed. A model that does not predict such interactions would be considered of no interest since there is no mean to prove it. There are three ways of detecting DM. When DM particles interact between themselves or decay, the products of these processes can be SM particles, which are, in principle, detectable by any kind of particle detector. This is the principle of indirect dark matter detection. When DM particles interact directly with SM particles, the effects (for example, recoil) produced on the SM particles are observable. This is direct dark matter detection. Attempts can be made at producing DM particles in the interaction of SM particles. This is what can be done in high-energy particle colliders. The following paragraphs will present these three types of detection in more detail. A scheme resuming the possible interactions involving dark matter can be found in fig. 1.11.

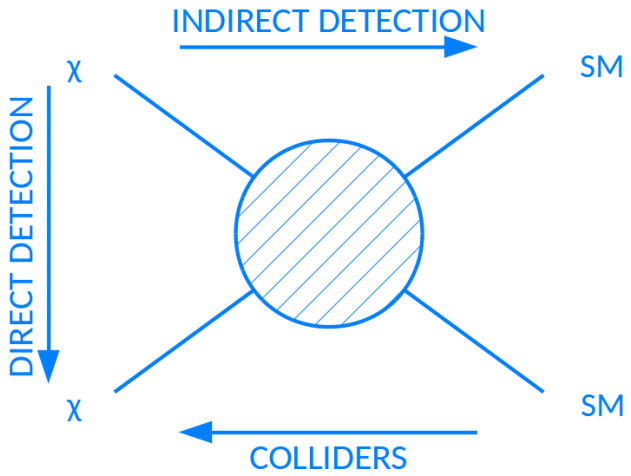

Figure 1.11 – Representation of the possible interactions between DM (χ) and SM particles. For each case, time follows the direction of the arrow. Indirect searches look for SM products of DM-driven interactions. Direct searches detect the recoil effect from scattering of DM off SM particles. Colliders aim at producing DM via the interaction between SM particles.

1.6.1 Indirect detection

DM particles can interact to form, or decay into, SM particles. For the case of the lightest neutralino, which is a Majorana particle, a couple of DM particles can self-annihilate into a couple of SM particles. Indirect detection aims at detecting the particles produced in these processes or the secondary products of the interaction. Generally, this kind of observation looks for regions where a high DM population is expected, such as the Galactic Centre or the dwarf spheroidal galaxies (dSphs). For this kind of source, experiments aim to measure the velocity averaged self-annihilation cross-section $\langle \sigma_{\mathrm{A}} v \rangle$.

Analyses to search for an excess of gamma-rays from the Galactic Centre and dSphs have been performed with many telescopes such as H.E.S.S. [20], Fermi-LAT [23], MAGIC [42] and VERITAS [47]. Interesting results have come from the combination of multiple experiments in recent years [35] [116]. It is worth remarking that Fermi-LAT has observed an excess from the Galactic Centre [16] that could be explained by dark matter [24], though a variety of standard physics explanations have been given [64], too. A resuming plot of gamma-ray limits to $\langle \sigma_{\mathrm{A}} v \rangle$ is shown in fig. 1.12.

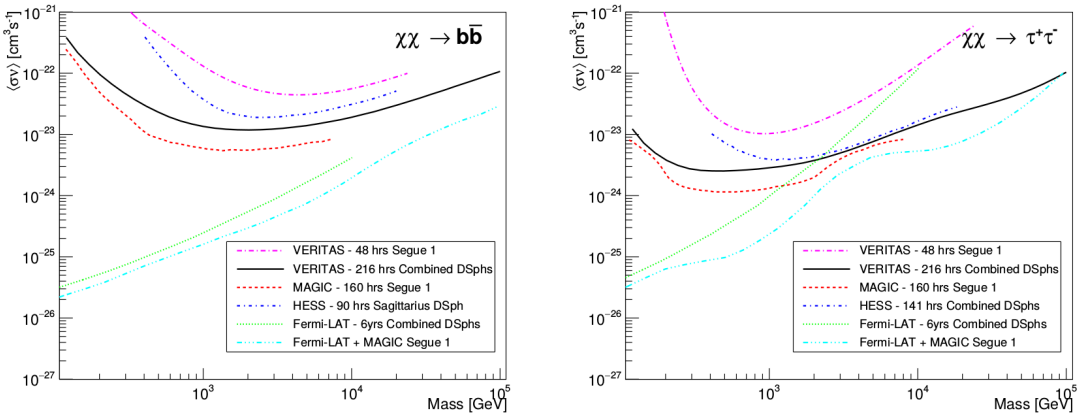

Figure 1.12 – Limits to the self-annihilation cross-section from gamma-ray telescopes. From [47].

Neutrino telescopes can detect an excess of neutrinos from potential DM sources. Neutrinos are among the secondary particles produced in DM self-annihilation and decay. Analysis have been performed by the Cherenkov neutrino telescopes IceCube [4], ANTARES [39], Baikal-NT200 [48] and Super-Kamiokande [21]. Fig. 1.13 shows the current limits from neutrino telescope searches.

As explained in 1.5, dark matter particles may also become gravitationally trapped inside massive celestial bodies such as the Sun or planets such as the Earth (see 1.5.4) after scattering off SM particles and losing velocity. An excess of neutrinos coming from the centre of celestial bodies can be detected by the Cherenkov neutrino experiments. Searches have been performed for the Sun [9] [28] [66] and the Earth [12] [40] [110].

The secluded dark matter model predicts that WIMPs in the Sun self-annihilate into a non-standard mediator, which can escape the Sun before decaying into SM particles [51]. This effect enhances the detectable DM flux by the neutrino experiments since it strongly limits the attenuation of the signal. Results have been produced for this DM model by ANTARES [27] and IceCube. Dark matter results from IceCube will be shown in detail in 3.6.

Cosmic rays measurements also proved to be an interesting probe in the dark matter quest [95]. The challenges in this kind of search come from the fact that cosmic rays are charged particles hence they do not point back to the source where they were generated. Also, cosmic rays lose energy via interactions along their path to Earth, limiting the dark matter searches to the most nearby sources, like the galactic centre and halo. What can be done in this case is to look for an anti-matter excess in the cosmic-ray flux. The latter

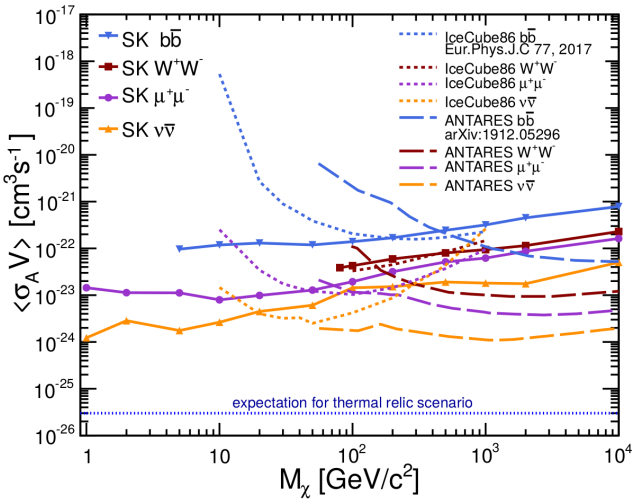

Figure 1.13 – Velocity averaged self-annihilation cross-section for neutrino telescopes. From [21].

could indicate the presence of dark matter since the expectations of anti-matter from astrophysical sources are low. Space satellite experiments, such as PAMELA [29] and AMS02 [22], have indeed measured a positron excess above ~ 10 GeV and up to the TeV region that can be interpreted as evidence for dark matter, although astrophysical explanations (e.g. nearby pulsar wind nebulae) cannot be excluded.

1.6.2 Direct detection

Direct detection [56] experiments aim at detecting the recoil of dark matter particles scattering off SM nuclei. These experiments exploit the fact that the Sun and the Earth are moving in the DM halo, favouring the interaction. Recoil can be detected in a target material in underground laboratories. The need to be underground is to reduce the background from cosmic ray interactions in the atmosphere.

Direct detection of a recoil event may be difficult because of the multiple backgrounds producing similar effects. Since the Earth is rotating around the Sun, thus, alternating parallel and anti-parallel motion with the Sun's motion, the signal shall have an annual modulation and the total observed events can be expressed as:

$$S(t) = B(t) + S_0 + S_m \cos(\omega(t - t_0)), \tag{1.43}$$

where S_0 and S_m are the amplitudes of the constant and modulated signal, respectively, and $S_m/S_0 \sim 0.05$. The background $B(t)$ is typically much larger than the signal, so the annual modulation gives an advantage in detecting signal, though the effect is relatively small.

Spin-independent cross-section limits have been set by a number of experiments, such as DarkSide-50 [31] [32], LUX [36] [37], XENONIT [45], CDEX [107] and many more. A summary plot is shown in figure 1.14.

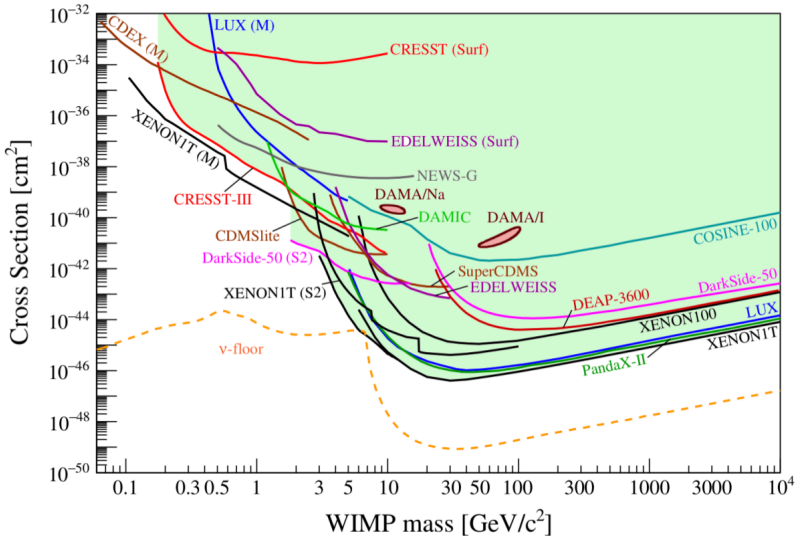

Figure 1.14 – Spin-independent cross-section limits from direct detection experiments. From [56].

The NaI(Tl) crystals array experiment DAMA/LIBRA claimed [53] the detection of an annual modulation signal at 12.9σ level. Although there are not yet plausible alternatives to the DM hypothesis explanation, no other experiments have confirmed this detection, and many experiments have set limits that exclude the DAMA detection region by orders of magnitude. These results are not explicable with the classic spin-independent scattering. Experiments such as COSINE-100 [25], being constituted of the same crystal target material, aim at probing alternative DM models [79] that would justify the sole detection by DAMA.

The most sensitive experiments to the spin-dependent cross-section are bubble chambers with ^{19}S as the target material. The current best limits on the spin-dependent WIMP-proton cross-section are from the PICO [43] experiment, while for the spin-dependent WIMP-nucleon cross-section the strongest constraints are from XENONIT [46].

1.6.3 Production in colliders

Scenarios of particle dark matter production are probed in hadron colliders. At the Large Hadron Collider (LHC) [78], various experiments have investigated this path. The principle is that the products of dark matter annihilation or decay could be non-detectable. This kind of search is, thus, complementary to the direct and indirect searches for dark matter.

Generally, dark matter particles could be produced as decay products of a heavy energetic boson. In the so-called *Higgs portal*, a Higgs boson can decay into dark matter particles. The current limits allow, in fact, for up to a 20% branching fraction of decay to invisible particles. Other models include the decay of new bosonic mediators into dark matter.

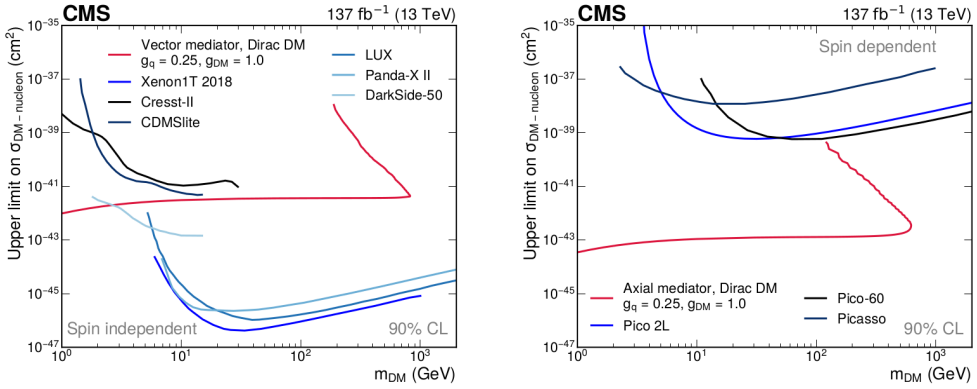

Figure 1.15 – Comparison of the latest limits [140] from the CMS tracker experiment obtained assuming $g_{\mathrm{q}} = 0.25$ and $g_{\mathrm{DM}} = 1.0$ with direct search limits. Left: Spin-independent cross-section. Right: Spin-dependent cross-section.

The detection of invisible particles in a collider needs a visible signature. Signal candidates can be identified with a corresponding missing quantity, for example with the presence of energetic hadronic jets accompanying an invisible particle and with the measure of a large missing transverse momentum p_T^{miss}. Also, collider results are strongly model-dependent.
Fig. 1.15 shows recent results [140] from the CMS experiment at the LHC, for spin-independent and spin-dependent couplings, in comparison with direct detection results. The limits shown were obtained assuming that dark matter particles are Dirac fermions, with the mediator couplings to quarks and dark matter set at $g_{\mathrm{q}} = 0.25$ and $g_{\mathrm{DM}} = 1.0$, respectively

CHAPTER 2

NEUTRINO: A UNIQUE PARTICLE

In a tree by the brook there's a songbird who sings
Sometimes all of our thoughts are misgiven

Neutrinos were postulated in 1930 by W. Pauli [119] to explain the continuous spectrum of beta-decay electron [80]. Neutrino characteristics of charge neutrality and only weak interaction made it impossible, at the time, to prove its existence. Neutrinos were finally discovered only in 1960 [127]. Afterwards, a crescent number of experiments managed to measure neutrinos from radiochemical processes and those produced in the atmosphere. The first detection of neutrinos from out of the solar system came with supernova 1987A [146].

For their characteristics, neutrinos are unique probes for the high energy universe, since they are not subject to interactions of any kind until their detection. This means that neutrinos directly point towards the source in which they were generated and bring information about physics happening in dense environments: neutrinos can only be produced in hadron interactions, so they are the key to the discovery of cosmic ray sources.

This chapter aims at summarising the main physics characteristics of neutrinos: how they are inserted in the context of the Standard Model, the unique process of neutrino oscillations, the main neutrino interactions in matter and the consequences of these interactions.

2.1 Neutrino in the Standard Model

Neutrinos are fundamental particles of the Standard Model of particle physics. As previously mentioned, neutrinos are electrically neutral fermions and have a small rest mass compared to the other fundamental particles. They can interact only weakly with other particles, thus, their coupling with other particles is small compared to particles which can couple electrically or strongly. Hence, neutrinos travel through matter with a low

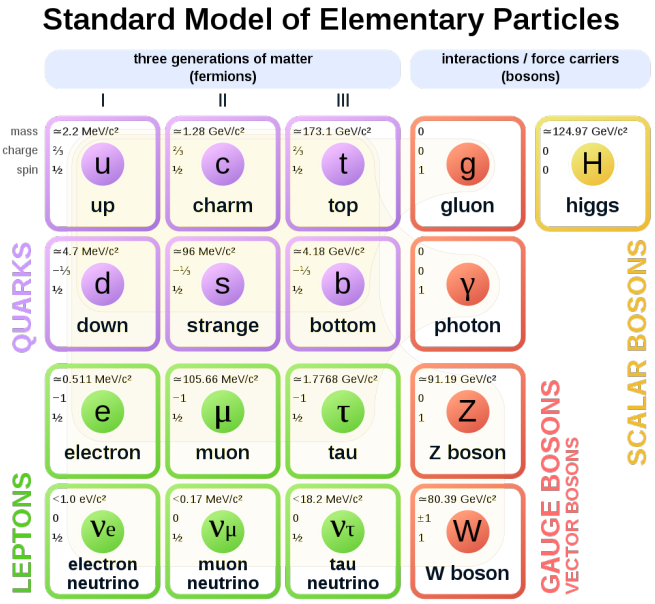

Figure 2.1 – Table of the fundamental particles of the Standard Model. From [112]

chance of interacting. These characteristics make them unique particles to observe astrophysical phenomena, as they can reach the detector from dense and far environments, still carrying the information on their origin in the incoming direction.

In the Lagrangian density $\mathcal{L}$ of the Standard Model, neutrinos are included [136] as three eigenstates ν_i ($i = 1, 2, 3$), also referred to as neutrino mass eigenstates. Neutrinos are, though, observed in flavor eigenstates ν_α ($\alpha = e, \mu, \tau$), which are linear superpositions of the mass eigenstates following

$$\nu_\alpha = U_{\alpha i}\nu_i, \tag{2.1}$$

where $U_{\alpha i}$ is the unitary Pontecorvo-Maki-Nakagawa-Sakata (PMNS) matrix (see (2.2)). The three flavour states are associated with the charged leptons e, μ and τ, as shown in fig. 2.1.

In the Standard Model, neutrinos are predicted to be massless. However, the measure of neutrino oscillations, both in solar and atmospheric neutrinos, proved that neutrinos have mass, although it is small in comparison with the other fundamental particles. The mass of neutrinos is still unknown but constraints can be set through oscillation studies and cosmology observations.

2.1.1 Neutrino oscillations

Neutrino oscillation is a process for which, during propagation, neutrino flavour transitions occur. It was predicted in 1958 by Pontecorvo [126] and measured for the first time by Super-Kamiokande in 1998 [102]. Oscillation is a consequence of the fact

that the mass eigenstates are linear combinations of the mass eigenstates. This relation between the flavour and mass eigenstates is described by the PMNS matrix [136]:

$$U = \begin{pmatrix} 1 & 0 & 0 \\ 0 & c_{23} & s_{23} \\ 0 & -s_{23} & c_{23} \end{pmatrix} \begin{pmatrix} c_{13} & 0 & s_{13}e^{-i\delta_{CP}} \\ 0 & 1 & 0 \\ -s_{13}e^{i\delta_{CP}} & 0 & c_{13} \end{pmatrix} \begin{pmatrix} c_{12} & s_{12} & 0 \\ -s_{12} & c_{12} & 0 \\ 0 & 0 & 1 \end{pmatrix} \begin{pmatrix} e^{-i\rho_1} & 0 & 0 \\ 0 & e^{-i\rho_2} & 0 \\ 0 & & 1 \end{pmatrix}, \tag{2.2}$$

where $c_{ij} = \cos\theta_{ij}$ and $s_{ij} = \sin\theta_{ij}$. δ_{CP} is the CP-violating phase and the last term is only present if neutrinos are Majorana particles and not relevant for oscillation. To the present, there is no evidence for neutrinos to be Dirac or Majorana particles. Two more parameters are given by the masses of ν_1, ν_2 and ν_3, as oscillation depends on the difference of the squared masses $\Delta m^2_{ij} = m^2_i - m^2_j$.

Neutrino oscillations in vacuum can be described via the distance covered by the neutrino, L, and the neutrino energy, for which, considering $m_\nu \ll E_\nu$, we can write:

$$E_\nu = p_\nu + \frac{m^2_\nu}{2p_\nu}, \tag{2.3}$$

and the probability of flavour transition from flavour α to β can be expressed as:

$$P_{\nu_\alpha \to \nu_\beta}(E_\nu, L) = \sum_{i=0}^{3}\sum_{j=0}^{3} U^*_{\beta,i}U^*_{\alpha,j}U_{\alpha,i}U_{\beta,j}e^{-i\Delta m^2_{ij}L/2E_\nu}. \tag{2.4}$$

The presence of masses in the form of squared mass differences Δm^2_{ij} makes it impossible to measure single masses with oscillation studies.

Another unresolved question for neutrinos is the Neutrino Mass Hierarchy (NMH) problem, namely the order of the masses. The mass difference Δm^2_{31} is estimated from solar oscillation observations and it is smaller than Δm^2_{32}, measured with atmospheric neutrino oscillations. The unknown is which of the two represents the difference between the bigger masses. This fact leaves two open possibilities for the NMH: Normal Ordering (NO), if $\Delta m^2_{32} > 0$, and Inverted Ordering (IO), if $\Delta m^2_{32} < 0$. Equation (2.4) can be rewritten [136] in the form:

$$\begin{aligned} P_{\nu_\alpha \to \nu_\beta}(E_\nu, L) = \delta_{\alpha,\beta} - 4\sum_{i=0}^{2}\sum_{j=i+1}^{3} \Re\{U^*_{\beta,i}U^*_{\alpha,j}U_{\alpha,i}U_{\beta,j}\}\sin^2\left(\frac{\Delta m^2_{ij}L}{4E_\nu}\right) \\ \pm 2\sum_{i=0}^{2}\sum_{j=i+1}^{3} \Im\{U^*_{\beta,i}U^*_{\alpha,j}U_{\alpha,i}U_{\beta,j}\}\sin\left(\frac{\Delta m^2_{ij}L}{2E_\nu}\right), \end{aligned} \tag{2.5}$$

where the $+$ and $-$ sign in the second term indicate neutrinos and anti-neutrinos, respectively.

Sensitivity to the NMH in Equation 2.5 can be reached in two ways [105]. The real term of the equation contains a $\sin^2$ term, thus, it is not sensitive to the sign of

Δm^2. Observing multiple oscillation channels at the same time would make it possible to measure all the three Δm^2 parameters, so the NMH could be established by finding which is the bigger between Δm^2_{31} and Δm^2_{32}. The imaginary term is sensitive to the sign of Δm^2, and it is only present when $\delta_{CP} \neq 0$.

Oscillation in matter

When propagating through matter, neutrinos are exposed to an electron density. To describe neutrino oscillation in matter, hence, we need to add a potential term for the electron-neutrino interactions to the neutrino Hamiltonian [93]. The added term gives rise to two effects: the parametric enhancement and the resonant enhancement. The latter is also called Mikheyev-Smirnov-Wolfenstein (MSW) effect [111] [145]. In the two flavours limit and for a constant local electron density N_e, the MSW effect can be described analytically. The Δm^2 parameter and the oscillation angle θ in vacuum can be rewritten as:

$$\Delta m^2 \rightarrow \Delta m^2_m = C\Delta m^2. \tag{2.6}$$

$$\sin(2\theta) \rightarrow \sin 2\theta_m = \frac{\sin 2\theta}{C}, \tag{2.7}$$

with:

$$C = \sqrt{(\cos(2\theta) - A)^2 + \sin^2(2\theta)}, \tag{2.8}$$

where A is:

$$A = \pm\frac{2\sqrt{2}G_F N_e E_\nu}{\Delta m^2}, \tag{2.9}$$

where G_F is the weak force coupling constant. Maximal resonance happens when the first term in (2.8) vanishes so that

$$E_\nu = \pm\frac{\Delta m^2}{2\sqrt{2}G_F N_e}\cos(2\theta). \tag{2.10}$$

For neutrinos travelling through the Earth core, typical resonance energies are $E_\nu \sim 1 - 10$ GeV [113].

2.2 Neutrino flux at Earth

In this section, we want to give a picture of the expected neutrino flux at Earth. As visible in figure 2.2 [142], the sources of the neutrino flux are multiple and the range of energies is extremely wide, over 24 orders of magnitudes in the eV scale. The lowest energy neutrinos come from the so-called Cosmic Neutrino Background (CNB), which has not been detected yet and is predicted to be blackbody radiation in the meV range. On the other hand, the highest, undetected, flux is the cosmogenic neutrino flux. This flux is predicted to be produced in very high-energy cosmic ray interactions and to be at energies above the PeV. In the middle, a plentiful number of different fluxes originated in the most various processes contributes to the unified spectrum. Among the main features are neutrinos from the Sun, which are dominant in the eV - MeV region at Earth. Neutrinos produced in ultra-high-energy cosmic ray (UHECR) interactions in the

Earth's atmosphere, also called *atmospheric neutrinos*, are dominant up to 100 TeV and constitute a major background in searches for astrophysical neutrinos. Astrophysical neutrinos were detected by the IceCube Neutrino Telescope [1] for the first time in 2013 as a diffuse flux. Since then, neutrino telescopes have focused mainly on the search for the sources where these neutrinos are produced. More details on the IceCube main results will be given in chapter 3. Each component will be presented singularly in the following paragraphs, starting from the lowest energies up to the highest.

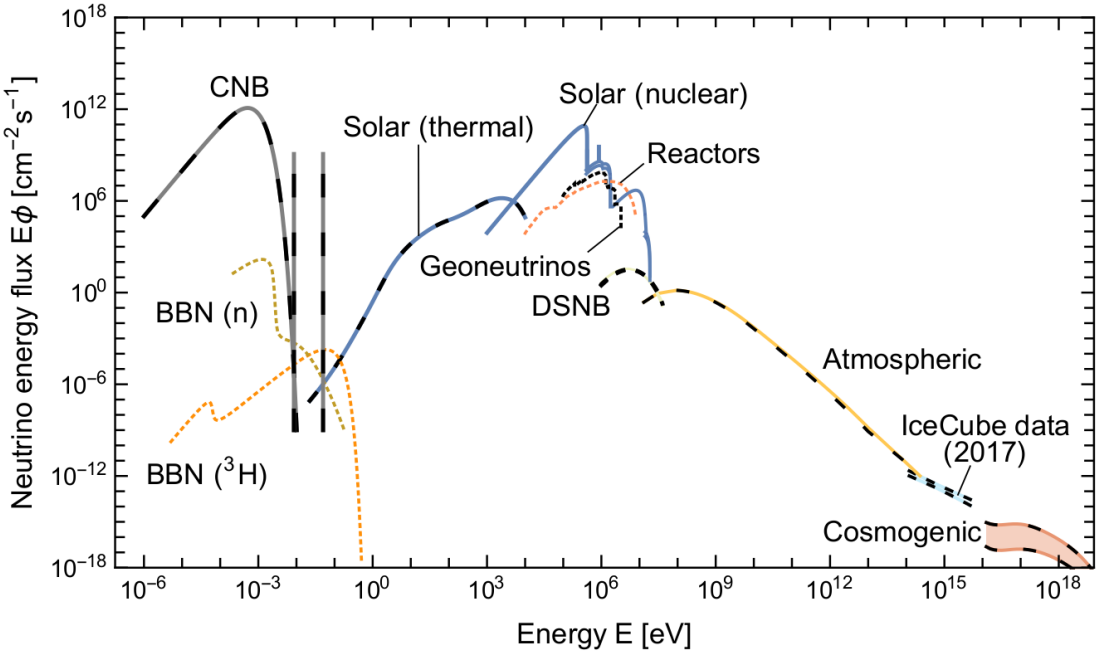

Figure 2.2 – Grand Unified Neutrino Spectrum from [142]. The CNB is represented as a blackbody plus two monochromatic lines at the massses m_1 and m_2 of the minimal mass spectrum $m_1, m_2, m_3 = (0, 8.6, 50)$ meV. Dashed lines indicate anti-neutrino fluxes. Sources which emit both neutrinos and anti-neutrinos have superposed continuous and dashed lines. The various components of this spectrum also include BBN neutrinos (see 2.2.1), solar neutrinos (see 2.2.2), geoneutrinos (see 2.2.3), supernova neutrinos (see 2.2.4), neutrinos produced in atmospheric cosmic-ray interactions and from astrophysical sources (see 2.2.5), and cosmogenic neutrinos (see 2.2.5).

2.2.1 Primordial neutrinos

The lowest energy neutrinos predicted are those of the Cosmic Neutrino Background. In the early Universe, at cosmic temperature T above a few MeV, neutrinos are in thermal equilibrium with the other particles, namely photons, nucleons and other leptons. Neutrinos at this epoch follow a Fermi-Dirac distribution. At $T \simeq 1$ MeV, the neutrino interaction rate slows below the expansion led by the Hubble constant H, i.e. neutrinos freeze out. Since neutrino masses are small, their distribution is still Fermi-Dirac. At

$T \simeq 0.1$ MeV electrons and positrons annihilate into photons, so that the photon temperature rises. At this point, in the adiabatic limit, one finds that the relation between the neutrino and photon temperature, T_ν and T_γ, respectively, is described by:

$$T_\nu = \left(\frac{4}{11}\right)^{1/3} T_\gamma, \tag{2.11}$$

which, considering the current epoch CMB temperature $T_{\gamma,0} = 2.725$ K, gives a present day CNB temperature of $T_{\nu,0} = 1.945$ K.

The so-called Big-Bang nucleosynthesis (BBN) happened a few minutes after the Big-Bang and produced light elements. A small flux of electron anti-neutrinos is expected from the decay of neutrons and tritiums generated in the BBN, via the processes $n \to p + e^- + \bar{\nu}^e$ and ${}^3\mathrm{H} \to {}^3\mathrm{He} + e^- + \bar{\nu}^e$. Although the predicted flux is small, it fills a gap between the CNB and the Sun thermal production, at energies in the $10 - 100$ meV range. BBN anti-neutrino detection would open a window on the primordial nucleosynthesis, however, given their low energies and minimal interaction cross-section, detection of these neutrinos is beyond the current detection techniques, although efforts are in place to detect the CNB neutrinos [68] [55].

2.2.2 Solar production

The Sun is the major source of detectable neutrinos [142] coming to the Earth due to its proximity. The study of solar neutrinos has been a key in the discovery of neutrino flavour oscillations [102]. Neutrinos are produced both in the proton-proton (pp) and Carbon-Nitrogen-Oxygen (CNO) nuclear fusion cycles. Every ${}^4\mathrm{He}$ nucleus produced implies the conversion of two protons to neutrons via the fusion process $p + e^- \to n + \nu_e$. The effective fusion reaction, considering all the reactions in the two cycles, is $4p + 2e^- \to {}^4\mathrm{He} + 2\nu_e + 26.73$ MeV. The luminosity of the Sun in nuclear reaction neutrinos is $L_{\odot,\nu_e} = 1.83 \times 10^{38}$ s^{-1}. The flux at Earth is, thus, $\Phi_\nu = 6.51 \times 10^{10}$ cm^{-2} s^{-1}.
The Sun also produces neutrinos of all flavours via thermal processes. Though these neutrinos are currently not detectable, this flux is dominant in the ∼eV - ∼keV region. The main components of this flux come from:

- Plasmon decay: $\gamma \to \nu + \bar{\nu}$;
- Compton effect: $\gamma + e \to e + \nu + \bar{\nu}$;
- Bremsstrahlung: $e + Ze \to e + Ze + \nu + \bar{\nu}$.

A hypothetical detection would carry information about the solar chemical composition.

2.2.3 Earth sources

The so-called *geoneutrinos* are anti-neutrinos produced in the decay of natural long-lived radioactive isotopes [142]. The quasi-totality of geoneutrinos comes from the decay of ^{238}U, ^{232}Th and ^{40}K. The resulting $\bar{\nu}_e$ flux peaks in the MeV range and exceeds 10^{25} s^{-1}. Although the flux is superposed to the solar nuclear flux, the distinction of

geoneutrinos is possible given the fact that they are anti-neutrinos. Observation of geoneutrinos allows, in principle, for studying the Earth interior composition. This flux strongly depends on the observation location.

Electron anti-neutrinos at MeV energies are also produced in nuclear power plants and reactors, via β-decay of neutron-rich nuclei. The main components of this flux come from the fission of ^{235}U, ^{238}U, ^{239}Pu and ^{241}Pu. An additional source is due to the neutron capture processes. The main contribution here comes from the decay of ^{239}U formed in a neutron capture to ^{238}U. The total $\bar{\nu}_e$ flux from reactors can be estimated considering that an average power plant of 1 GW of thermal power produces a flux of $\sim 2 \times 10^{20}$ s^{-1} and that the global nuclear thermal power is $\sim$1.2 TW. The reactors flux is in the same energy range and only a few per cent of the geoneutrino flux. However, the reactor contribution can be dominant at specific locations and has a different spectrum, so that it is detectable [142].

2.2.4 Diffuse supernova neutrino background

The compact core of a star at the end of its life collapses to subsequently bounce back, forming a shock-wave outwards which ejects most of the mass of the object in what is called a supernova explosion. A supernova emits roughly $\sim 3 \times 10^{53}$ erg in neutrinos. Photons and electrons do not contribute to the energy transfer because of their large interaction rate in dense matter. The neutrino mean free path in such a hot and dense environment is short compared to the dimensions of the object, therefore neutrinos thermalise via various processes. A supernova can be thought of as a neutrino blackbody [142]. A supernova is a transient source of neutrinos which can be detected, under certain conditions, by neutrino observatories, as it was in the case of Supernova 1987A [146].
The contribution of all supernovae in the visible universe, a few per second, provides a diffuse neutrino background which dominates in a small window, between 10 and 25 MeV. This flux could be detectable by future experiments [142].

2.2.5 Highest energies flux

The *atmospheric* neutrinos are produced in interactions and decays along the extensive air showers induced by the primary interaction of high-energy cosmic rays in the atmosphere. It is the dominant contribution from below the GeV scale up to hundreds of TeV. Many oscillation studies are carried out by studying the atmospheric neutrino flux. The understanding of the atmospheric neutrino flux is also essential because it constitutes the main background for neutrino telescopes. The atmospheric neutrino flux will be discussed in more detail in the context of the event selection for this work in chapter 4.

Astrophysical neutrinos are produced in galactic and extra-galactic sources when the sources are *hadronic*, i.e. they present interactions involving hadrons. The detection of neutrinos from a specific source can therefore indicate the nature of the source itself and the main processes leading in the source environment. IceCube detected a diffuse flux of astrophysical neutrinos, but there is tension on the characterisation of the astrophysical neutrino flux between different analyses. More details on the astrophysical neutrino flux measured with IceCube will be given in 3.5. The difficulties in identifying the astrophysical neutrino sources lie in the limited number of astrophysical neutrino events that a 1 km^3 neutrino telescope is able to detect and in the limits of the angular

resolution of neutrino telescopes. However, with a *multi-messenger* approach, detection of neutrino events in correspondence with γ-rays or gravitational waves detection considerably raises the significance of even a single neutrino event detection. More details on this argument will be given in 3.5.

A further contribution of *cosmogenic* neutrinos could be due to ultra-high-energy cosmic-rays (UHECR) of energy around $\sim 10^{20}$ eV interacting with the CMB or the extra-galactic background light (EBL). If the Lorentz factor is $\Gamma \geq 10^{10}$ the UHECRs interact with the CMB, otherwise, they can interact with the EBL. If UHECR are moslty protons, pions can be produced in photo-pion interactions via the Δ resonance following $p + \gamma \rightarrow \Delta \rightarrow p + \pi^{0,\pm}$ which, for an atom of atomic number N, can be written as $N + \gamma \rightarrow N + \pi^{0,\pm}$. Photo-pion interactions are responsible for the so-called Greisen-Zatsepin-Kuzmin (GZK) effect, which is a predicted [91] [148] cut-off of UHECRs at high energies. If UHECR are heavier nuclei, photo-disintegration can happen. In this interaction the UHECR loses one or more nucleons following $(A, Z) + \gamma \rightarrow (A - n, Z - n') + nN$, where n and n' are the number of lost nucleons and protons, respectively. The flux of cosmogenic neutrinos carries uncertainties due to the unknown composition of UHECR at such energies and the maximum possible UHECR energy [135]. Current limits on the cosmogenic neutrino flux disfavour a light atomic composition of UHECRs. The detection of the cosmogenic flux is one of the goals of the future radio neutrino observatories [34] [72] targeting PeV neutrino detection.

2.3 Neutrino interactions

Neutrinos interact only via the weak force. At low energy, multiple types of interaction contribute to the total cross-section [83]. The most relevant interaction at energies $E_\nu \lesssim 2$ GeV are the quasi-elastic (QE) and elastic scattering; in an intermediate region with neutrino energy of a few GeV the leading process is the resonance scattering; for $E_\nu \gtrsim 10$ GeV, deep-inelastic scattering (DIS) is dominant.

Generally, neutrino interactions can be divided into charged current (CC) and neutral current (NC) interactions. CC is verified when a charged lepton is present in the final state, NC when there is a neutrino.

QE scattering is a CC process where a neutrino scatter off an entire nucleus [83]. Considering the leptonic flavour α, for a (anti-)neutrino we can write:

$$\overset{(-)}{\nu}_\alpha + n(p) \rightarrow \alpha^{-(+)} + p(n); \tag{2.12}$$

NC elastic scattering of a (anti-)neutrino off a nucleon can be described with:

$$\overset{(-)}{\nu}_\alpha + N \rightarrow \overset{(-)}{\nu}_\alpha + N, \tag{2.13}$$

being N a nucleon n or p.

Resonant scattering happens when a neutrino has sufficient energy to excite a nucleon [83]. This process produces a baryon resonance N^* which quickly decays, mainly to a pion and a nucleon. We can write the interaction as:

$$\nu_\alpha + N \rightarrow \alpha^- + N^* \tag{2.14}$$

$$N^* \rightarrow \pi + N', \tag{2.15}$$

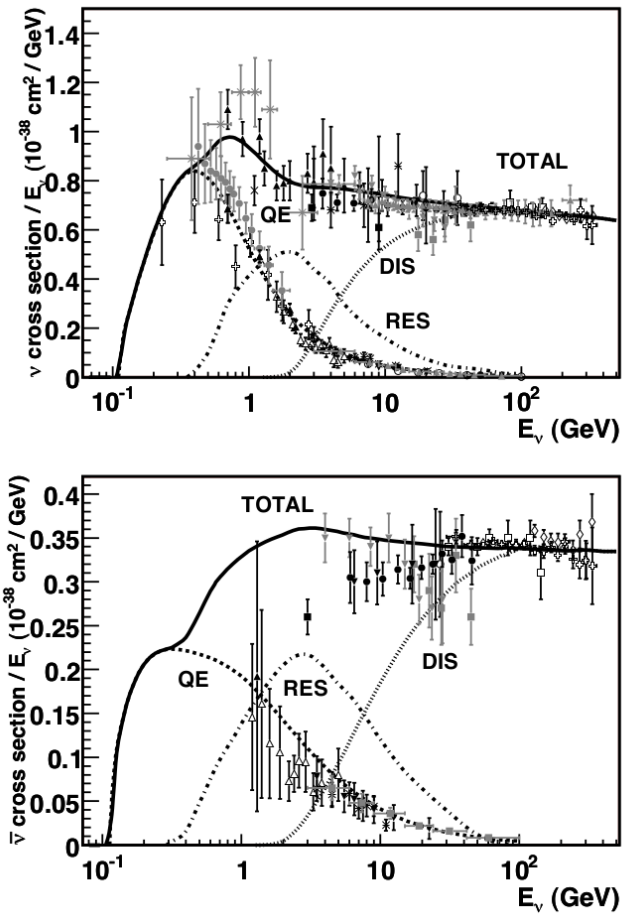

Figure 2.3 – Overview of the neutrino (top) and anti-neutrino (bottom) interaction cross-section as a function of the neutrino energy. From [83].

where $N, N' = n, p$. The pion and nucleon can generate a hadronic shower in a similar way to DIS, which will be described in the following.

When the neutrino energy is above $E_\nu \sim 10$ GeV, the dominant interaction is scattering off a single quark inside a nucleon [83], in a process called deep-inelastic scattering. The interaction occurs via exchanging a W or Z boson, for CC and NC processes, respectively. The final state is composed of a lepton and a hadronic system. For a neutrino we can write:

$$\nu_\alpha + N \to \alpha^- + X \ (\mathrm{CC}), \tag{2.16}$$

$$\nu_\alpha + N \to \nu_\alpha + X \ (\mathrm{NC}), \tag{2.17}$$

where X represents the hadronic system and α a leptonic flavour, as usual. The hadronic system in the final state generates a shower of particles that can be detected via the observation of the *Cherenkov effect* (see below). Charged leptons in the final state can also be detected in the same way. Analogous expressions can be written down for anti-neutrinos. The neutrino-nucleon cross-section can be written as a function of the

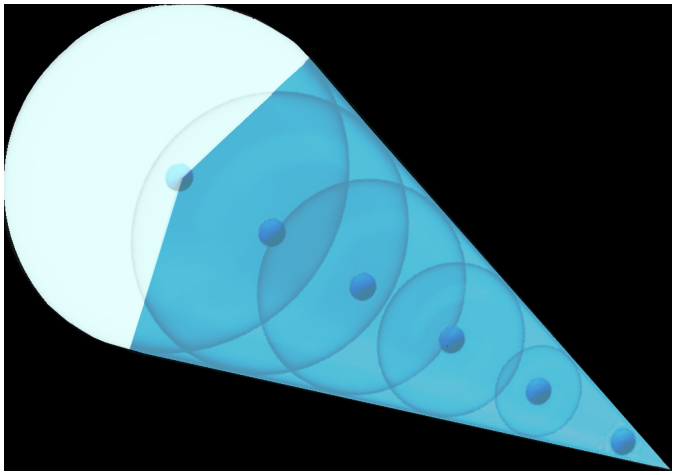

Figure 2.4 – Illustration of the Cherenkov effect. The waveforms interfere coherently to form a cone-shaped front of light with characteristic angle θ_C, which is the angle between the radius of the spheres tangent to the cone and the cone axis. The particle, represented by a little blue sphere, is drawn at different positions in time, where the latter flows towards the vertex of the light-cone.

inelasticity parameter $y = E_X/E_\nu$ [136] as:

$$\frac{d^2\sigma^{\nu N}}{dxdy} = \frac{G_F^2}{\pi} sx \left[f_q(x) + (1-y^2) f_{\bar{q}}(x)\right] \tag{2.18}$$

$$\frac{d^2\sigma^{\bar{\nu} N}}{dxdy} = \frac{G_F^2}{\pi} sx \left[(1-y^2) f_q(x) + f_{\bar{q}}(x)\right], \tag{2.19}$$

where G_F is the weak force coupling constant, $\sqrt{s}$ is the center-of-mass energy, and f_q and $f_{\bar{q}}$ are, respectively, the quark and antiquark parton distribution functions for a nucleon. As expected, and as shown in fig. 2.3, in the DIS dominated region the cross-section is linearly dependent on the neutrino energy. The analysis described in this work is mostly contained in this region. Fig. 2.3 only shows the cross-section up to ~ 500 GeV. At higher energies there are no measurements and the cross-section must be inferred from the considerations just mentioned.

2.4 The Cherenkov effect

When a charged particle travels in a dielectric medium at speed higher than the medium phase velocity, an electro-magnetic radiation is emitted in the form of spherical waveforms. The latter will propagate in the medium with its phase velocity, $v_{ph} = c/n$, where n is the refractive index. The polarisation of the molecules will re-orient following the electromagnetic field of the passing charged particle. Photons are produced by the molecules returning from the excited state to the ground state with a random polarisation. When a charged particle is travelling faster than the speed of light in the medium v_{ph},

the wave fronts will superpose and the photons will interfere constructively to form a cone of light. The first to observe and describe this phenomenon was P.A. Cherenkov in 1934 [63], from which the effect takes the name. The Cherenkov light maximum is in the visible and ultra-violet range.

If we consider the Antarctic ice and the visible range, the refraction index is $n \simeq 1.32$ [11]. We can also consider $\beta = v/c \simeq 1$ for ultra-relativistic particles. The characteristic angle of the light cone, the Cherenkov angle θ_C, is defined with [104]:

$$\cos(\theta_C) = \frac{1}{n\beta} \simeq \frac{1}{n} \simeq \cos(41^\circ). \tag{2.20}$$

The photon spectrum is described by the Frank-Tamm formula [84] [104]:

$$\frac{d^2N}{dxd\lambda} = \frac{2\pi\alpha}{\lambda^2} \sin^2(\theta_C), \tag{2.21}$$

where α is the fine structure constant.
Charged leptons produced in neutrino interactions in ice induce Cherenkov radiation. IceCube can detect the light emitted along the path of passing particles and use it to reconstruct the characteristics of the particle, such as energy and direction. Principles of detection in IceCube will be shown in 3.4.

CHAPTER 3
THE ICECUBE NEUTRINO OBSERVATORY

...I have seen rings of smoke through the trees...

3.1 Introduction

The idea of large volumes filled with an array of photo-multiplier tubes to detect neutrinos was conceived in the late 1950s [108]. Exploiting the Cherenkov effect (see 2.4), i.e. the fact that charged particles produce visible light while travelling at a speed higher than that of light in a medium, charged particles produced in neutrino interactions in a medium can be detected at their passage. The first successful experiments of this kind were Baikal, AMANDA and ANTARES. Although these experiments were not able to measure astrophysical neutrinos produced in sources at cosmological distances, they provided milestone measurements of the neutrino flux produced in the atmosphere and demonstrated the feasibility of such a technique. The non-detection of an astrophysical flux led to the proposal of building a cubic kilometre scale detector to achieve this result.

IceCube is the first cubic kilometre neutrino telescope. It was built under the South Pole ice and its construction ended in 2010. The first breakthrough result was the measurement of the astrophysical flux in 2013 (see 3.5.1). More recently, evidence for some cosmic ray sources was found [5] [6] [10] and a Glashow resonance event was observed for the first time [8] (see 3.5). IceCube also proved to be very competitive in neutrino oscillation physics studies. Indirect detection of dark matter has been among the main objectives of the experiment since its beginnings (see 3.6).

3.2 The detector

The IceCube Neutrino Observatory [13] is a neutrino Cherenkov detector located at the Amundsen-Scott South Pole Station. The main detector is buried in the 3 km thick ice

cap of the pole, at a depth between 1450 m and 2450 m. The depth provides a screen against atmospheric events and sunlight. The South Pole ice offers an excellent medium for Cherenkov light detection. The photon yield, the long optical attenuation length of the material and the large area photo-multipliers (PMTs) permit to have a rather sparse array of detectors. The volume of the detector is 1 km^3. The big volume is necessary for the detection of a significant number of neutrino interactions and it is especially important for the observation of events of astrophysical origin.

The detector units are Digital Optical Modules (DOMs) containing a 10" (25.4 cm) PMT in a glass sphere which protects it from the ice pressure (see 3.2.2). The In-Ice array extends down to the depth of 2450 km and consists of 86 strings of 60 DOMs each. The primary array is composed of 78 strings with a 17 m vertical separation of the DOMs. The strings are composed of a single cable containing twisted copper-wire pairs which link the DOMs to the surface IceCube Laboratory (ICL), where data are read and processed. The strings are deployed in a hexagonal footprint on a triangular grid with a 125 m horizontal spacing between the strings. The design is optimised for the detection of astrophysical neutrinos in the $\mathcal{O}$(TeV)-$\mathcal{O}$(PeV) energy range and it has an energy threshold of ~ 100 GeV.

The DeepCore array is a denser area suited for lower energy events down to a few GeV and will be discussed in more detail in 3.2.1. The detector also includes the IceTop surface array. IceTop stations follow approximately the same grid as the In-Ice strings. Each station consists of two tanks filled with ice and instrumented with PMTs for Cherenkov light detection. The two tanks are separated from each other by 10 m. IceTop is a detector of extensive cosmic ray air-showers and can be used for cosmic rays studies, but also in combination with the In-Ice array as a veto for atmospheric muon background rejection.

3.2.1 The DeepCore sub-array

DeepCore [13] is a denser sub-array specialised for lower energy neutrino detection. It consists of 8 strings. The DOMs vertical spacing for the bottom 50 DOMs is 7 m and the horizontal spacing between the strings varies from 41 m to 105 m, with an average spacing of 72 m. The remaining 10 DOMs of these strings are above 2000 m and have a vertical spacing of 10 m. These DOMs serve as a veto to reduce the atmospheric background of down-going muons. DeepCore is at depths between 2100 m and 2450 m. The layer between 2000 m and 2100 m is not instrumented because of the significantly increased optical scattering and absorption due to a higher presence of dust. This region is thus called the *dust layer*. The DeepCore DOMs have a 35% higher quantum efficiency while 2 of the 8 strings have a combination of standard and higher efficiency DOMs. The DeepCore configuration lowers the energy threshold to a few GeV and is particularly suited for events in the 10-100 GeV energy range. These characteristics increase the ability of the detector for atmospheric neutrino oscillation studies, indirect dark matter and Galactic supernovae detection.

3.2.2 The Digital Optical Module

The Digital Optical Module (DOM) is the fundamental unit of the IceCube detector. It is a downward-facing 10" (25.4 cm) photo-multiplier tube (PMT) housed in a spherical glass. The glass has a 13" (33 cm) outer diameter and is 0.5" (1.27 cm) thick. The

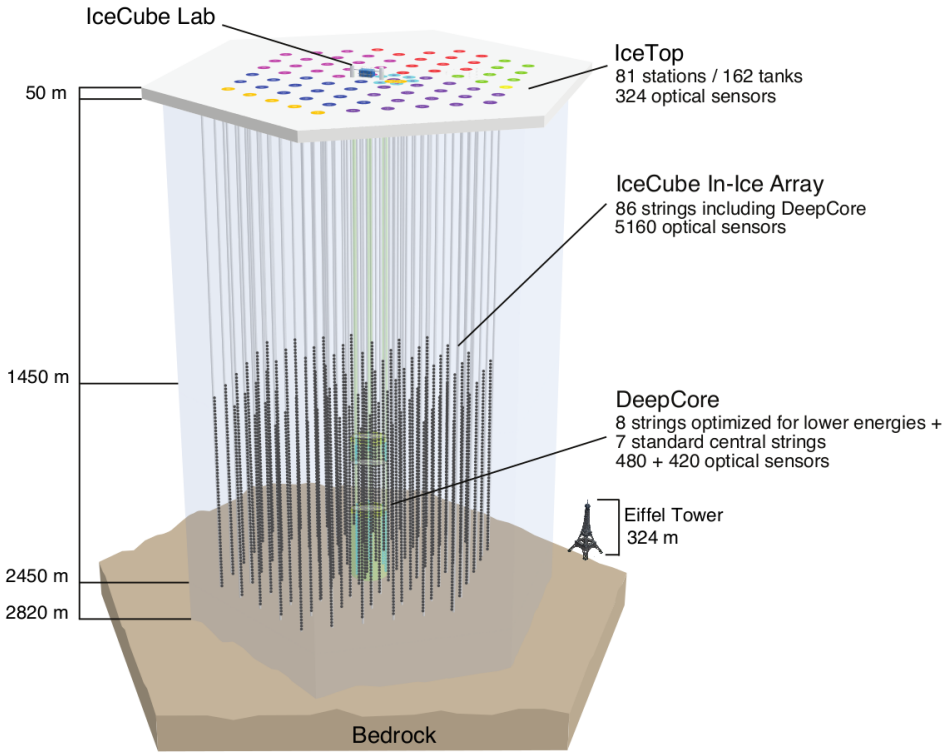

Figure 3.1 – The IceCube Neutrino Observatory with the In-Ice, DeepCore and IceTop arrays. Different colors indicate different seasons of deploying. From [13].

glass has very low radioactive trace elements and it was conceived mainly to protect the PMT from the ice pressure. Long-term ice pressure is 250 bar, but the glass has been projected to resist up to 690 bar, which is higher than the pressure caused by re-freezing ($\sim$ 400 bar) of the hole drilled to put the DOM in place. The PMT is secured by a 1 cm thick silicon gel layer, which provides mechanical support and has good optical coupling with the ice. The Main Board circuit is fixed around the neck of the PMT and it manages data acquisition, control, calibration, communication and low voltage power conversion. Separate circuits are present for high voltage, interface with the PMT pins, delayed signal and calibration light flashes. A mu-metal cage surrounds the PMT bulb to reduce the effect of the Earth magnetic field at the Pole.

A photon detection triggers the DOM to record the PMT waveform ("hit"). With a gain of 10^7, PMTs can have waveforms with amplitudes from 1 mV to $\sim$ 2 V and widths between 12 ns and 1500 ns. The DOM includes multiple digitisers in overlapping dynamic ranges and different sampling speeds to read a variety of signals. Digitisation of waveforms is done using a custom integrated circuit (Analog Transient Waveform Digitizer, ATWD) and a continuously sampling fast ADC (fADC). The ATWD can record photons up to 427 ns, allowing for reconstruction of light produced within $\mathcal{O}$(10 m). Photons arriving from further away are recorded by the fADC, which can record up to a total time of 6.4 μs. Each DOM is equipped with two ATWDs to reduce deadtime.

Data are sent to the surface in 1 s blocks, but a DOM is able to record up to $\sim$ 10 s

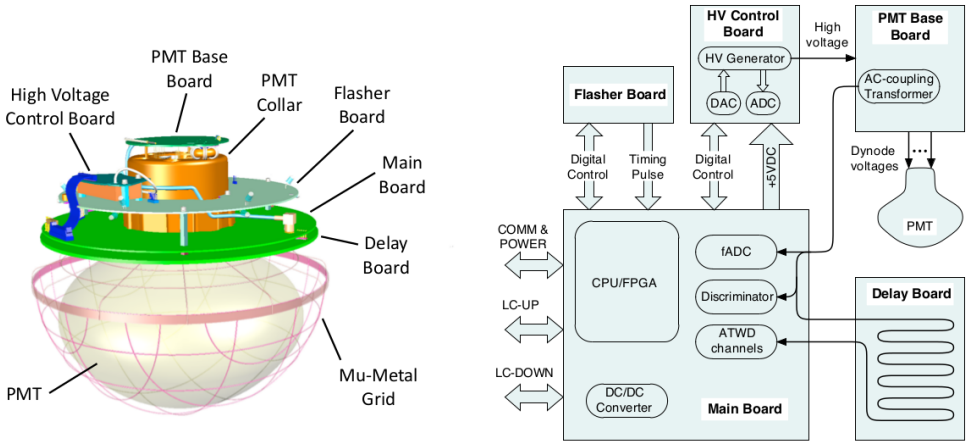

Figure 3.2 – Representation of a DOM. Left: mechanical layout. Right: functional connections. From [13].

of data in case the data readout is interrupted. Power and communication with the ICL are provided by twisted wire pairs which form the vertical In-Ice and the horizontal surface cables. Wire pairs are shared between 2 DOMs. An additional local coincidence wiring to neighbour DOMs is set to detect hits in nearest and next-to-nearest DOMs in a common time window. The span of forwarding is set to 2 DOMs above and below on the string. Data from a local coincidence (Hard Local Coincidence, HLC, hits) are stored in full detail. For single-photon detections (Soft Local Coincidence, SLC) reduced information is saved. The single photo-electron (SPE) discriminator is set to a threshold of 0.25 PE while for larger amplitudes an MPE discriminator is used.

The periodic calibration routine DOMCal is run yearly and monthly for In-Ice and IceTop DOMs, respectively, and provides the constants needed to convert waveforms into physical quantities. The RAPCal procedure provides global calibration across the DOM array and is run during data-taking. The latter translates hit timestamps from the individual DOM clocks to the ICL clocks for subsequent translation into UTC. Regular calibration is fundamental for converting signal into a measurement of Cherenkov light in time, the basis of event reconstruction.

3.2.3 Triggers

Correlated hits in space and time trigger the Data Acquisition System (DAQ). Multiple triggers are set for each component of the detector (In-Ice, IceTop, DeepCore). Correlations help to discriminate possible physics signal from dark noise, which generally consists of casual individual hits. A trigger algorithm searches for a multiplicity of HLC hits in a defined trigger time window and under a certain geometrical constrain.

The fundamental trigger is the Simple Multiplicity Trigger (SMT) which only looks for hits correlated in time all over the detector (or sub-detector). The main IceCube trigger is SMT-8, which requires at least 8 HLC hits in a $5\ \mu s$ time window, The main

DeepCore trigger is SMT-3, which requires at least 3 HLC hits in a $2.5\ \mu s$ time window. Rates for SMT-8 and SMT-3 are 2100 Hz and 250 Hz, respectively.

Spatial correlations allow for a lower threshold. The Volume Trigger fixes a cylinder of given volume around a hit DOM and searches for at least 4 hits in a time window of 1 μs within the cylinder. The String Filter requires 5 hits on 7 adjacent DOMs on a single string.

Similar triggers are set for IceTop and a trigger for slow particles (SLOP) as, for example, magnetic monopoles, is based on more elaborate requirements for an extended time window (500 μs).

For each trigger a readout window is open: in a time window around the trigger, every hit in the entire detector is collected. Triggers activated in the same time window are regrouped in a single Global Trigger, so that a given hit is not collected multiple times. An event is defined as the readout of a Global Trigger. An event at this stage can contain, thus, multiple physics events. The latter are eventually split at later stages of the processing.

3.2.4 Online processing and filtering

Triggered events are handled by the Processing and Filtering (PnF) [13] system in order to select events that are more interesting for physics and reduce the data to a volume that can be transferred to the North via satellite. The PnF calibrates data from DOMs, handles characterisation of the events, generates realtime alerts for potentially interesting astrophysical events, monitors data quality and prepares data for long-term archive storing.

As a first step, data from DOMs are calibrated, using geometry, calibration and detector status (GCD) information stored. Afterwards, the amplitude and time arrival of each photon for each DOM are extracted and stored in a compact format called SuperDST, which introduces a discretisation for both the time and amplitude information, instead of the full waveform. The discretisation error is, however, smaller than the calibration uncertainties. When the SuperDST format is not a good representation of the original waveform or there is a particularly big amount of light the full waveform is saved along the SuperDST. The amplitude and arrival time of photons are essential for event reconstruction.

At this point, event reconstruction algorithms are applied to determine the characteristics of events that could be identified as tracks or cascades. Information such as the interaction vertex coordinates, the direction, energy and goodness-of-fit is used in filtering. Each filter is thought to select events that are interesting for specific kinds of analyses. Events that pass at least one filter are $\sim 15\%$ of the total triggered data.

PnF eventually generates files for filtered data, SuperDST files with all triggered events for long-term archive, and raw uncalibrated DOM waveform data files.

Many filters exist depending on the physics and the purpose of the various analyses in IceCube. Those filters that are relevant for the analysis object of this work will be shortly presented in the following as an example:

- The *MuonFilter* aims at selecting events that can be successfully reconstructed as muon track events. All triggered up-going events with such characteristics are included, while for down-going directions a cut on low energy events is needed to reduce the muon background. Muon tracks have the best direction resolution

(see 3.4), so this selection is often used in searches for point sources and transient sources;

- The *DeepCoreFilter* selects events that have lower energy and are contained in the inner DeepCore volume. Energy for these events is in the $10 - 100$ GeV range. This selection is suited for oscillation studies;
- The *VerticalEventFilter* (VEF) selects muon track events that are nearly vertical and up-going. All events are triggered by the String Trigger and must lie on a single string. This filter was specially developed for the search for dark matter from the centre of the Earth;
- The *LowUp* filter aims at a low-energy, up-going events selection. The filter is particularly suited for indirect dark matter searches and has a muon background rejection of $\sim 99\%$. The selection is potentially fit for atmospheric neutrino studies.

3.3 The South Pole Ice

For a correct interpretation of the detected events, an understanding of the medium in which light propagates is fundamental. The 2.8 km thick South Pole ice cap formed throughout the last 100 000 years. Several layers were superimposed at different ages and the ice characteristics vary by about an order of magnitude among the different layers. The bulk absorption length varies between 30 and more than 200 m, while the effective scattering length is in the 5 m to 70 m range [2]. Optical properties deteriorate in presence of air bubbles and other impurities. The dust layer mentioned in 3.2.1 contains ashes of volcanic origin which degrade the optical properties to the cm scale.

In IceCube, absorption and scattering are described by a set of parameters [11]. The effective scattering is:

$$b(\lambda) = b_e(400) \cdot \left(\frac{\lambda}{400 \text{ nm}}\right)^{-\alpha}, \tag{3.1}$$

where $b_e(400)$ is the scattering at 400 nm and α a fit parameter. Absorption is expressed in the form:

$$a(\lambda) = a_{dust}(\lambda) + Ae - b/\lambda \cdot (1 + 0.01 \cdot \delta T), \tag{3.2}$$

where:

$$a_{dust}(\lambda) = a_{dust}(400) \cdot \left(\frac{\lambda}{400 \text{ nm}}\right)^{-\kappa}. \tag{3.3}$$

$a_{dust}(400)$ is related to the absorption at 400 nm. Parameters A and κ are parameters fit in the detector calibration. Both $b_e(400)$ and $a_{dust}(400)$ vary with depth. δT is the temperature difference between the depth of 1730 m and the considered depth d:

$$\delta T(d) = T(d) - T(1730 \text{ m}). \tag{3.4}$$

The profiles of $b_e(400)$ and $a_{dust}(400)$, as well as δT in the South Pole ice are shown in figure 3.3, according to the *Spice3.2* model, which is the ice model adopted for this analysis. Down to 1300 m the ice shows the presence of air bubbles while, deeper, the

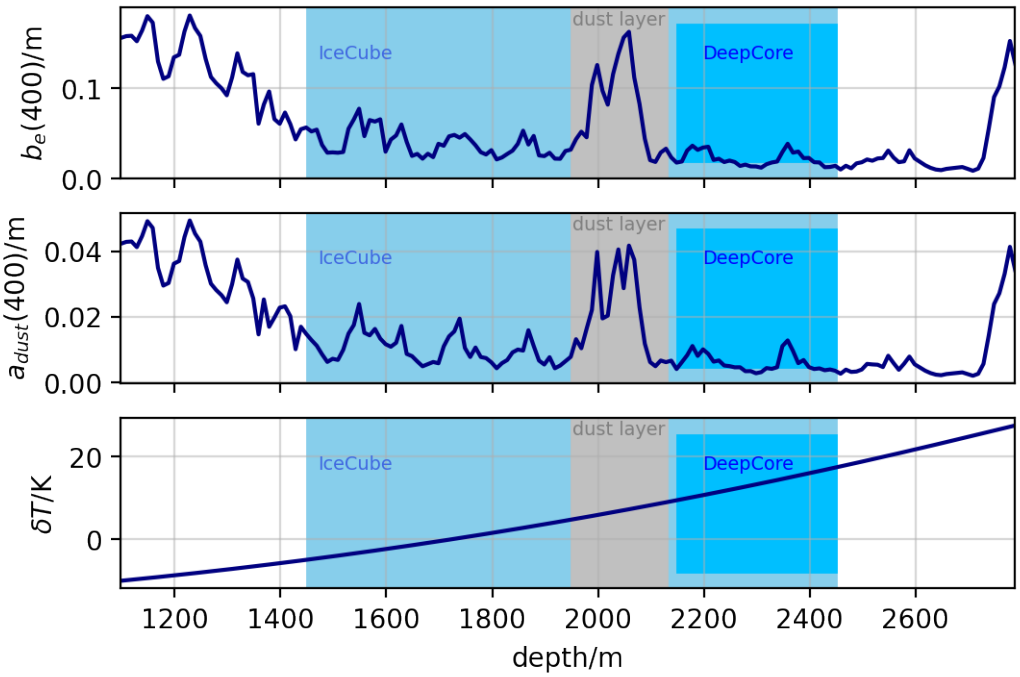

Figure 3.3 – Profiles of $b_e(400)$, $a_{dust}(400)$ and δT in function of the depth for the South Pole ice cap. A clear deterioration of the ice optical properties is seen in correspondence with the dust layer. The depths where DeepCore is deployed show the best optical properties. Figure produced with values taken from the tables describing the ice model used for this work.

pressure made the ice crystals incorporate the air bubbles. As a result, below 1300 m the ice is more transparent.

Another effect to take into consideration is the hole ice effect. Re-frozen ice from the drilling holes where strings were put contains higher contamination of air bubbles. The rapid freezing pushed the bubbles to the centre of the hole. The properties of the hole ice are a major systematic effect for IceCube, as this process is not completely understood yet.

A further feature of the South Pole ice is the azimuthal anisotropy [65]. It has been observed that the photon propagation properties vary with the direction along the z-plane. The origin of this effect is still unclear, although it has been remarked that it would be unlikely to ascribe this effect to the hole ice or the cables since there would be no consistency in the effect, as it is observed.

3.4 Neutrino detection in ice

A neutrino telescope can detect neutrinos of any flavour interacting in its active volume. Interactions have been discussed in 2.3 and this section aims to show how the products

of these interactions are seen and can be detected in IceCube. There are two main different event signatures in ice: tracks and cascades. The first ones are generated when a high energy muon traverses the detector: muons can travel kilometres before decaying or losing enough energy for it not to be detectable anymore. Muons appear, then, as long tracks of light in a water/ice Cherenkov detector. When the primary products of the neutrino interaction cannot travel considerably in the detector, a cascade of particles is generated, with an almost spherically symmetric light emission mainly constituted by a high number of single Cherenkov cones. This section aims at describing the observation of muons neutrino events and the different types of cascades formed in neutrino interactions in ice. In the following we will describe these main topologies.

3.4.1 Tracks

Muons produced in a muon neutrino CC interaction leave kilometres long tracks in ice. The path of a muon in ice is characterised by energy losses of different types, so that muons can be contained entirely in a 1 km^3 detector volume or exit the detector before losing enough energy not to be detectable anymore.

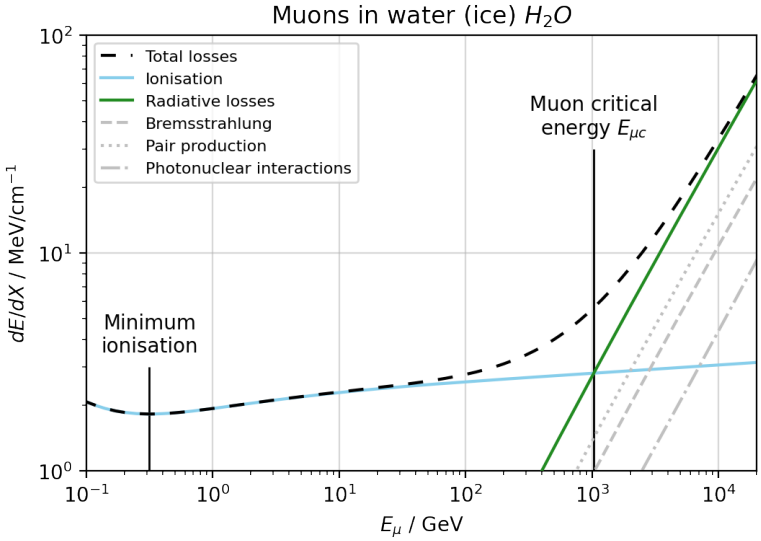

Figure 3.4 – Overview of muon energy losses in ice per length travelled dE/dX as a function of the muon energy E_μ. Values taken from [118].

As it moves through the ice, a muon is subject to losses due to ionisation of the medium via elastic scattering off electrons. For each interaction of this type, the muon loses energy and the mean loss can be described by the Bethe-Bloch formula [118]. Figure 3.4 shows how this effect is only slightly dependent on energy and is dominant below ~ 1 TeV when the muon critical energy is reached and radiative losses take the leading role.

High energy muons can interact with atoms to produce e^+e^- pairs. Electrons and positrons then recombine and form electromagnetic cascades. Pair-production of e^+e^- is the dominant energy loss mechanism above ~ 1 TeV, as can be seen in figure 3.4.

Bremsstrahlung occurs if the muon is suddenly decelerated and emits high energy photons. This process makes the muon lose a considerable part of its energy in a single interaction, while pair-production losses can be treated as if it was a continuous loss [118]. Similarly to pair-production, muons can also interact to produce hadrons. The latter would produce hadronic cascades.

The total energy loss for a muon can be expressed by [118]:

$$-\frac{dE}{dx} = a(E) + b(E)E, \tag{3.5}$$

where $a(E)$ represents the energy losses via ionisation and $b(E)E$ the radiative energy losses. Note that both $a(E)$ and $b(E)$ change very slowly with energy and for the most part they can be assumed constant. The energy dependence of dE/dX above ~ 1 TeV makes it possible to estimate the muon energy using dE/dX as proxy. However, the stochastic losses make this quite challenging. The critical energy can be found as the exact point where ionisation and radiation losses are equal:

$$E_{cr} = a(E_{cr})/b(E_{cr}). \tag{3.6}$$

The range a muon can travel can be expressed, defining the muon starting energy as E_0, in terms of the quantities above [118]:

$$x_0 \approx \frac{1}{b} \ln\left(1 + \frac{E_0}{E_{cr}}\right). \tag{3.7}$$

The mean kinetic angle difference between the primary neutrino and produced muon directions is $0.7°(E_\nu/\text{TeV})^{0.7}$ [104]. A typical muon direction reconstruction resolution in IceCube is $0.6°$ [13].

3.4.2 Cascades

As discussed in 2.3, all neutrino interactions also produce a hadronic shower. Electrons produced in ν_e CC interactions and in the τ particle decay chains generate, instead, an electromagnetic cascade of particles. These two types of showers are not distinguishable in IceCube. Light in showers is generated by the combination of multiple charged particle Cherenkov cones and results in an approximately spherically distributed diffuse light.

Under some circumstances, tau neutrino CC events can produce a double shower: a hadronic shower at the interaction vertex and a hadronic and electromagnetic shower at the τ decay vertex. The resolution of the two cascades is not possible at $\sim$TeV energies, since the τ particle does not travel enough to separate the two vertexes more than the IceCube resolution. The events are seen as two superimposed showers. Recent studies have shown that it is possible to resolve these "double bang" events by the arrival time of the light to the DOMs [137]: if two showers are produced, the number of photons hitting the detector in time should have two peaks, or pulses, corresponding to the times at which the neutrino interaction and the τ decay happen, respectively.

Cascade events are usually well-contained in the detector, therefore the neutrino energy reconstruction for this kind of event is more precise than for track events. The presence of neutral particles, such as neutrons, makes the energy measurement more challenging for hadronic showers.

3.4.3 Principles of reconstruction

Once data are collected and knowing how different particles give different signatures, reconstruction algorithms can be developed and applied to infer the events characteristics. For IceCube the incoming direction and energy of the events are generally the fundamental variables which are analysed. Other important variables for purposes of veto or more peculiar kinds of analyses are the time of arrival and the interaction vertex position coordinates. In this section I will expose the main concepts of angular and energy reconstruction, as these are the observables that are used in this work.

Angular reconstruction

Reconstruction algorithms in IceCube typically involve the use of an unbinned likelihood method. The angular reconstruction likelihood is based on the photon arrival time probability density function (PDF) of the DOMs. Two categories of likelihood are generally used [18]:

$$\mathcal{L} = \prod_{j=1}^{N_{\mathrm{DOM}}} \prod_{i=1}^{N_{\mathrm{hit}}} [p_j(t_i)]^{q_i} \tag{3.8}$$

$$\mathcal{L}_{1st} = \prod_{j=1}^{N_{\mathrm{DOM}}} p_{j,1st}(t_1) \propto [p_j(t_1)]^{q_1} \cdot (1 - P_j(t_1))^{Q_j - q_1}, \tag{3.9}$$

where N_{DOM} and N_{hits} are the total number of hit DOMs and hits, respectively. The PDF for each observed hit is $p(t)$ and $P(t)$ is the cumulative distribution function. Data are weighted by the charge q_i, where $Q = \sum_i q_i$. While the likelihood of equation (3.8) takes into account all the hits, $\mathcal{L}_{1st}$, defined in equation (3.9), only considers the first hit for each DOM. Equation (3.8) is efficient in modelling minimal ionising muons in homogeneous ice. However, muons of typical energy for IceCube are subject to stochastic losses (see 3.4) and the South Pole ice is not homogeneous. Using only the first hit for each DOM reduces the probability of including photons originating in stochastic losses and the error due to the homogeneous ice modelling.

The optimisation is usually conducted on 6 parameters, including the track positional parameters x, y, z, t, and two orientation parameters, the zenith, θ, and azimuth, ϕ, angles. Parameters are summarised by $\mathbf{\Theta} = (x, y, z, t, \theta, \phi)$.

Including ice properties and a more realistic ice model allows for a more accurate reconstruction of the photon arrival distribution. A typical ice model is composed of horizontal layers where ice properties are considered homogeneous. Ice layers have a $10 - 20$ m thickness. The resulting photons from simulated infinite minimally-ionising muon tracks with different positions and orientations are used to build high-dimensional histograms. The photon arrival PDF as a function of the direction and orientation are computed by normalising the histograms and interpolating them with B-splines [143].

Being T the knot positions, the photon PDF can be expressed as:

$$p(t) = \sum_{i=1}^{T-k-1} w_i B_{i,k}(t - t_0; \mathbf{\Theta}, \boldsymbol{\lambda}), \tag{3.10}$$

where $B_{i,k}$ is the i-th B-spline of order k, and $\boldsymbol{\lambda}$ are the parameters that describe the ice properties. The weights w_i are given by the normalisation and sum up to 1. $t_0 = t_0(\mathbf{\Theta})$

indicates the time when the first Cherenkov photon can reach a DOM without scattering for a given emission point hence it depends on the track parameters $\mathbf{\Theta}$.

Further improvements can be obtained by using L_{1st}, by simulating stochastic losses, using better noise modelling, and adding energy information to the PDF [18].

Energy reconstruction

Reconstructing the energy of the products of a neutrino interaction in ice cannot be carried out independently: an estimation of the other event characteristics, $\mathbf{\Theta}$, is needed.

One of the most used reconstruction frameworks in IceCube is called *Millipede* [105]. The main feature of this framework is the separation of the event in several time bins $\tau = 1, ..., T_i$ defined for each DOM i. The Millipede likelihood is a Poissonian likelihood comparing the distribution of observed photons $N_{i\tau}$ with the distribution of the expected photons $\mu_{i\tau}$. It can be expressed in terms of its logarithm as:

$$\log \mathcal{L}_{\mathrm{mp}} = -\sum_{i=1}^{N_{\mathrm{DOM}}} \sum_{\tau=1}^{T_i} \left[N_{i\tau} \log(\mu_{i\tau}) - \mu_{i\tau} + \log(\Gamma(N_{i\tau}+1)) \right]. \tag{3.11}$$

The expected photon distribution $\mu_{i\tau} = \sum_{k=1}^{K} \mu_{i\tau k}(\mathbf{\Theta}_k; E_k)$, in terms of K discrete energy losses E_k, is obtained in a similar way as for the angular reconstruction: photons from tracks of different positions and orientation are simulated and photon arrival PDFs are arranged in splined tables. Millipede features an internal optimisation of the energy losses. In the first layer, the likelihood minimisation is carried on the $\mathbf{\Theta}$ parameters and, at each step, in a second layer, the energy losses are optimised. The result is the likelihood minimised value and a number k of energy parameters.

The *PegLeg* reconstruction aims at testing the hypothesis of a finite minimally-ionising track and a starting cascade at the same interaction vertex and aligned with the track [105]. The hypothesis is then composed of the set of parameters $\{\mathbf{\Theta}, L, E_c\}$, where L is the length of the track and E_c the cascade energy. The energy of the track, in the minimally-ionising hypothesis, can be directly inferred from its length. The energy loss is set to $0.22\ \mathrm{GeV/m} \cdot L$ and the track is split into 5 m segments. The likelihood used is the Millipede one and the optimisation is, in a similar fashion, composed of three layers optimising, in turn, different parameters.

The first layer consists of optimisation on $\mathbf{\Theta}$ where L and E_c are found internally and returned as values together with the likelihood value.

In the second layer, the $\mathbf{\Theta}$ parameters are fixed at the values found in the first layer and the new optimisation consists of a scan of the L phase space. For each step of the optimisation, a track segment is added as far as the likelihood keeps improving, starting from the first segment, where the cascade energy E_c only is present. E_c is, again, obtained internally.

The last layer is the optimisation of the cascade energy E_c, while fixing all the other parameters at the optimal values found in the previous layers. The likelihood is derived with respect to E_c:

$$\frac{d \log \mathcal{L}_{\mathrm{mp}}}{dE_C} = \frac{1}{E_c + c_1} + c_2 = 0, \tag{3.12}$$

where, being the c_i constants, the optimisation aims to find the one positive value of E_c that satisfies equation (3.12). The optimum value is found with the Newton method [87] via the second derivative of the log-likelihood $\log \mathcal{L}_{\mathrm{mp}}$.

As explained in paragraph 3.4.3, an improvement is seen using a process of photon selection similar to what is done in L_{1st}. In this case, for each time bin τ, only the first photon is selected, ignoring all subsequent hits in a certain "dead" time window. The difference with what is described for L_{1st} is that a new time window is opened at the end of the first, and a new, late photon can be included, repeating the same process as for the first time window.

3.5 IceCube highlights

In the last decade, IceCube has produced many important results, pioneering the fields of neutrino and multi-messenger astronomy. The impact of these discoveries has been decisive in rising the interest towards this new field and paving the way to new projects and experiments [26] [34] [33]. This section summarises the most prominent results achieved by the IceCube collaboration.

3.5.1 The astrophysical neutrino flux

IceCube published in 2013 a paper [1] showing the first evidence for an astrophysical component in the measured neutrino flux in the Tev-PeV energy region. The observation was made out of a selection of well-contained High Energy Starting Events (HESE) in the detector with two-years data combining the 2010-2011 season, with the 79 strings configuration (IC79), and the 2011-2012 first full configuration (IC86) season. Subsequent analyses with various selections of data, including a multi-year HESE selection [17], confirmed the first evidence and attempted to characterise the incoming flux of neutrinos of astrophysical origin. Figure 3.5 shows the flux of neutrinos in IceCube with the HESE selection.

A comparison of the fit for the normalisation and spectral index of the flux characteristics when assuming a single power-law flux with different selections of data shows, at present, a mild tension between the results of the different analyses. This tension could be due to different energy responses between the analyses or different physics happening at different energies and is currently object of study. The tension is illustrated in figure 3.6.

3.5.2 Oscillation studies

IceCube is also competitive in the neutrino oscillation field. The parameters Δm^2_{32} and $\sin^2(\theta_{23})$ have been constrained measuring muon-neutrino disappearance [14] for atmospheric neutrinos hitting the detector after crossing the Earth. Muon neutrino disappearance is the effect for which the expected flux of muon neutrinos lacks of events, with the maximum effect visible around 25 GeV. The missing events are muon neutrinos that, while crossing the Earth, have oscillated into another flavour. The results of this analysis are in agreement with other long-baseline oscillation analyses and are shown in fig. 3.7.

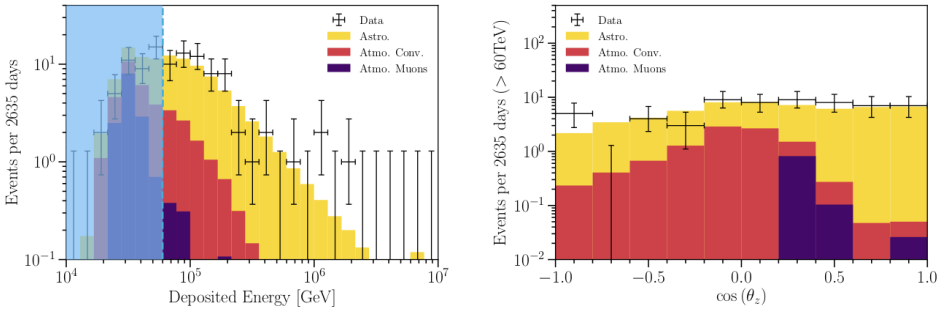

Figure 3.5 – Graphical representation of the flux best fit values for the IceCube HESE selection. Data are the black crosses. Astrophysical neutrinos are in gold, while atmospheric neutrinos are in red and atmospheric muons in purple. From [17].Left: Energy spectrum. Right: Declination distribution. Up-going events are closer to $\cos(\theta_z) = -1$ *and down-going events are closer to* $\cos(\theta_z) = 1$.

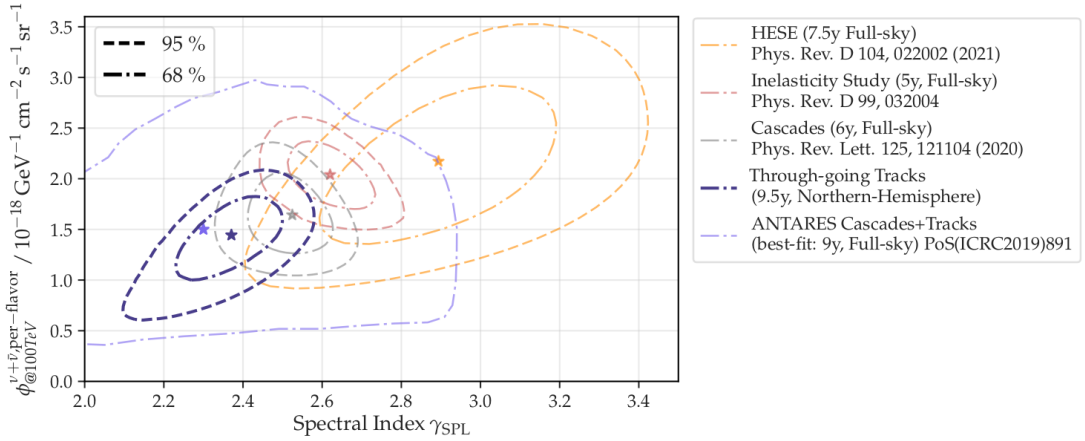

Figure 3.6 – Flux single-power law normalization (y-axis), versus spectral index (x-axis) for different analyses. Adapted from [19].

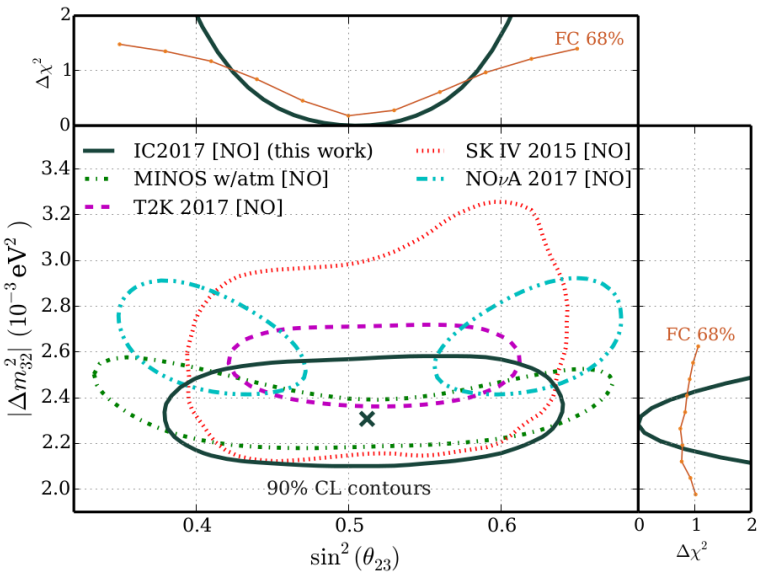

Figure 3.7 – IceCube oscillation results compared to other long-baseline oscillation experiments. From [14].

3.5.3 Astrophysical neutrino sources

In 2017 IceCube detected the high energy event IceCube-170922A. The real-time alert system made it possible to point gamma-ray telescopes in the incoming neutrino direction to find the known blazar TXS 0506+056 in a flaring state [5]. A subsequent search for neutrinos from the direction of TXS 0506+056 in the IceCube archival [6] data found an excess of neutrinos over the expected atmospheric background in the 2014-2015 period. Further evidence for a neutrino source was found in the IceCube all-sky search for the source NGC 1068 [10]. These results give the first and, currently, the strongest evidence for astrophysical neutrino sources. It is important to underline how the multi-messenger approach to astronomy was decisive to have the capability to determine an evidence with just one neutrino event. The discovery of neutrino sources is fundamental to determine the environments where cosmic-rays are accelerated to extreme energies.

3.5.4 A Glashow resonance candidate

A Glashow resonance is a process for which the cross-section of an electron anti-neutrino interaction with an electron is enhanced for an anti-neutrino energy of $E_\nu = 6.3$ PeV. The resonant interaction forms a W^- boson. In ice, the W^- decays to produce a hadronic shower, which is detectable via Cherenkov radiation observation. Recently, IceCube presented a study on one event consistent with a Glashow resonance event [8]. The event has been claimed as of astrophysical origin at 5σ level. The reconstructed visible energy is 6.05 ± 0.72PeV which, considering the non-detectable components of a hadronic shower, is consistent with the tested hypothesis. The analysis carried in [8] computed a 2.3σ rejection of the hypothesis for the event to be of different origin than

the Glashow resonance. The detection of muons during the event is also consistent with the hadronic production in a W^- decay.

3.6 Previous dark matter results

IceCube has played an important role in the search for dark matter since its beginning. Observation of neutrino fluxes can give evidence for the presence of dark matter in particular regions from which dark matter is expected. Typical regions are the centre of the Galaxy, dwarf galaxies, galaxy clusters and local sources such as the Sun and the Earth (see 1.4 and 1.5.4). IceCube sensitivity to variations of the expected fluxes caused by dark matter has grown in time, due to novel analysis techniques and the accumulation of data seasons. This section aims at reviewing IceCube potentialities and main results in this field.

3.6.1 Dark matter from the centre of the Galaxy

The centre of the Galaxy is one of the most promising sites to search for dark matter, due to gravitational evidence (see 1.4.2) of a matter overdensity. A 3-years analysis searching for dark matter annihilation has been published in 2017 [4] and the results of this analysis have been used in an IceCube-ANTARES combined effort [41]. A search for decaying dark matter has been conducted [7] with two different selections of tracks and cascades, respectively. These analyses investigated a possible improvement in the IceCube neutrino flux description by adding a dark matter decay component. The latter was able to set the current best limits on a wide dark matter particle mass range in indirect searches, as shown in figure 3.8.

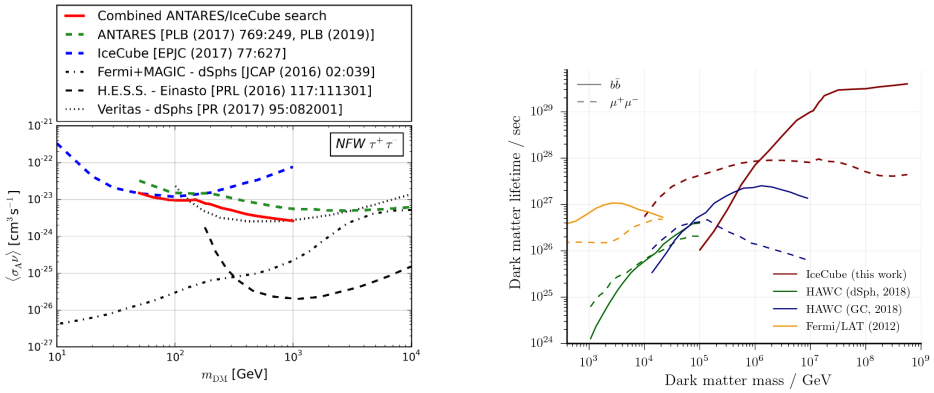

Figure 3.8 – Left: Limits from the combined ANTARES-IceCube analysis. From [41]. Right: Limits for dark matter decay from the galactic centre. From [7].

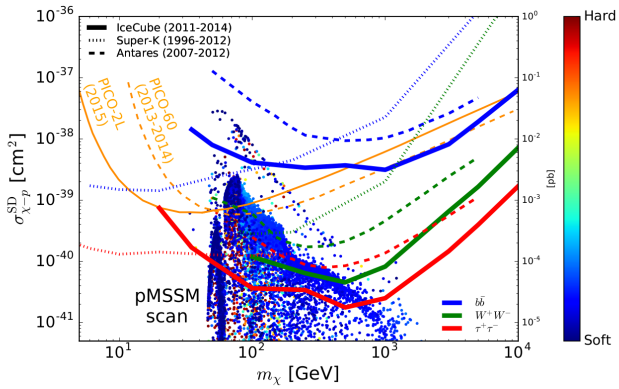

Figure 3.9 – IceCube limits on the spin-dependent WIMP-nucleon cross-section. From [3].

3.6.2 Dark matter from the Sun

The model which brings to accumulation and self-annihilation of dark matter in the centre of the Sun has been explained in 1.5.4. As written before, because of the higher gravitational effect of the Sun, the process described by equation (1.31) has reached equilibrium, therefore, for the Sun, equation (1.42) can be applied.
A search [3] has been performed with 3 years of IceCube data. The search focused on track-like events, with a selection of only up-going events during the Austral winter, when the Sun is under the horizon, to strongly reduce the atmospheric muon background. The centre of the Sun could be treated as a point-like source and an unbinned likelihood method was used. The spin-dependent dark matter-nucleon scattering is the favoured process for the Sun, as stated in 1.5. Results from this analysis are shown in figure 3.9. A renovated effort in this field is in place and new results are foreseen.

3.6.3 Dark matter from the centre of the Earth

An early investigation on dark matter from the centre of the Earth was completed with 1 year of data [12]. A dedicated event selection was developed and the final zenith distribution was analysed with a likelihood method. This analysis has been a pathfinder for the analysis object of this dissertation. Results are shown in figure 3.10.

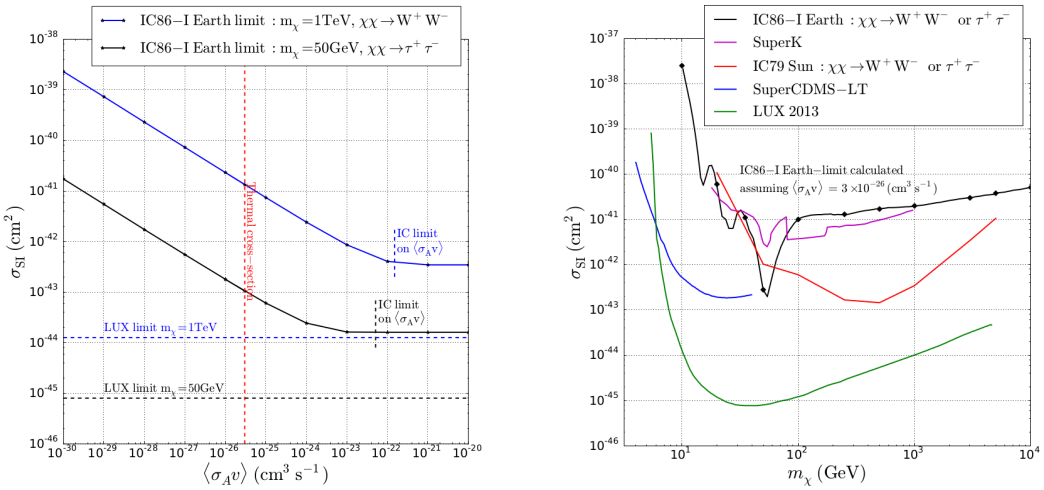

Figure 3.10 – Limits from the 1 year search for dark matter in the centre of the Earth. From [12]. Left: Cross-dependency plot of the self-annihilation cross-section $\langle\sigma_A v\rangle$ and the spin-independent DM-nucleon scattering cross-section $\sigma^{SI}_{\chi N}$. Right: Limits on $\sigma^{SI}_{\chi N}$, given the assumption $\langle\sigma_A v\rangle = 3\times10^{-26}\mathrm{cm}^3\mathrm{s}^{-1}$.

CHAPTER 4
THE EVENT SELECTION

And it's whispered that soon, if we all call the tune
Then the piper will lead us to reason

In this chapter, the process I implemented to select the possible interesting events for a search for a dark matter signal from the centre of the Earth is presented. We expect a small signal for this analysis, in the order of tens of events, based on the limits from the previous 1-year analysis [12]. Therefore, we need to reduce the background as much as possible. The main goal of the event selection is to discard the highest possible number of muon events. Neutrino events from other sources are very similar to those coming from dark matter annihilation in the centre of the Earth. Neutrinos will, hence, constitute the main source of background at the latest stages of the selection. After illustrating the characteristics of signal and background (4.1), I will disclose the selection process I developed for this analysis. The first sets of cuts (presented in 4.2 and 4.3) are thought to reduce the amount of data, in order to run a random forest algorithm (4.4.2) within a reasonable computational time. The random forest is the main stage of the selection, as it is a powerful tool to discriminate muon events from neutrino events. The selection, at this point, is split into a low-energy (LE) and a high-energy (HE) part (4.4), as the lower and higher energy signal events present differences which complicate the possibility to find a general common pattern in the event characteristics. A reconstruction algorithm able to reliably reconstruct the energy of the events is run as the final step. The computational demand of this step is the reason why it is applied only at the latest stages of the process. The final reconstruction algorithm and the last stages are presented in 4.5.

4.1 Signal and background characteristics

In this work, a signal-like event comes from a direction close to the centre of the Earth ($\theta \sim 180^\circ = \pi/\mathrm{rad}$). These events are seen from IceCube as *up-going*, i.e. they come

from directions below the surface. The analysis focuses on muon-neutrino signal events because of their better angular resolution (see 3.4).

Muons generated in interactions of ultra-high-energy cosmic rays (UHECR) in the atmosphere can only come from above the surface (they are *down-going*), but a fraction of them is mis-reconstructed as up-going by the reconstruction algorithms. These mis-reconstructed *atmospheric muons* are an artificial up-going background that, at a low selection level, largely dominates the composition of the events.

Neutrinos are also generated in atmospheric UHECR interactions. Neutrinos, in the energy range 1 Gev - 10 TeV, can travel through the entire Earth to reach IceCube from the opposite side. When their direction is close to that of the centre of the planet, this kind of event has very similar characteristics to signal events. These neutrinos constitute the main background at the final selection level.

4.1.1 Datasets

Generally, in analyses involving experimental data, it is preferable to work with pseudo-data while developing the process. The reason is that working with real data could create biases that can lead to wrong interpretations of what is seen or desirable, fine-tuned outcomes. With this method, the analysers are able to work *blind* to the real data. Only when an analysis is completely set, a process of *unblinding* reveals the real data-driven results.
In many analyses, to preserve blindness during the analysis development, the background can be estimated by scrambling the right ascension coordinates of real data events. This technique can be used since the IceCube atmospheric background is uniform in right ascension. A potential signal would be diluted by the scrambling. However, the peculiar direction investigated in this work does not allow for this kind of estimation: the zenith angle $\theta = 180^\circ$ is one of the poles of the spherical coordinates system so, for events near the pole, a scrambling in right-ascension would not move the events far from their original position, preventing the signal from being diluted. Consequently, we need to rely on Monte Carlo (MC) simulations. A burn sample of real data is used to check the reliability of simulations in representing reality. Simulations are used to test the efficiency of the selection steps all along the process.

Background IceCube provides collaboration-wide usable simulations, including generation, propagation to the detector, and interaction in ice simulation. *Atmospheric muons* are generated with CORSIKA [94]. CORSIKA generates full cosmic ray interaction simulations. The IceCube collaboration produces events in the primary cosmic ray energy range 600 GeV $< E_{\mathrm{CR}} < 10^{11}$GeV.
Neutrinos are generated with the GENIE and NuGen software pieces, for energy $E_\nu < 100$ GeV and $E_\nu > 100$ GeV, respectively. GENIE [44] and NuGen (which is an adapted version of ANIS [86] for IceCube) produce event simulations for neutrinos interacting in the detector volume. The interaction is forced in order not to reduce statistics after the generation and a weight is given for the probability of the interaction to happen. These events can then be weighted to reproduce the desired flux. As explained before, we expect a primary contribution from atmospheric neutrinos, for which the event weights are produced using the *Honda* model [97] [96]. Neutrinos generated in UHECRs interactions with heavier quarks (*prompt* neutrinos) and astrophysical neutrinos are included, too, even if their contribution is expected to be very low compared to

Component	Flux
Classic Atmospheric	Honda 2006 [97] and 2014 [96]
Prompt Atmospheric	Sarcevic Standard [77]
Astrophysical	$\Phi_\nu = nE^\gamma$ with $n = 1.44$, $\gamma = 2.28$ [19]

Table 4.1 – Summary of neutrino flux schemes used for this work.

Parameter	Value
θ_{12}	33.65^o
θ_{13}	8.33^o
θ_{23}	45.57^o
δ_{CP}	0
Δm^2_{21}	$7.53 \cdot 10^{-5}$ cm^2
Δm^2_{31}	$2.45 \cdot 10^{-3}$ cm^2

Table 4.2 – Neutrino oscillation parameters set used in simulations.

the classic atmospheric contribution, as from the reference fluxes by Sarcevic [77] and the 9.5 years through-going tracks IceCube analysis [19] for the prompt and astrophysical neutrinos, respectively. The choice of using the result in [19] for the astrophysical flux comes from the fact that the data selection used for that analysis is the most similar to the selection developed for this work for energy range and incoming direction distribution. Table 4.1 resumes the different weighting schemes applied to the simulated neutrinos. As the main neutrino background is up-going, neutrino oscillation must be considered. Oscillation is included for travelling through the Earth with the parameters shown in table 4.2.

Signal Dedicated signal simulations were produced specifically for this analysis using WimpSim [57] [76]. Events propagation and interaction in the detector were simulated with IceCube-provided tools, similarly to the simulations presented above for background. Simulations for the three channels $\chi\chi \to \tau^+\tau^-$, $\chi\chi \to W^+W^-$ and $\chi\chi \to b\bar{b}$ are produced, considering each time 100% branching ratio. A range of dark matter masses from 10 GeV to 10 TeV is considered. Table 4.3 shows the details of the DM scenarios produced. Since we expect different behaviour between low-energy (LE) and high-energy (HE) events and we want to be sure our selection is efficient in a wide range of energies, two signal configurations are chosen as baseline for LE and HE, respectively:

- LE: $\chi\chi \to \tau^+\tau^-$, $m_\chi = 50$ GeV;

Channel	Masses
$\chi\chi \to \tau^+\tau^-$	[10, 20, 35, 50] GeV
	[100, 250, 500] GeV
	[1, 3, 5, 10] TeV
$\chi\chi \to W^+W^-$	[100, 250, 500] GeV
	[1, 3, 5, 10] TeV
$\chi\chi \to b\bar{b}$	[35, 50] GeV
	[100, 250, 500] GeV
	[1, 3, 5, 10] TeV

Table 4.3 – Summary of WIMPs simulation scenarios produced with WimpSim.

- HE: $\chi\chi \to W^+W^-$, $m_\chi = 1$ TeV.

The parameters in table 4.2 are used for oscillation in travelling through the Earth from the centre to the surface.

Data The analysed IceCube data consist of 10 years of events from the 2011 to the 2020 season for a total of $\sim$ 3619 days. Each day of data-taking is separated in three runs identified with sequential numbers. A burn sample of $\sim$ 353 days of IceCube data is used for data/MC agreement verification along the event selection steps. The burn sample corresponds to $\sim 10\%$ of the total available data and the runs composing the burn sample are taken sparsely over the whole livetime, selecting the runs whose identification number ends with 0.

4.2 First set of cuts

This section describes the first steps I took in the selection process for this work. In these stages, I aim at reducing the overall rates to run more sophisticated reconstruction algorithms by removing the events which are more obviously background. At this point, cuts are quite conservative since the quality of the reconstructed event characteristics available is not high.

4.2.1 Combination of filters

As a very first step, the possible interesting selections available in IceCube after the online filtering (see 3.2.4) are selected. The four filters called *MuonFilter*, *DeepCoreFilter*, *LowUpFilter* and *VEF* are tried in different combinations to choose the solution which

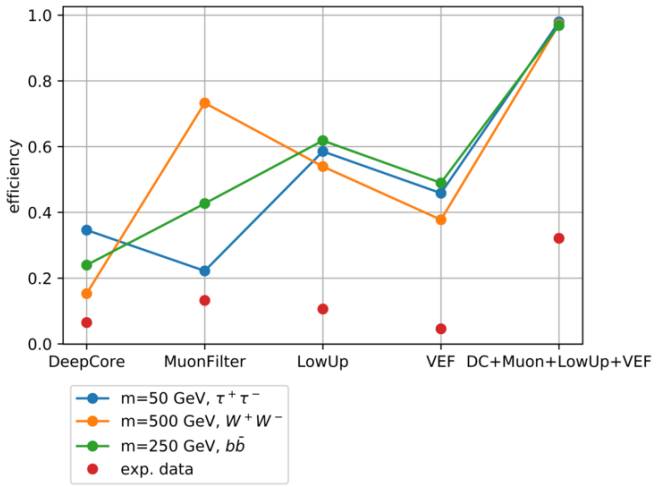

Figure 4.1 – Efficiency for different combinations of the four selected filters: MuonFilter, DeepCoreFilter, LowUpFilter and VEF. Efficiency is tested on three different signal signatures (blue, yellow and green lines). Experimental data from the burn sample (red dots) are included to show the efficiency in removing background events.

saves the most of the signal. Efficiency is defined as the ratio between the number of events passing the filters $N_{\text{ev,selection}}$ and the total number of events at L2 $N_{\text{ev,L2}}$:

$$\epsilon = \frac{N_{\text{ev,selection}}}{N_{\text{ev,L2}}}. \tag{4.1}$$

It is found that the combination of all four filters is the best possible solution from the point of view just described, as shown in figure 4.1. Events passing more than one filter are taken once, following the logic:

MuonFilter `or` DeepCoreFilter `or` LowUpFilter `or` VEF.

4.2.2 Zenith and quality cuts

A straightforward step that can be applied is a cut on the reconstructed zenith angle distribution. As previously explained, it is preferable to be conservative in this early phase, so a cut $\theta_{\text{reco}} > 115°$ is applied to reduce most of the down-going events. Reconstruction algorithms compute a goodness-of-fit variable indicating the probability of the reconstruction to be a good representation of the sequence of hits detected. Lower values indicate a likely successful reconstruction. A cut on this variable is applied to reduce the rate of possibly mis-reconstructed events: $r \log L < 15$. The two variables θ and $r \log L$ are shown in figure 4.2.

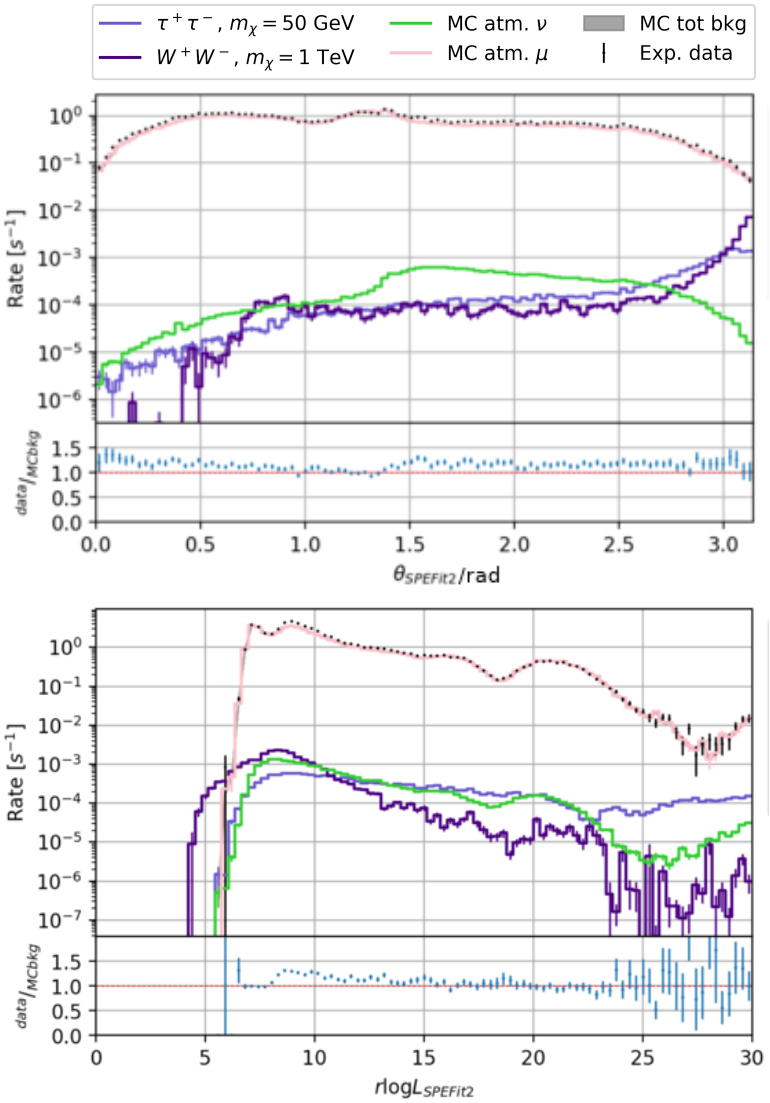

Figure 4.2 – Variables before the cuts presented in 4.2.2. Top: Reconstructed zenith distribution. Bottom: Goodness of fit variable $r \log L$.

4.2.3 Veto cuts

As the last step for this first analysis stage, I cut out events having the reconstructed interaction vertex outside the detector or at the top of the detector volume. The idea here is to discard events which are not entirely in the detector. The reason to avoid these events is the high probability of a low-quality reconstruction due to only partial detection. The cut is applied on the variables ρ_{reco} and z_{reco}, being, respectively, the distance from the vertical axis of the detector and the vertical distance from the centre of the detector.
The variable z_{travel} [103] is defined as:

$$z_{\text{travel}} = \sum_{i=1}^{N} \frac{z_i - \langle z_{\text{1stQuartile}} \rangle}{N}, \tag{4.2}$$

which is the average of the distances between the N hit DOMs and the average position of the hit DOMs in the first quartile along the z-axis. This variable represents the drift along the z-axis for an event. Negative values of this variable generally correspond to down-going events, while positive values denote most probably up-going events. The distribution of the three variables just presented is shown in figure 4.3.

A loop is run on the possible cut values combinations of the three variables, in order to find the best possible efficiency, which, for this step, is defined as:

$$\epsilon = \frac{\epsilon_{sig}}{\sqrt{\epsilon_{bkg}}}, \tag{4.3}$$

where ϵ_{sig} is the combined efficiency for baseline low dark matter mass and high dark matter signal, and ϵ_{bkg} is the background passing ratio. Figure 4.4 illustrates the scan performed on the cut values and marks the most efficient combination at:

- $\rho_{\text{reco}} < 520$ m;
- $z_{\text{reco}} < 60$ m;
- $z_{\text{travel}} > 20$.

4.3 Re-running reconstruction algorithms

At this stage, the selection starts to differ more substantially from the previous work [103]. In the first instance, casual hits activating a detector response contemporarily to the events are removed. Also, a more sophisticated algorithm can recognise when two events are happening coincidently and separate them. The cuts used in the previous step (see 4.2) are applied again and some new cuts are added. At this point, the aim is to further reduce the overall rate and start to discriminate atmospheric muons more aggressively. The final target is to prepare data for the machine learning algorithm that will constitute the following step, described in 4.4.

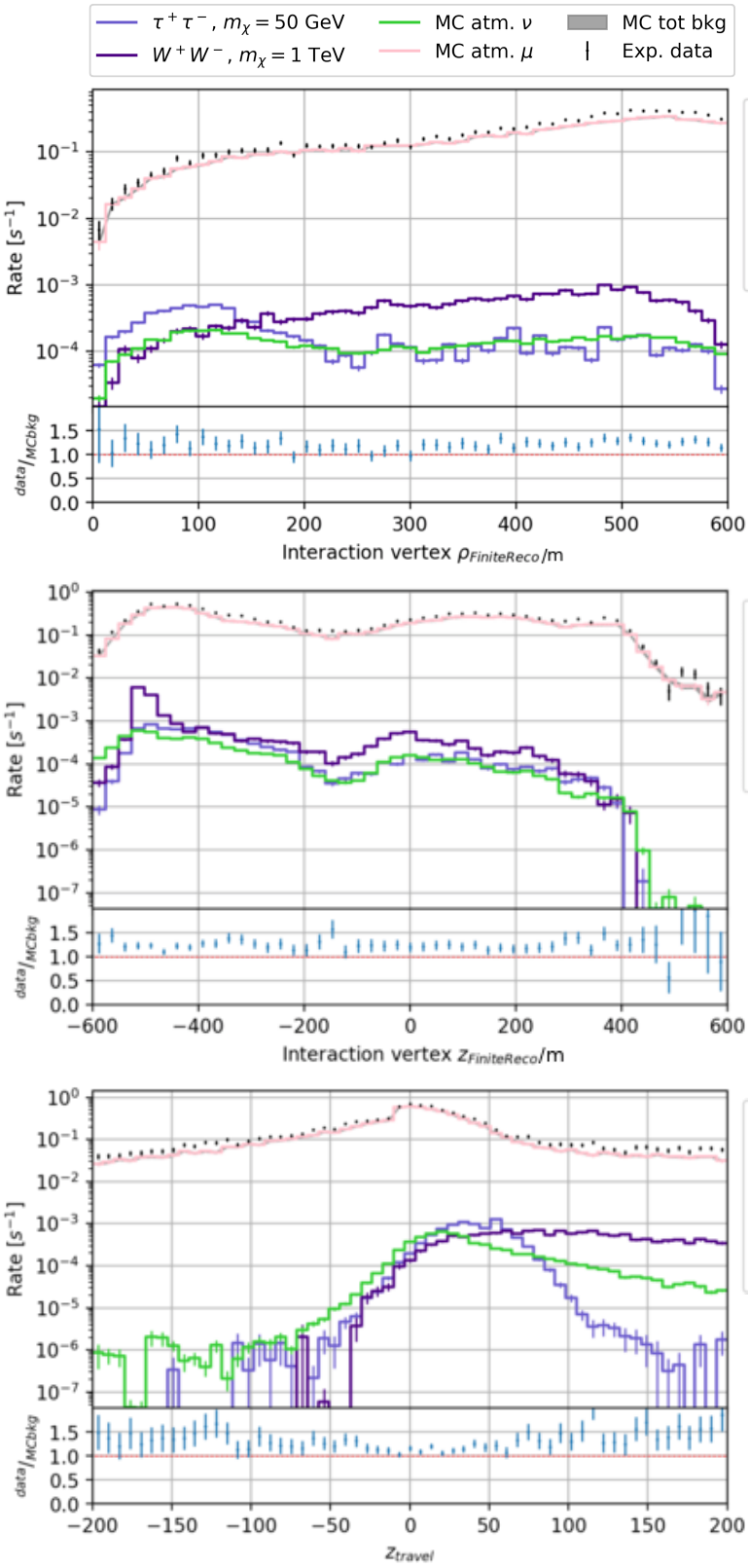

Figure 4.3 – Distribution of variables before the cuts in 4.2.3. Top: Reconstructed interaction vertex ρ coordinate distribution. Middle: Reconstructed interaction vertex z coordinate distribution. Bottom: z_{travel} distribution.

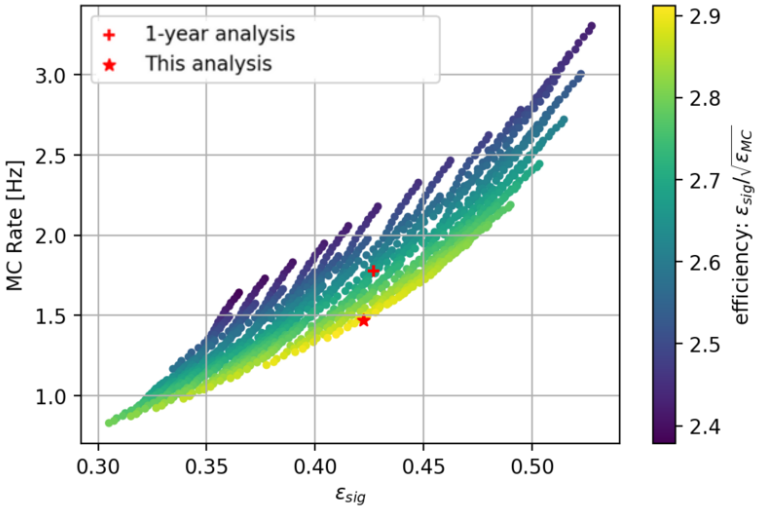

Figure 4.4 – Plot of the efficiency (see (4.3)*) for the combination of cuts on the three variables* ρ_{reco}*,* z_{reco} *and* z_{travel}*. The* x*-axis is the signal efficiency, while the* y*-axis represents the background rate. The colour scale indicates the efficiency value. The plot also shows the combination used in [103] (marked as "1-year analysis"). The optimum combination of cuts is given by the colour scale, with yellow indicating the maximum value of the defined efficiency* $\epsilon_{\mathrm{sig}}/\sqrt{\epsilon_{\mathrm{bkg}}}$*.*

4.3.1 Cleaning and splitting

As summarised in the introduction to this section, the first step of this selection level is the cleaning of the hits [103]. Each hit is given an individual active volume. In this way, isolated hits can be excluded from the reconstruction algorithms. Categorisation of the hits is also used to separate coincident events into two single events. A coincident event is generally an atmospheric muon that hits the detector in the same time window of an interesting event. In these cases, reconstruction is harder since hits from the coincident event can be included while attempting to reconstruct the main event, altering the correct sequence of hits needed for a successful reconstruction. This is particularly important since $\sim 10\%$ of the IceCube events are coincident. Hits can be considered as connected when:

- they are part of the same Cherenkov cone: they are spatially separated but have little or null time separation;
- they are part of the same light front: they have the same photon propagation speed;
- they are part of the same track: they are connected via the particle propagation speed.

Cleaned series of hits are used to run the relevant reconstruction algorithms again. The advantage is that removing casual hits and splitting coincident events allow for

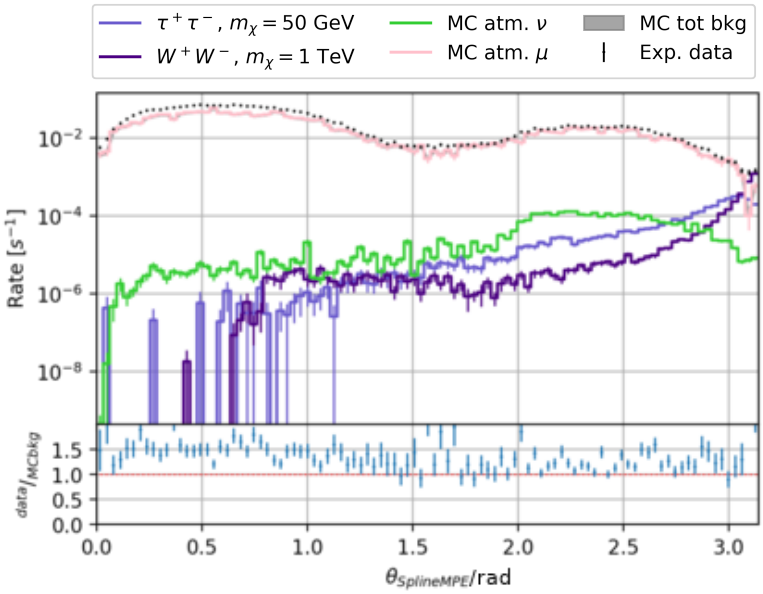

Figure 4.5 – Reconstructed zenith distribution after the cleaning and re-running process described in 4.3.1. Note that the processing made it possible to recognise as down-going more than half of the total previously mis-reconstructed atmospheric muons.

more precise reconstructions and more reliable results. The *SplineMPE* algorithm described in 3.10 is run at this stage. Figures from 4.5 to 4.9 show the distribution of cuts variables after cleaning and re-running. These variables are used to apply the same cuts as in the previous stages.

4.3.2 Added variables

A set of variables, firstly introduced for the previous search with 1 year of IceCube data [103], is computed. These variables are relevant in discriminating down- and up-going events and removing noise hits that could still be present.

The first variable is the speed ratio defined using the first three HLC hits of an event. The variable is defined as:

$$\frac{v_{12}}{v_{13}} = \frac{d_{12}/\Delta t_{12}}{d_{13}/\Delta t_{13}}, \tag{4.4}$$

where indexes 1,2,3 indicate the first, second, and third hit, respectively. d_{ij} and Δt_{ij} are the distance and the time difference between the i-th and j-th hit, respectively. The projection on the z-axis of this variable is particularly useful in identifying up-going events. Analogous variables v_{12}/v_{23} and v_{13}/v_{23} are computed.

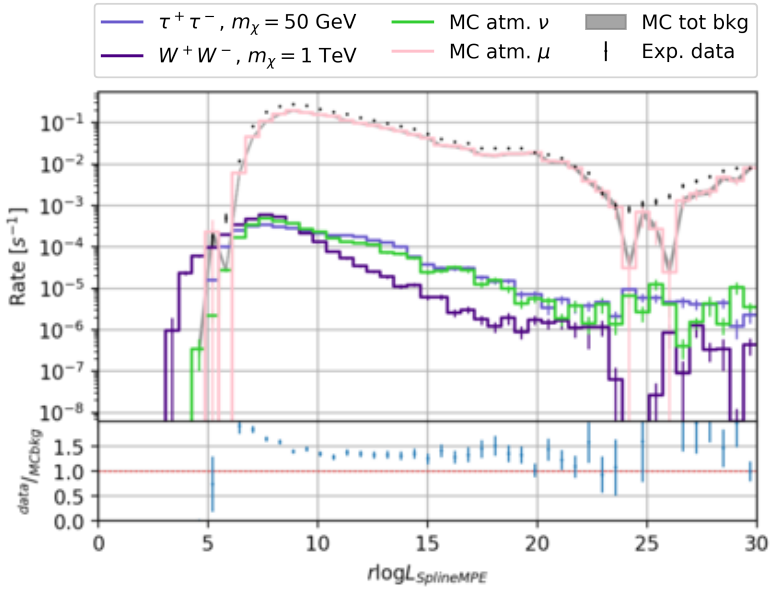

Figure 4.6 – Quality variable $r \log L$ distribution after cleaning and re-running, as described in 4.3.1.

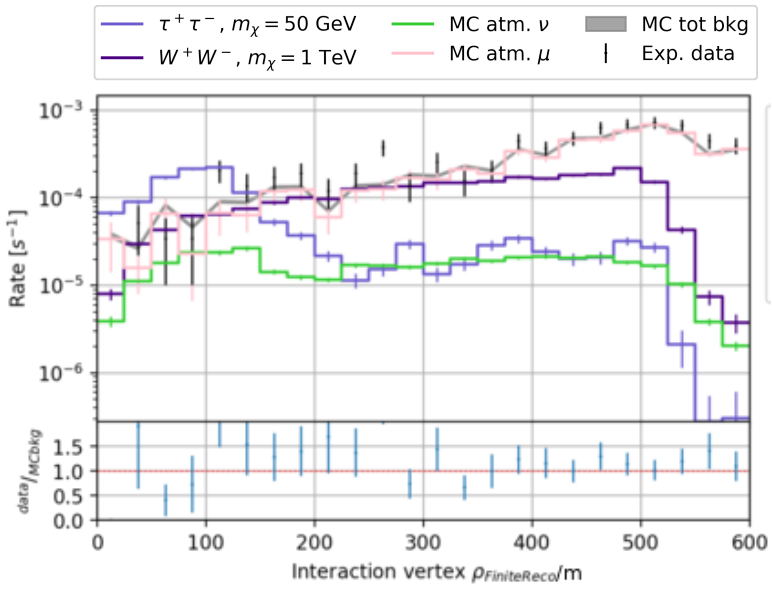

Figure 4.7 – Interaction vertex distance from the detector axis distribution after cleaning and re-running, as described in 4.3.1.

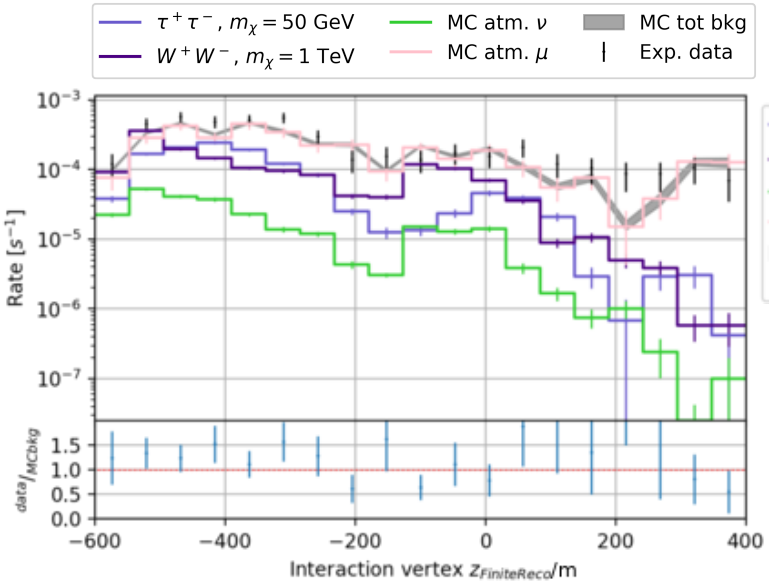

Figure 4.8 – Interaction vertex vertical distance from the detector centre distribution after cleaning and re-running, as described in 4.3.1.

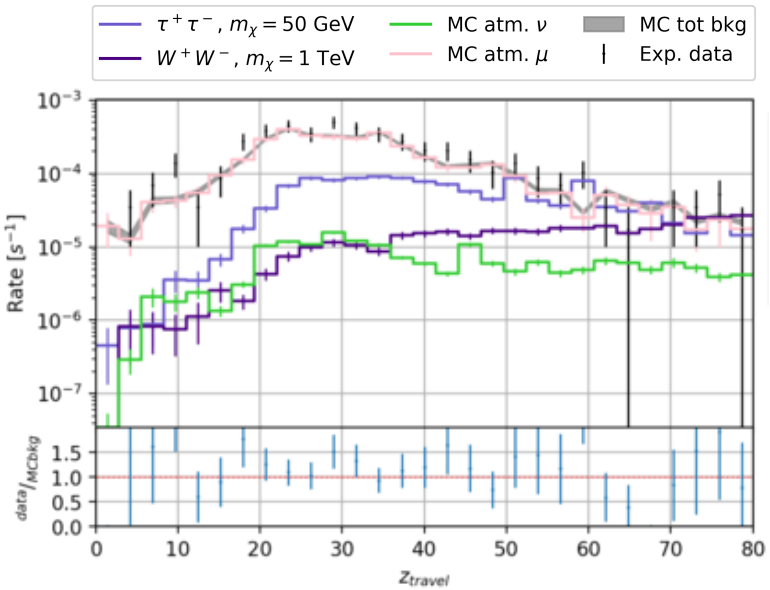

Figure 4.9 – z_{travel} distribution after cleaning and re-running, as described in 4.3.1.

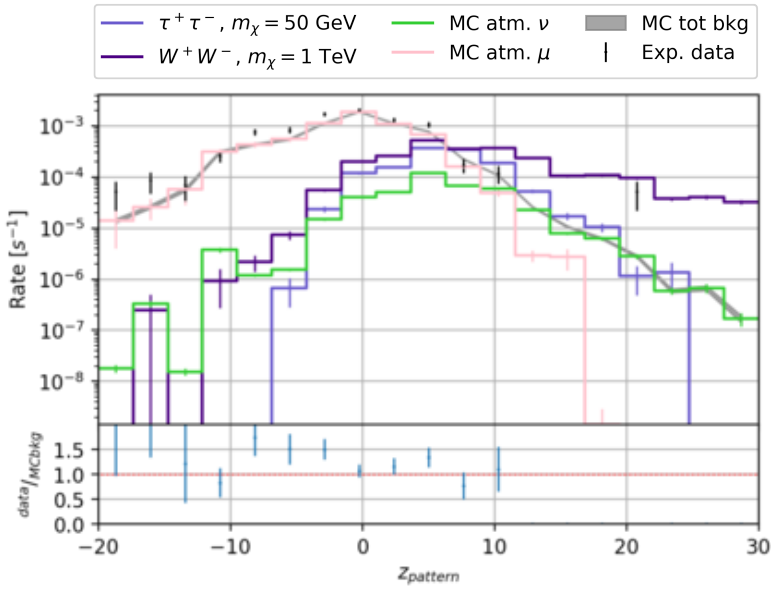

Figure 4.10 – Distribution of the variable z_{pattern} introduced in 4.3.2.

The second variable is the sum of the sign of the vertical distances between each couple of consecutive hits. This variable, called z_{pattern}, can be expressed in the following form:

$$z_{\text{pattern}} = \sum_i \text{sign}(\Delta z_i), \tag{4.5}$$

with i being the couple of hits considered. Positive values identify up-going events, as shown in figure 4.10.

4.3.3 Cuts

After the reconstructions, as mentioned in 4.3.1, cuts are applied to the events. Now that cleaner sets of hits can be used and higher quality reconstructions have been computed, more stringent cuts are applied to the zenith angle θ_{reco} and the quality parameter $r \log L$:

- $\theta_{\text{reco}} > 149°$;
- $r \log L < 9$.

Cuts on variables ρ_{reco}, z_{reco} and z_{travel} are left unaltered (see 4.2) and re-applied. I added a further cut on the variable z_{pattern} with the condition $z_{\text{pattern}} > -1$. The final reconstructed zenith angle distribution is shown in figure 4.11.

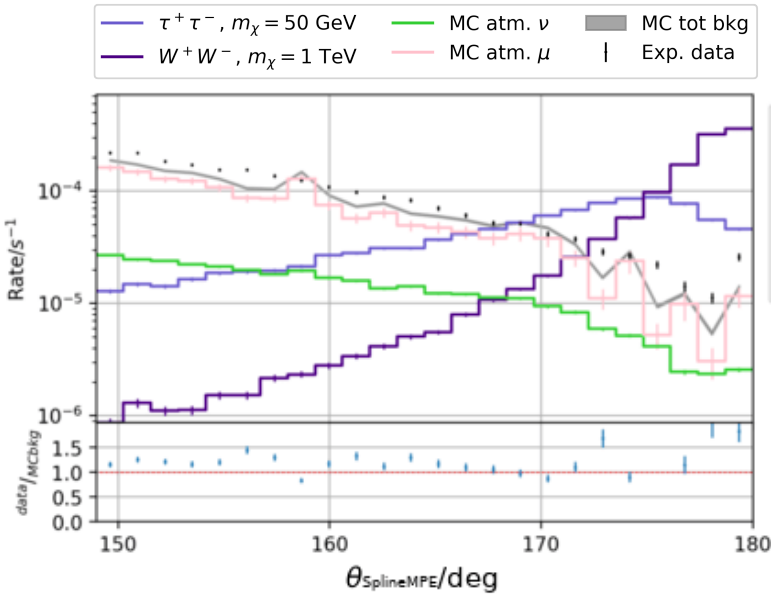

Figure 4.11 – Zenith angle distribution after the whole process described in 4.3.

4.4 Analysis splitting

At this selection level, as the background is still dominated by mis-reconstructed atmospheric muons by orders of magnitude, a more sophisticated method is needed to discard them efficiently while saving most of the signal. Now that the data rate is reduced enough to allow for a stronger computational effort, a random forest machine learning algorithm is applied. A random forest is composed of multiple *decision trees* which have *branches* where events are separated according to their characteristics. At this point the signal originating from low-mass ($m_\chi \lesssim 100$ GeV) and high-mass ($m_\chi \gtrsim 1$ TeV) dark matter annihilation have different characteristics that bring to different distributions in many variables. For example, high energy events have better angular resolution and are more focused in the $\theta \sim 180°$ region, while low energy events tend to lie in a smaller volume, often inside DeepCore and have worse angular resolution due to the lower number of photons that can be detected. For this reason, the selection is split into two: for the first selection, I focus on low-energy signal signatures (LE selection) while for the second on high-energy ones (HE selection).

4.4.1 Decision trees

A decision tree is made of subsequent splitting nodes and for this case, the physical variables describing the events are the parameters used in the trees. The chosen variables are those which have the best chance at discriminating background from signal. At each node, a cut on one parameter is applied, so that events are divided depending on whether they do, or do not, pass the cut. Split nodes are those branching out into more nodes. A node which does not have more subsequent nodes is called a leaf node and can be either a signal or a background leaf. An event walks its path through the

nodes until reaching a leaf. The signal purity p, defined as the fraction of signal events on the total in a leaf, indicates whether a leaf is a signal or a background leaf. A signal purity $p > 1/2$ identifies a signal leaf. For each node, the Gini separation criterion is defined as:

$$S_G(p) = p(1-p). \tag{4.6}$$

At each split, being L and R the left and right node respectively, a separation gain factor can be written as:

$$\Delta S = S_G(p) - W_L S_G(p_L) - W_R S_G(p_R), \tag{4.7}$$

where W_L and W_R are the total weight in the left and right nodes, respectively. The algorithm puts cuts in place maximising the separation gain ΔS.

Trees need to be trained to find the cut values for the parameters at each node and determine whether a leaf is a signal or a background one. Sub-samples of the datasets are used as training samples. More sub-samples are used as testing samples to validate the training by verifying that a tree acts in the same way for the training and testing samples. Training stops when reaching a pre-established maximal depth or when a node remains with only signal or background events left.

4.4.2 Random boosted decision tree forests

A single tree has a main limitation: when limiting the depth, non-typical events will be incorrectly classified. On the other hand, too deep trees focus excessively on the traits of non-typical events causing inconsistency between the performance of the tree on the training and the testing sample.

The solution to the problem just exposed is to train a forest of multiple trees (generally, order of hundreds). For this analysis, the software `pybdt` [129], developed within IceCube, has been used. The code implements the process described in this paragraph.

In a forest, each tree gives a weighted contribution to the total, assigning the value -1 to events ending on background leaves and the value +1 to events ending on signal leaves. The total score for an event i can be written as

$$-s_i = \frac{\sum_t \alpha_t s_{t,i}}{\sum_t \alpha_t}, \tag{4.8}$$

where the index t indicates a tree and α_t is the weight of a tree. The term $s_{t,i}$ can only assume ± 1 values. A cut on the score distribution is then to be determined. In this work, the cut value is chosen as the one giving the best final sensitivity to signal detection.

A boosted decision tree (BDT) forest is obtained when adjusting the relative weights w_i of the events before each tree. In this way, the weights of misclassified events are boosted. If s_i are the event i scores and y_i their true classification, we can define $I_i = 1 - \delta(s_i - y_i)$, which is $I_i = 0$ when $s_i = y_i$ and 1 in any other case. The error rate of a tree will be:

$$e = \frac{\sum_i w_i I_i}{\sum_i w_i}. \tag{4.9}$$

The boost factor is:

$$\alpha = \beta \log \frac{1-e}{e}, \tag{4.10}$$

where β is usually between 0 and 1 and it is defined by the user. This parameter is used to compute the scores. The weights are adjusted with the factors $w_i \rightarrow W_i e^{\alpha I_i}$ and re-normalised. The new weights are used to train the next tree. The weight adjustment is cumulative from tree to tree.

It should be noticed that, in this process, the first trees have the highest weights and are able to classify the bulk of background events. The last trees have the lowest weights, but the weights of single events that have been misclassified multiple times are the highest, so that non-typical behaviour can be recognised and classified.

Randomisation can be added to the process by selecting only some of the parameters out of the total number of parameters used. For each tree, the parameters to use will be chosen randomly.

A process called *pruning* is used to prevent a particular kind of tree over-training. Some nodes could present a split where one side still contains useful information while the other side is adding complexity while not contributing significantly to the classification. These parts of a tree can be removed. A node whose child nodes are removed becomes a leaf. Nodes splitting into two leaves of the same kind are pruned. An algorithm cuts at a certain percentage of nodes, starting from the less useful. The pruning percentage is provided by the user.

Starting from a pool of ~ 50 variables, iterations of forests are trained and when two variables are highly correlated, the one of the two that is less contributing to the score determination is removed. For both the selections developed in this work, the final number of variables used is 10.

For the forests trained for this analysis, after a study on the impact of the parameters settings, I adopted the following:

- Number of trees: 400;
- Tree depth: 3;
- Boost β: 0.7;
- Number of random variables: 8 on a total of 10;
- Prune strength: 35%.

The training and testing samples are sub-samples of the burn sample for background, and the baseline signal channel-mass combination for LE and HE signal, respectively.

4.4.3 Low energy selection

For the low energy selection, the available statistics in simulations are limited hence a straight cut on the random forest score would keep a too low number of events to allow for a statistical analysis. Instead, I used a technique called *pull validation* [129]. It consists of training multiple forests, instead of a single one, and assigning to each event a weight determined by the fraction of forests for which an event would pass the chosen cut value on the score distribution. Each forest is trained on different sub-samples of the original training sample, ensuring that the outcome is different for each forest. The

pull-validation weight is computed in the following way:

$$w_{i,s_{cut}} = \frac{\sum_{n=1}^{N} \mathcal{H}(s_i^n - s_{cut})}{N}, \tag{4.11}$$

where i identifies the i-th event, s_i is the score of the i-th event for a forest, $s_{\rm cut}$ is the chosen cut value, $\mathcal{H}$ is the Heaviside step function, and $N_{tot} = 200$ is the total number of forests. In this way, all the events that would be discarded with one straight cut on a single score, receive instead a weight and can still be used.

The signal training and testing samples for this forests are sub-samples of signal generated in $\chi\chi \to \tau^+\tau^-$ with $m_\chi = 50$ GeV. The variables used for this forest are the following:

- `MuEx4MPE_energy`: the energy from the so-called *MuEx* reconstruction algorithm;
- `SPEFit2empty_hits_track_length`: the maximal track length of the track with no hits within a specified track cylinder radius;
- `SPEFit2n_dir_pulses`: The total number of direct pulses (hits) for the given time window;
- `SPEFit2track_hits_distribution_smoothness`: how smoothly the hits of the given hits map, within a specified track cylinder radius, are distributed along the track;
- `SplineMPEcramer_rao_theta`: estimated standard deviation on the θ value for the *SplineMPE* reconstruction;
- `SplineMPEzenith`: θ value for the *SplineMPE* reconstruction;
- `pos_z`: reconstructed interaction vertex z-coordinate for the *FiniteReco* algorithm;
- `speed_ratio_13_23`: described in section 4.3.
- `startingProb`: Probability of a track to be starting in the detector volume from the *FiniteReco* algorithm;
- `stoppingProb`: Probability of a track to be stopping in the detector volume from the *FiniteReco* algorithm.

Following what explained in paragraph 4.4.2, all the selected variables are not strongly correlated between each other, as visible in figure 4.12. Figure 4.13 is a plot of the median score distributions for each event category.

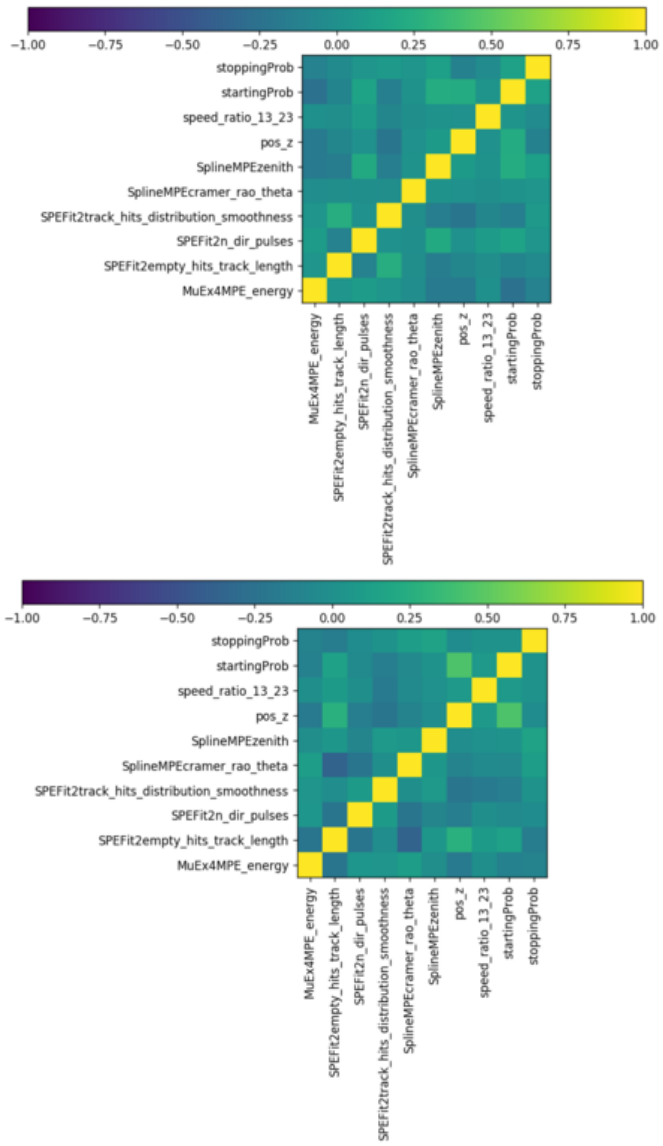

Figure 4.12 – LE forests correlation matrices for signal (top) and background (bottom) training samples. The colour scale indicates the degree of correlation between two variables with -1 *indicating no correlation and* 1 *indicating high correlation.*

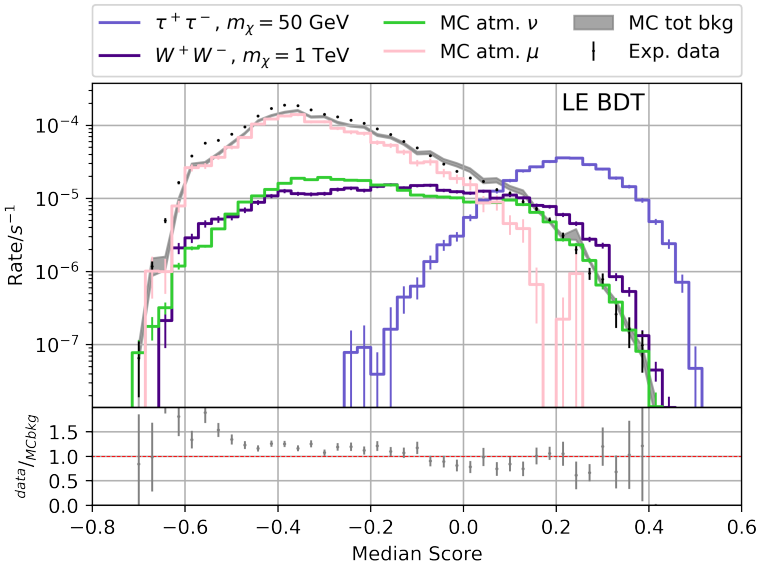

Figure 4.13 – Median score distributions for the various type of events for the LE forest presented in 4.4.3. Signal is on an arbitrary scale. Both the LE and HE reference signal configurations are shown (light and dark purple for LE and HE, respectively). Atmospheric neutrinos and muon are shown in green and pink, respectively. The grey band represents the total MC distribution, given by the sum of the atmospheric muon and neutrino distributions. The black points show the distribution of experimental data from the burn sample. The vertical bars at each bin (or point) represent the statistical errors.

4.4.4 High energy selection

For the high energy selection, I trained a single forest and applied a straight cut on the score value. The signal training and testing samples are sub-samples of the dataset generated for the annihilation channel $\chi\chi \to W^+W^-$ with $m_\chi = 1$ TeV. The variables used for this forest are:

- `LFVelZRatio`: the projection along the z-axis of the track speed calculated in the *LineFit* reconstruction;
- `SPEFit2empty_hits_track_length`: described in paragraph 4.4.3;
- `SPEFit2track_hits_distribution_smoothness`: described in paragraph 4.4.3;
- `SplineMPEcramer_rao_theta`: described in paragraph 4.4.3;
- `cog_rho`: Center of gravity ρ-coordinate;
- `cog_z`: Center of gravity z-coordinate;
- `speed_ratio_12_13`: described in section 4.3.
- `startingProb`: described in paragraph 4.4.3;
- `stoppingProb`: described in paragraph 4.4.3;
- `z_travel`: described in paragraph 4.3.

Figures 4.14 and 4.15 show the correlation matrices and score distributions obtained for this forest, respectively.

4.4.5 Score cut and next level preparation

The score cut values were chosen, for both selections, in order to optimise the sensitivity results that will be described in detail in chapter 5. For the LE selection, the best cut value was found at $s_{\mathrm{cut,LE}} = 0.24$. This means that every event is assigned a weight corresponding to the fraction of the 200 forests for which it would pass a straight cut $s_{\mathrm{ev}} > s_{\mathrm{cut,LE}}$. For the HE selection, the best cut value was found at $s_{\mathrm{cut,HE}} = 0.18$. The score cut is not applied at this point but at the latest stage of the selection process. The process which led to this choice will be described in detail in chapter 5.

Some common cuts are applied to further reduce the amount of data because of the high computational demand of the *PegLeg* (see 3.4.3) reconstruction algorithm. All events which, at the same time, do not pass the HE score cut $s_{i,\mathrm{HE}} > 0.10$ or have null weight for the LE cut $s_{i,\mathrm{LE}} > 0.14$ are discarded.

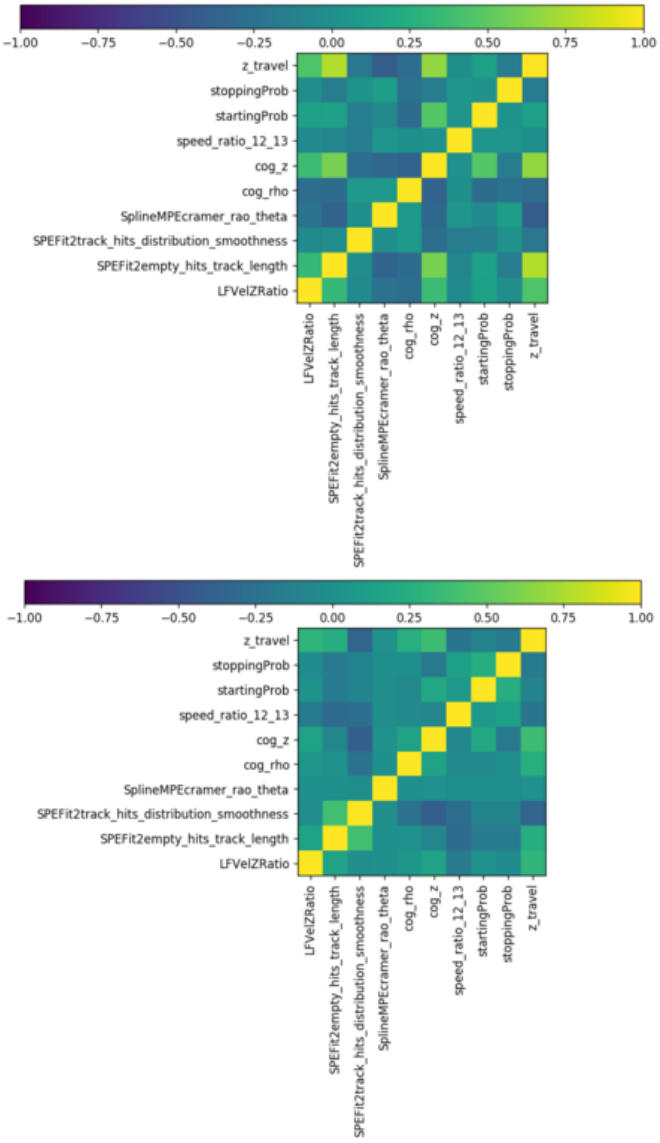

Figure 4.14 – HE forest correlation matrices for signal (top) and background (bottom) training samples. The colour scale indicates the degree of correlation between two variables with -1 *indicating no correlation and* 1 *indicating high correlation.*

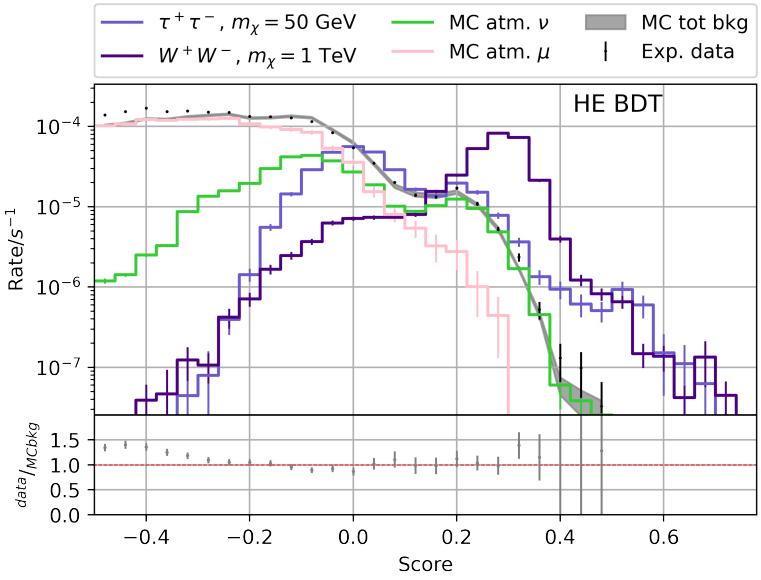

Figure 4.15 – Score distributions for the various type of events for HE forest presented in 4.4.4. Signal is on an arbitrary scale. Both the LE and HE reference signal configurations are shown (light and dark purple for LE and HE, respectively). Atmospheric neutrinos and muon are shown in green and pink, respectively. The grey band represents the total MC distribution, given by the sum of the atmospheric muon and neutrino distributions. The black points show the distribution of experimental data from the burn sample. The vertical bars at each bin (or point) represent the statistical errors.

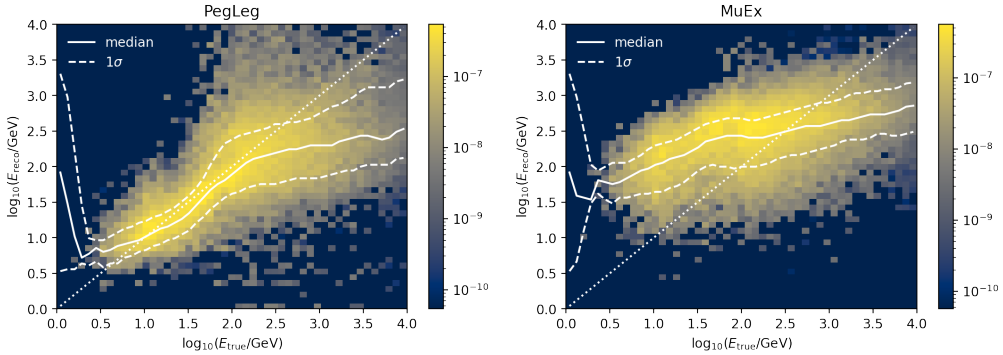

Figure 4.16 – Comparison of the PegLeg performance (left) in reconstructing the neutrino energy with the previously available reconstruction algorithm MuEx (right).

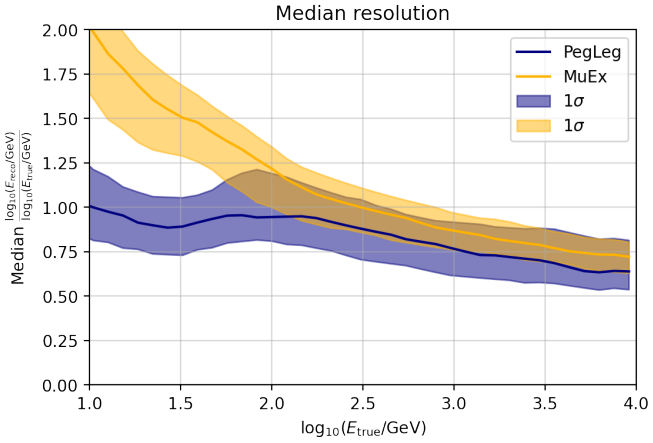

Figure 4.17 – Median resolution of the PegLeg algorithm (blue) in reconstructing the neutrino energy compared to the previously available reconstruction algorithm MuEx (yellow).

4.5 Final selection

The last step of the event selection is the application of the *PegLeg* reconstruction algorithm (see 3.4.3). This step is crucial in order to have a good energy reconstruction since energy is one of the two variables that will be used for the final analysis. Figures 4.16 and 4.17 show the outstanding improvement of *PegLeg* compared to the previously available reconstruction algorithm *MuEx*. Aside from an overall more stable behaviour, the overall average resolution in terms of $\log_{10} E$ rises to $\sim 17\%$ above 10 GeV for *PegLeg* against $\sim 28\%$ of *MuEx*, with $\sim 10\%$ resolution in the 10-1000 GeV energy region.

After the score cut, the datasets are $\gtrsim 90\%$ neutrino pure for both the LE and HE selections, as visible in figures 4.18 and 4.19. Once we have the final distributions, we can also compute the total neutrino effective areas for both the selections, which are shown in figure 4.20. In chapter 5, I will illustrate the definition of the analysis phase space, the way the score cut values were chosen, and how data are used.

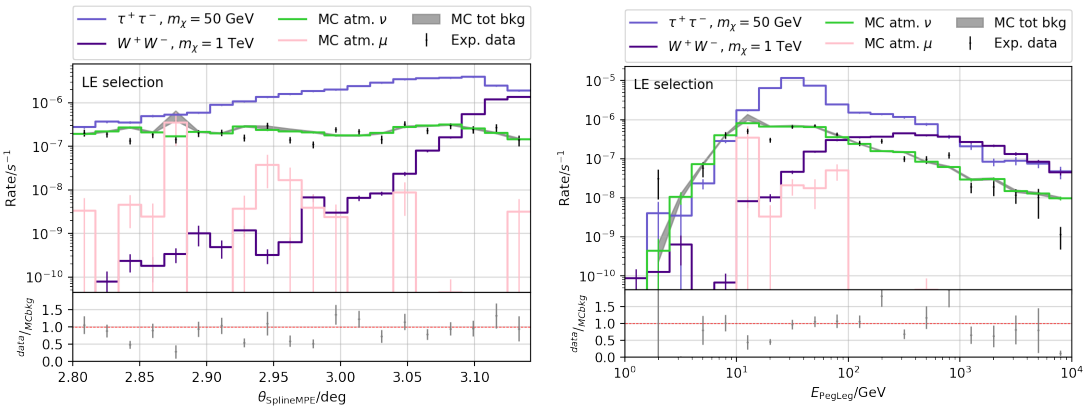

Figure 4.18 – Zenith (left) and energy (right) distributions for the LE selection after the score cut.

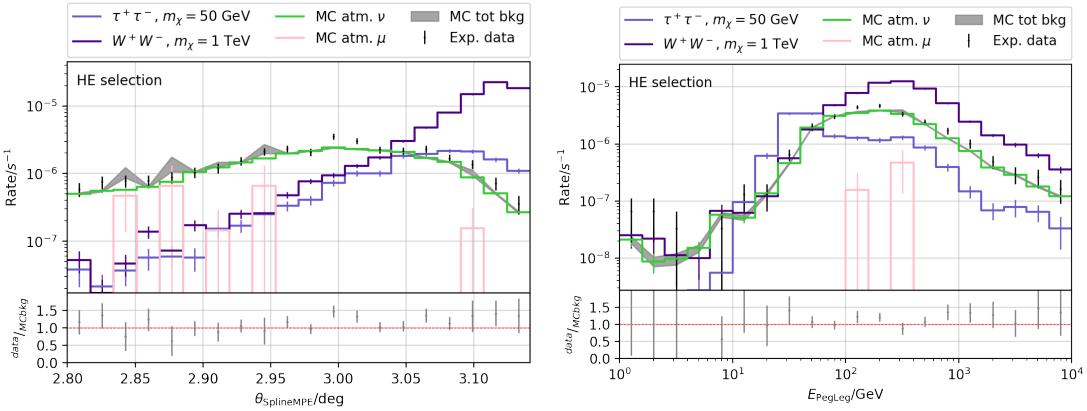

Figure 4.19 – Zenith (left) and energy (right) distributions for the HE selection after the score cut.

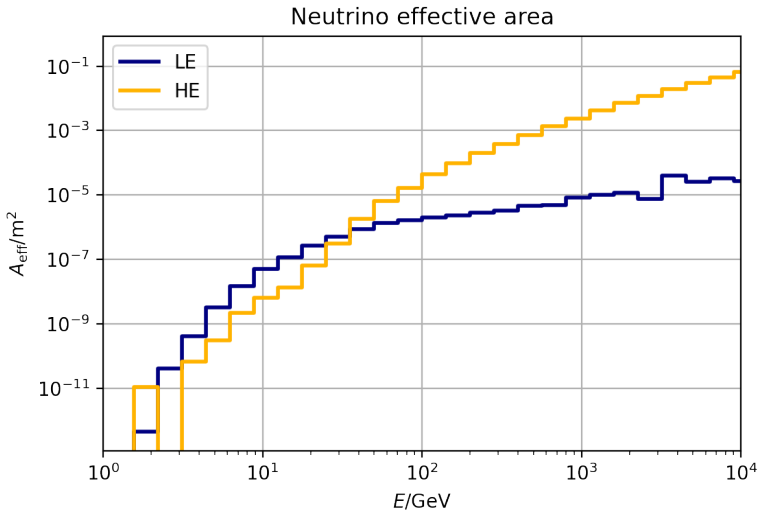

Figure 4.20 – LE (blue) and HE (yellow) neutrino effective area at the final selection level.

CHAPTER 5

THE ANALYSIS

Yes, there are two paths you can go by...

In this chapter the method I used to analyse the data is described. The statistical analysis is based on a method of maximisation of the Poisson likelihood. A 2D zenith-energy representation of data is used. I estimated sensitivities as the median upper limit on ten thousand pseudo-experiments. A description of the study I carried out on the systematic effects that could affect the result is also presented. The likelihood includes some nuisance parameters to handle the unknowns of the real data distribution that could not be included in the simulations or the systematic variations. The way data are handled and the analysis procedure will be illustrated in section 5.1. A discussion on the systematic uncertainties will follow in section 5.2 and sensitivities obtained for the analysis will be presented in section 5.3.

5.1 A binned likelihood analysis

For this analysis we are considering two observables: the zenith angle θ and the energy in the form $\log_{10} E$. 2D distributions in the θ-$\log_{10} E$ plane for signal and background are used to build probability density functions (PDFs). As mentioned in chapter 4, the peculiar direction observed does not allow for a representation of the signal and background distributions derived from real data so the PDFs are built on MC data. The likelihood used in this work is the Poisson likelihood which is binned, therefore the PDFs will be binned distributions. In this section, I present the PDFs and describe the analysis method developed for this work.

5.1.1 The Probability Density Function

As previously mentioned, because the Poisson likelihood is a binned one, the model to analyse must be a binned distribution λ. Being i the i-th bin of the model we can write:

$$\lambda_i(\xi, \overrightarrow{n}) = \xi S_i + (1-\xi)B_i(\overrightarrow{\eta}), \tag{5.1}$$

where ξ is the signal fraction of the total number of events while $S_i = S_i(\theta, E)$ and $B_i = B_i(\theta, E)$ are the signal and background PDFs content in the bin i, respectively. The following background components are considered: conventional atmospheric neutrinos, astrophysical neutrinos, prompt neutrinos and atmospheric muons. Neutrinos of astrophysical origin are to be considered a minor background contribution based on the IceCube measurements [19] [17] in the energy range and the direction we are observing. Neutrinos from prompt interactions in the atmosphere are a secondary contribution from atmospheric interactions, due to the decay of short-lived particles. We expect their contribution to be several orders of magnitude below the classic atmospheric contribution. All neutrino backgrounds are obtained by re-weighting the neutrino simulated events. Atmospheric muons constitute a secondary background that CORSIKA simulations indicate to be about $\sim 10\%$ of the total background. The relative normalisation of each flux component n_i is taken as a free nuisance parameter and encapsulated in $\overrightarrow{\eta} = (n_1, n_2, n_3...)$. For the background PDF $B(\overrightarrow{\eta})$ I developed the following formulation for an arbitrary number of parameters n_j:

$$\begin{aligned} B_i(\overrightarrow{\eta}) = n_1 B_i^1 + \sum_{j=1}^{n-1}\prod_{k=1}^{j-1}(1-n_k)n_j B_i^j + \prod_{k=0}^{n-1}(1-n_k)B_i^n = \\ = n_1 B_i^1 + (1-n_1)(n_2 B_i^2 + (1-n_2)(n_3 B_i^3 ... + (1-n_n)B_i^n), \end{aligned} \tag{5.2}$$

where the $B_i^j = B_i^j(\theta, E)$ are content for the bin i for the various components j of the background aforementioned. The atmospheric neutrino component is, in turn, split into a NuGen and a GENIE component, to handle a mismatch between the distributions produced by the two pieces of software which will be discussed in detail in 5.2.

The Probability Density Function (PDF), for each bin i, can now be written in its final form:

$$\begin{aligned} \lambda_i = n_0 S_i + \sum_{j=1}^{n-1}\prod_{k=0}^{j-1}(1-n_k)n_j B_i^j + \prod_{k=0}^{n-1}(1-n_k)B_i^n = \\ = n_0 S_i + (1-n_0)(n_1 B_i^1 + (1-n_1)(n_2 B_i^2 + ... + (1-n_n)B_i^n). \end{aligned} \tag{5.3}$$

The corresponding fractions of events for the B_i are, hence, given by:

$$f_j \equiv \prod_{k=0}^{j-1}(1-n_k)n_j, \tag{5.4}$$

except for the last term in (5.3), for which we have:

$$f_n = \prod_{j=0}^{n-1}(1-n_j). \tag{5.5}$$

The first term is the signal fraction and is simply defined as:

$$f_0 = n_0 = \xi, \tag{5.6}$$

For the components used in this work we have therefore the following:

- NuGen atmospheric neutrinos: $f_{\mathrm{NuG}} = (1-\xi)n_1$;
- GENIE atmospheric neutrinos: $f_{\mathrm{GEN}} = (1-\xi)(1-n_1)n_2$;
- Atmospheric muons: $f_{\mu} = (1-\xi)(1-n_1)(1-n_2)n_3$;
- Prompt neutrinos: $f_{\mathrm{prompt}} = (1-\xi)(1-n_1)(1-n_2)(1-n_3)n_4$;
- Astrophysical neutrinos: $f_{\mathrm{astro}} = (1-\xi)(1-n_1)(1-n_2)(1-n_3)(1-n_4)$.

In brief, in this formulation the various parameters are nested one into each other and, having n components in the model, $n-1$ parameters are needed. This optimisation allows for a computationally less demanding likelihood maximisation. This formulation also assures a proper normalisation of the model. Notice that the chosen order of the parameters is irrelevant for the likelihood calculations.

Data which underwent the whole selection process described in chapter 4 are ready to be analysed. The reconstructed zenith and energy values, from the SplineMPE and PegLeg algorithms, respectively, are put in a binned 2D distribution of the events to build the PDFs. As explained before, all the single component PDFs are built on MC data. As for the score cut value (see 4.4), the number of bins to be used is chosen as the one optimising the sensitivity. PDFs include events in the $160^\circ \lesssim \theta < 180^\circ$ zenith angle range, while the range $149^\circ \lesssim \theta \lesssim 160^\circ$ has been used to check the data-MC agreement before analysing the full IceCube dataset.

To cope with statistical fluctuations due mainly to low statistics in the simulations, a Kernel Density Estimation (KDE) of the distributions is computed. The KDE method consists of approximating each event with a 2D Gaussian whose normalisation is determined by the event weight. The width of the Gaussians is an important settable parameter: a too-thin bandwidth would bring a distribution which is not different from the original data distribution; on the other hand, a too-large bandwidth would produce a uniform distribution where all the events' Gaussians are superposed to each other. The optimal bandwidth has been found with the cross-validation method [121], consisting of scanning bandwidth values to find the one giving the most reliable description compared to the original data without losing the stabilisation of fluctuations that the estimation is seeking. Figure 5.1 shows, as an example, the LE atmospheric neutrino PDF, comparing the used PDF, which is a KDE, and a PDF built without a KDE of the MC data distribution. It is visible to the eye that the KDE-based model smooths the fluctuations while preserving the overall shape of the original distribution.

All the PDFs are normalised to 1 so the model built in (5.3) is also normalised to 1 by construction. The final normalisation is given by multiplying the model in (5.3) by the total number of events observed. For the sensitivity calculations, as we are blind to the real data, we obtain this number from the burn sample, by multiplying its events rate at the final selection stage by the total livetime. It is important to take burn sample runs sparsely over the whole ten years of IceCube data-taking, to reduce at the minimum the biases due to seasonal variations and possible variations along the course of time in the detected neutrino flux. In the unblinding process, the number used is the actual number of events in the observed IceCube data at the final selection stage.

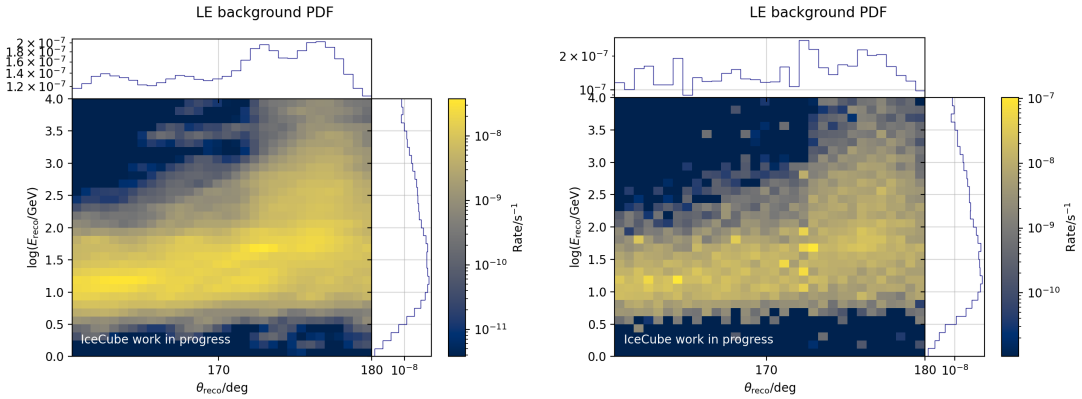

Figure 5.1 – Comparison between the atmospheric background PDF built using a KDE (left) and without KDE (right). The KDE preserves the original overall shape of the distribution while reducing the spikes due to fluctuations.

Low energy analysis

The low energy analysis is performed in the 1 GeV $< E < 10^4$ GeV energy range. Despite the pull-validation method used to apply the random forest score cut, the statistics are very low so the KDE estimation is crucial in order to have a meaningful representation of data. The optimised number of bins is 32×32. Figure 5.2 shows the PDFs for signal and the three neutrino background components. A $\sim 10\%$ atmospheric muon contribution is present for the LE selection.

High energy analysis

Statistics for the HE selection are higher than for LE hence the KDE needs a smaller bandwidth compared to the LE analysis. Also, the optimal number of bins found is higher, being 100×100. A marginal atmospheric muon component is still present, being $< 10\%$ of the total. The PDFs for the HE analysis for signal and the neutrino background components are shown in figure 5.3.

5.1.2 The Poisson likelihood

Being k the number of observed events to be compared to the model λ, where k_i and λ_i are the i-th bin contributions to the observation and the model, respectively, the Poisson likelihood is defined as:

$$\mathcal{L}(\lambda) = \mathcal{L}(\xi, \overrightarrow{\eta}) = \prod_i^{N_{\text{bins}}} \frac{\lambda_i^{k_i} e^{\lambda_i}}{k_i!}. \tag{5.7}$$

where ξ is the physics parameter and $\overrightarrow{\eta}$ is the set of nuisance parameters. As the likelihood $\mathcal{L}$ typically assumes high values, it is preferable to work with the logarithm

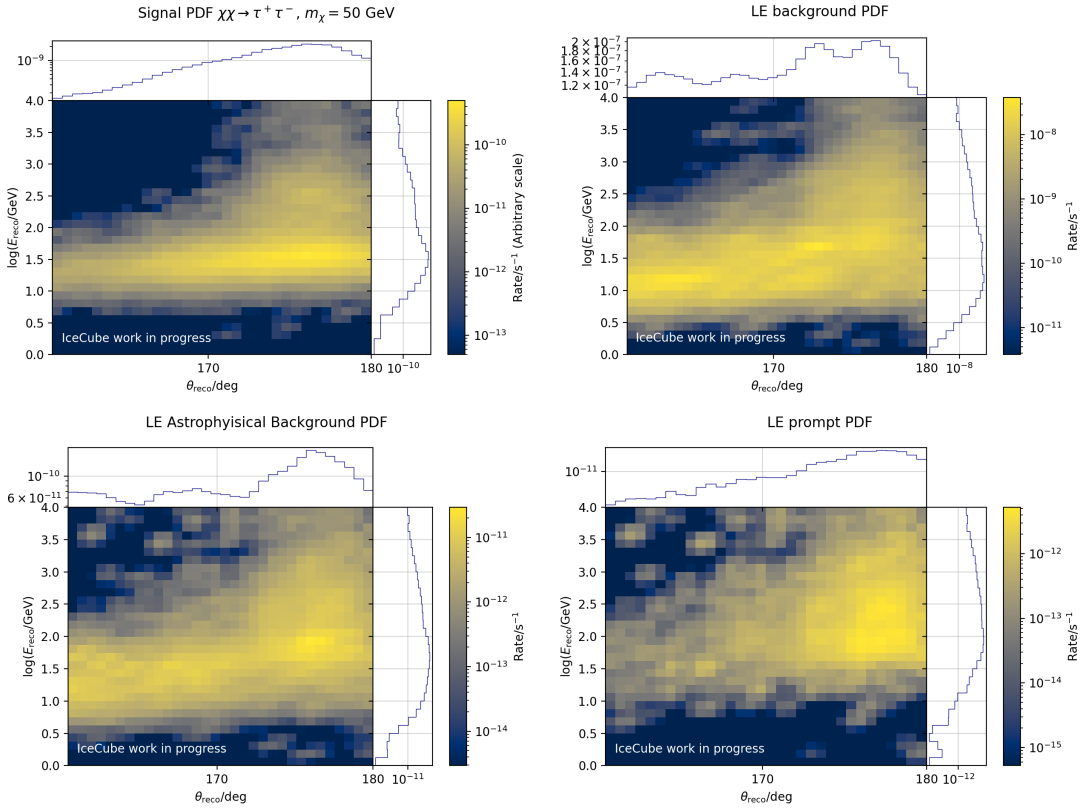

Figure 5.2 – PDFs for the LE analysis. They correspond to the KDE of the 2D zenith angle-energy logarithm distributions. The colour scale indicates the rate of the component represented. Top left: Signal baseline (Arbitrary normalisation) $\chi\chi \to \tau^+\tau^-$, $m_\chi = 50$ GeV. Top right: Standard atmospheric neutrinos. Bottom left: Astrophysical neutrinos. Bottom right: Prompt neutrinos.

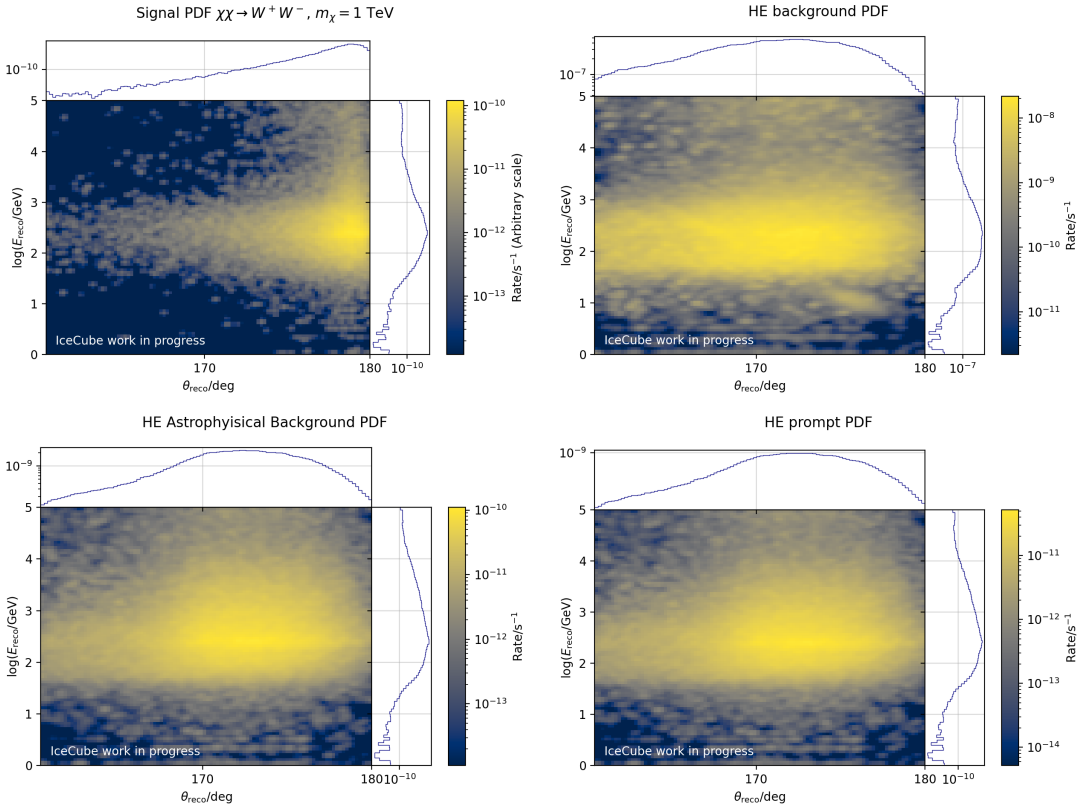

Figure 5.3 – PDFs for the HE analysis. They correspond to the KDE of the 2D zenith angle-energy logarithm distributions. The colour scale indicates the rate of the component represented. Top left: Signal baseline (Arbitrary normalisation) $\chi\chi \to W^+W^-$, $m_\chi = 1$ TeV. Top right: Standard atmospheric neutrinos. Bottom left: Astrophysical neutrinos. Bottom right: Prompt neutrinos.

of the likelihood (or *log-likelihood*). We can hence write:

$$-\log \mathcal{L}(\xi, \overrightarrow{\eta}) = \sum_{i}^{N_{\text{bins}}} (-k_i \log \lambda_i + \lambda_i), \tag{5.8}$$

where the term $\log(k_i!)$ has been dropped since for the analysis method used, which will be described in the following paragraph, it cancels out and it is independent of the model λ. Notice that the shift to $-\log \mathcal{L}$ transforms the mathematical problem into a minimisation one.

5.1.3 The analysis method

For the analysis, I define the test statistic using the ratio between the minimum likelihood $\mathcal{L}(\xi, \hat{\overrightarrow{\eta}})$ when fixing the signal fraction ξ and the absolute minimum likelihood (best fit) $\mathcal{L}(\hat{\xi}, \hat{\overrightarrow{\eta}})$ [71]:

$$t_\xi = 2 \log \frac{\mathcal{L}(\xi, \hat{\overrightarrow{\eta}})}{\mathcal{L}(\hat{\xi}, \hat{\overrightarrow{\eta}})} = 2(\log \mathcal{L}(\xi, \hat{\overrightarrow{\eta}}) - \log \mathcal{L}(\hat{\xi}, \hat{\overrightarrow{\eta}})). \tag{5.9}$$

The case t_0 is used for background rejection. Its value describes how much the null hypothesis $\xi = 0$ is in disagreement with the observation. Under the assumption that we can test an infinite number of observations over the null hypothesis the Wilks' theorem [144] holds and the distribution of t_0 is described by:

$$f(t_0|0) = \frac{1}{2}\delta(t_0) + \frac{1}{2}\frac{1}{2\pi}\frac{1}{t_0}e^{-t_0/2}, \tag{5.10}$$

which is the sum of half a delta function and half a χ^2 distribution, and can be referred to as a *half-chi-square distribution*. The p-value is an indicator of the compatibility between the observation and the background-only hypothesis, and is defined as:

$$p_0 = \int_{t_{0,obs}}^{\infty} f(t_0|0) dt_0, \tag{5.11}$$

where $t_{0,obs}$ is the observed value of t_0. It is demonstrated [71] that the significance Z_0 of the deviation from the background-only hypothesis can be obtained with:

$$Z_0 = \sqrt{t_0}. \tag{5.12}$$

The p-value can be obtained via:

$$p_0 = 1 - \Phi(Z_0), \tag{5.13}$$

where Φ is the cumulative distribution of the standard Gaussian. A significance of 5σ (i.e. $Z_0 = 5$) corresponds to $p_0 = 5.7 \times 10^{-7}$ and it is the common condition to claim a discovery. A significance of 3σ constitutes evidence for the presence of a signal.

In case of no discovery, the 90% confidence level (C.L.) upper limit on the signal strength can be computed. This corresponds to a threshold p-value $p = 0.1$. The value of $\xi_{\rm up}$ is the one which gives:

$$t_0 - t_{\xi_{\rm up}} = \Phi^{-1}(1-p) = 1.64. \tag{5.14}$$

The likelihood space can be altered using *prior* Gaussian functions to prevent the possibility that a likelihood prefers physically non-acceptable fits. Two priors were implemented for this likelihood:

- Astrophysical prior: to prevent the astrophysical contribution from assuming values higher than the IceCube measured flux. Starting from the parametrisation given in table 4.1, the astrophysical contribution should not overcome the upper one standard deviation of the measurement as visible in figure 3.6. The Gaussian parameters are hence set to:

$$\mu_{\rm astro} = \sigma_{astro} = \frac{N_{\rm astro}(n_{\rm IC} + \sigma_{\rm IC})}{N_{tot} n_{\rm IC}}, \tag{5.15}$$

  where $N_{\rm astro}/N_{tot}$ is the fraction of astrophysical neutrinos expected from weighting the MC neutrino with the flux in table 4.1. $n_{\rm IC}$ is the normalisation of the given flux, while $\sigma_{\rm IC}$ is the upper one standard deviation of $n_{\rm IC}$. A condition is set on the astrophysical fraction $f_{\rm astro}$, computed in the likelihood with equations (5.4) and (5.5), in the following way:

$$\begin{cases} f_{\rm astro} \leq \mu_{\rm astro} : \mathcal{A} = 1 \\ f_{\rm astro} > \mu_{\rm astro} : \mathcal{A} = \mathcal{G}(\mu_{\rm astro}, \sigma_{\rm astro}), \end{cases} \tag{5.16}$$

  where $\mathcal{A}$ is the astrophysical prior, which is 1 when the astrophysical fraction $f_{\rm astro}$ is below or equal to the maximum acceptable fraction, while it's a Gaussian $\mathcal{G}$ otherwise.

- GENIE-NuGen prior: to prevent the relative variation between the GENIE and NuGen components to be more than 20%. The condition was convened in an internal discussion within the IceCube collaboration and more details will be given in the following section. In this case, the parameter $p_{\rm ratio}$ on which the condition is set is:

$$p_{\rm ratio} = \frac{|r - r_0|}{r_0}, \tag{5.17}$$

  where r is the ratio between the GENIE and NuGEn fraction of atmospheric neutrinos $r = f_{\rm GENIE}/f_{\rm NuGen}$, where the two fractions were again obtained using equations (5.4) and (5.5) while r_0 is the ratio given by the MC datasets after the whole event selection. The Gaussian parameters are:

$$\mu_{\rm ratio} = \sigma_{\rm ratio} = 0.2, \tag{5.18}$$

  and the prior is defined as:

$$\begin{cases} p_{\rm ratio} \leq 0.2 : \mathcal{R} = 1 \\ p_{\rm ratio} > 0.2 : \mathcal{R} = \mathcal{G}(\mu_{\rm ratio}, \sigma_{\rm ratio}), \end{cases} \tag{5.19}$$

  where $\mathcal{R}$ is 1 when the parameter $p_{\rm ratio}$ is smaller than 0.2 and a Gaussian $\mathcal{G}$ otherwise.

The final form of the likelihood can, hence, be written as:

$$\mathcal{L} \times \mathcal{A} \times \mathcal{R}, \tag{5.20}$$

and the negative log-likelihood is:

$$-\log \mathcal{L} - \log \mathcal{A} - \log \mathcal{R}. \tag{5.21}$$

The code for this method has been implemented in `python` in a collaborative project developed within our working group in the context of this and other analyses [52] [98] on dark matter. In particular, I implemented the code structure needed to use more than one parameter in the likelihood, including the nested PDF formulation, and the possibility of using priors. The minimiser chosen for the likelihood minimisation is the `python` version of Minuit [100] called `iminuit` [74].

5.2 Systematic uncertainties

Since this work heavily relies on simulations, estimating systematic uncertainties is fundamental. In this section, effects that could affect the correct prediction of the signal and background fluxes are considered. Estimation of the systematic uncertainties is important to cope with the unknowns in the adopted modelling and the assumptions made for which an unambiguous choice cannot be made. The following paragraphs will illustrate the different kinds of systematic effects to account for, which include: uncertainties in the propagation of light in the Antarctic ice, uncertainties in the detector response to incoming light pulses, and physics uncertainties. All systematic effects are tested individually directly in the post-unblinding phase, studying how the variations affect the likelihood minimum value and the number of signal events estimated by the fit. The final result corrected for the systematic effects will correspond to the systematic variation which gives the minimum negative log-likelihood among all those analysed.

5.2.1 Uncertainties on the propagation of light

The hole ice is the ice which froze around the DOMs after the hot water drilling used to put the strings in place. This hole ice has been observed to have different optical properties than the common South Pole ice. The effect of the hole ice on light propagation and detector efficiency is described by two parameters p and p_2. The first affects the acceptance of incoming photons depending on their incoming direction η and has a value $p = 0.25 + 0.1$. The second parameter only affects the vertical up-moving photons. The acceptance for these directions is not well constrained so that the nominal value is $p_2 = 0$. Values of $p_2 < 0$ mean a lower efficiency in photon detection for high η, while values of $p_2 > 0$ indicate a higher efficiency. The influence of the choice for these parameters on the η-dependent acceptance is shown in figure 5.4. For this analysis, the values $p = 0.3$, $p_2 = 0$ have been set as baseline. As the parameter p_2 is the one expected to most affect the detection of very vertical up-going events, we consider variations $p_2 = \pm 1$ to estimate the systematic uncertainty due to the hole ice effects.

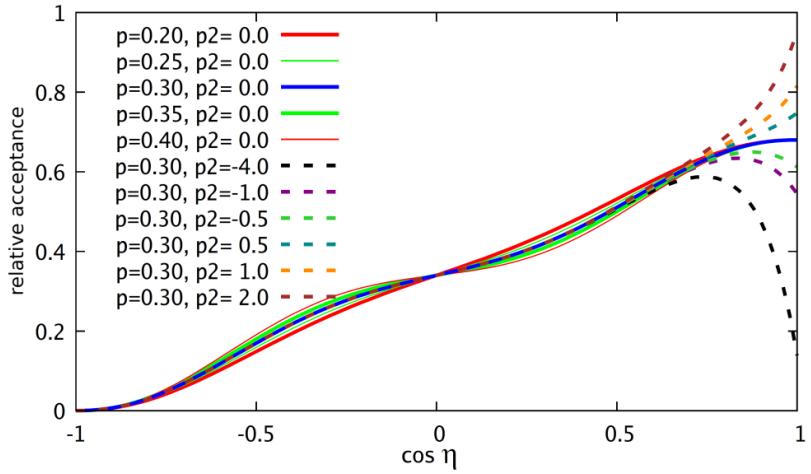

Figure 5.4 – Relative photon angular acceptance of various hole ice models obtained varying the values of p and p_2. From [105].

5.2.2 Uncertainties on the detector response

The overall DOM efficiency of photon detection depends on the PMT efficiency, other hardware effects and the ice surrounding the DOMs. We expect an uncertainty of $\pm 10\%$ around the baseline DOM efficiency. Variations of $\pm 10\%$ are, hence, considered for this analysis. A higher DOM efficiency than the nominal would allow for more low-energy events to be detected, while a lower DOM efficiency would make the average detected event energy to be higher. Therefore, DOM efficiency variations not only affect the overall normalisation (which is irrelevant for our analysis construction) but also the shape of our PDFs, enhancing, in turn, low- or high-energy events. The zenith distributions are also affected since higher energy events tend to be more vertical with directions closer to $\sim 180°$ and generally have better angular reconstruction.

5.2.3 Physics uncertainties

Atmospheric neutrino flux

The estimation of the atmospheric neutrino flux with simulations requires a model of the cosmic ray interactions in the atmosphere. The complexity of the atmospheric interactions does not allow for a perfect representation of reality. Two alternative weighting schemes are, therefore, tested along with the nominal one: the *CORSIKA* [131] and the *Bartol* [49] models. A plot resuming a collection of neutrino fluxes is shown in figure 5.5.

A disagreement between the GENIE and NuGen neutrino generators in the region around ~ 100 GeV has been observed when comparing the two energy distributions. The GENIE rate at these energies is lower by $\sim 10\%$ compared to the NuGen rate, creating a gap when switching from GENIE to NuGen at 100 GeV. The mismatch is probably ascribable to the different neutrino cross-section modelling used by the two pieces of

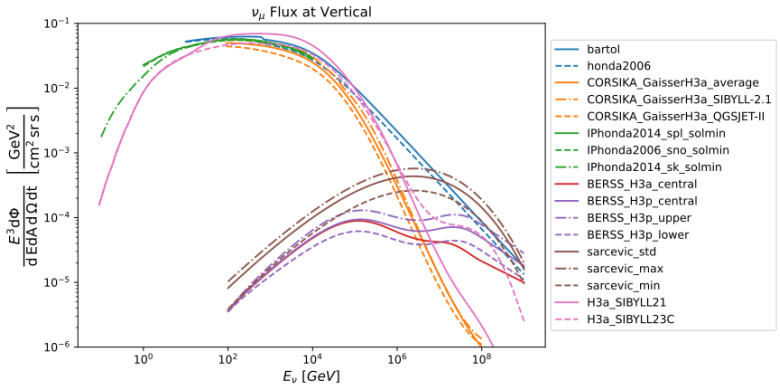

Figure 5.5 – A view of various flux models, including the nominal Honda model (dashed blue line), the Bartol model (continuous blue line), the CORSIKA model (continuous orange line) used for systematics studies and the Sarcevic model for prompt neutrinos assumed in this work (continuous brown line). From IceCube internal resources.

software, as GENIE must use a more complete implementation of the various possible interactions and tunes the different parameters to colliders results [44], while NuGen is based only on DIS interactions [86] (see 2.3 for more details on neutrino interactions) based on the so-called *CSMS* model [69]. We decided to split the atmospheric neutrino contribution into a GENIE and a NuGen component directly in the likelihood formulation. This implementation allows the two components to vary relative to one another. Also, in the region $100\,\text{GeV} < E_{\text{true}} < 200\,\text{GeV}$, NuGen event weights are gradually increased from 0% to 100 % while decreasing GENIE event weights in the opposite way. The total GENIE and NuGen rates, respectively, are re-normalised to the original rates before this step. This technique is used to smooth the passage between the two cross-section models, as visible in figure 5.6. A prior function, introduced in the previous section, assures that the relative variation between the two is not larger than 20%.

Astrophysical neutrino flux

We expect a contribution of astrophysical neutrinos of less than 1% of the total number of events from the IceCube astrophysical flux measurement (see 3.5.1). For high-energy signal configurations, we also expect the astrophysical energy distribution to be similar to the signal one. This fact could push the minimisation process of the likelihood to prefer to boost the astrophysical contribution instead of signal. Therefore, we applied a prior function (see previous section) to prevent the astrophysical flux to deviate more than $+1\sigma$ from the nominal value, following the results in [134].

Oscillation parameters

Since we are analysing an up-going neutrino flux, the events hit the detector after crossing the entire, or half, the Earth for background or signal events, respectively. The Earth enhances oscillation, as explained in 2.1.1, causing the muon-disappearance and tau-appearance effects. Given that the oscillation parameters have not been precisely

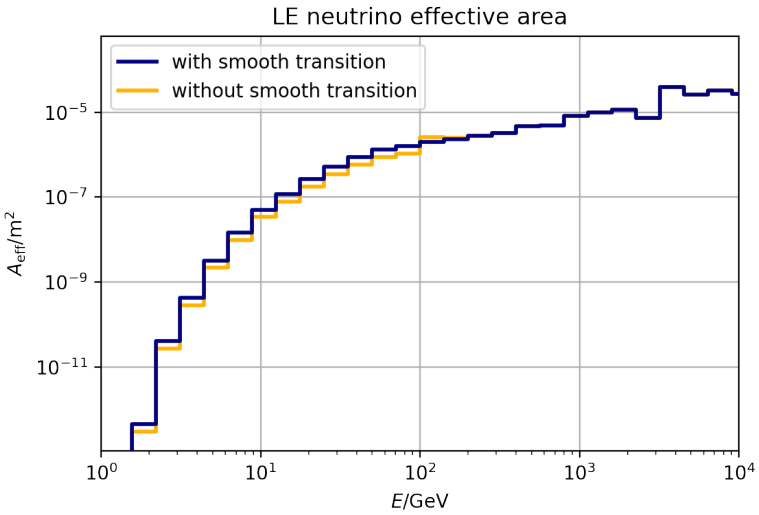

Figure 5.6 – Comparison between the LE neutrino effective area used in this work (blue) (see also 4.5) and one where the smooth transition between GENIE and NuGen is not applied (yellow). The latter presents a mismatch between GENIE and NuGen at 100 GeV.

measured yet, it is important to probe some alternative oscillation scenarios. A summary of the parameter variations used can be found in table 5.1.

Bedrock

IceCube results can, in principle, be affected by the lack of measurement of the exact depth of the bedrock below the South Pole ice. However, an internal IceCube study has estimated, for neutrinos incoming from the direction of the centre of the Earth, that the impact is less significant than the statistical fluctuations, at the level of $\sim 1\%$ of the total number of events. A variation of the bedrock position is, hence, not considered in this work.

Name	Δm^2_{21}	Δm^2_{31}	$\sin^2\theta^2_{21}$	$\sin^2\theta^2_{31}$	$\sin^2\theta^2_{32}$	δ_{CP}
Nominal	$7.53 \cdot 10^{-5}$	$2.45 \cdot 10^{-3}$	0.307	0.021	0.510	0
IceCube fit	$7.53 \cdot 10^{-5}$	$2.38 \cdot 10^{-3}$	0.307	0.021	0.510	0
Inverted order	$7.53 \cdot 10^{-5}$	$-2.46 \cdot 10^{-3}$	0.307	0.021	0.539	0
δ_{CP} phase	$7.53 \cdot 10^{-5}$	$2.45 \cdot 10^{-3}$	0.307	0.021	0.510	4.27

Table 5.1 – Oscillation systematic variations parameters, including the IceCube fit values from [14], an inverted mass order set from [150] and a set with a δ_{CP} phase, with the δ_{CP} value taken from [150].

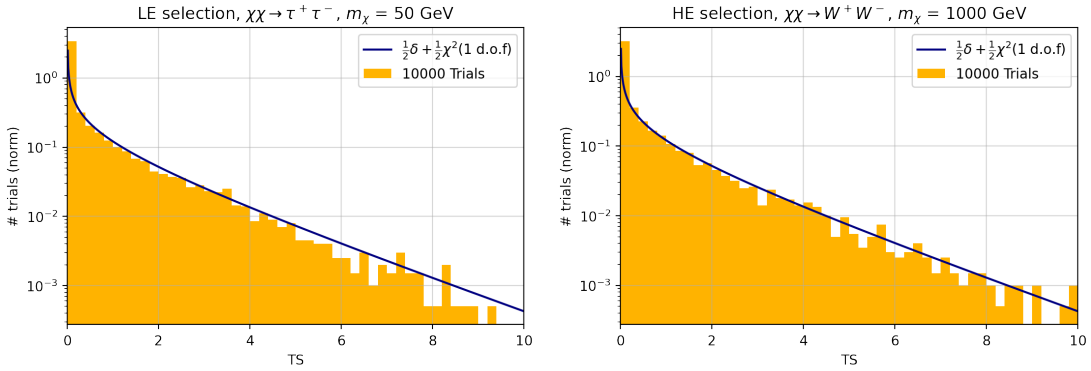

Figure 5.7 – Test-statistic distribution for the baseline LE (left) and HE (right) DM configuration. The distribution follows in both cases a half-chi-square distribution.

5.3 Sensitivities

The method described in 5.1 has been used to compute blind sensitivities in this work. Each dark matter configuration (mass and channel) is analysed individually both in the LE and HE analyses. An unblinding procedure has been prepared following an IceCube internal review of the sensitivity results presented in this chapter. Unblinded results will be presented in 6.

A frequentist approach is used to estimate the upper limits on the presence of signal. Ten thousand pseudo-experiments are built as Poisson variations of the background PDF (see 5.1.1 for more details). For each pseudo-experiment, the upper limit is computed via the method illustrated in 5.1.3. The median value $\langle \xi^{90\%\mathrm{CL}} \rangle$ of the upper limit distribution from the ten thousand trials is the sensitivity at the 90% C.L.

A test is necessary to verify that ten thousand trials are a number high enough to apply the analytical method described in 5.1.3. When this is the case, the test-statistic distribution follows the half-chi-square distribution. Figure 5.7 shows, as an example, this test for the two baseline LE and HE DM scenarios, respectively. Wilks' theorem is applicable for all the DM configurations. The complete set of test-statistic distributions will be shown in chapter 6 and appendix A.

5.3.1 Volumetric flux

Sensitivities on the volumetric flux $\Gamma_{\nu\to\mu}$ can be obtained with a simple conversion:

$$\Gamma_{\nu\to\mu} = \frac{\langle \xi^{90\%\mathrm{CL}} \rangle N_{\mathrm{tot}}}{V_{\mathrm{eff}} t_{\mathrm{livetime}}}. \tag{5.22}$$

In (5.22), N_{tot} is the total number of events, estimated from the burn sample final rate, t_{livetime} is the total livetime considered for this analysis, corresponding to $t_{\mathrm{livetime}} \simeq 3265.85$ days of detector activity, and V_{eff} is the effective volume for the specific dark matter configuration and analysis considered. The latter represents the ratio between the number of signal events in the final selection and the total number of generated

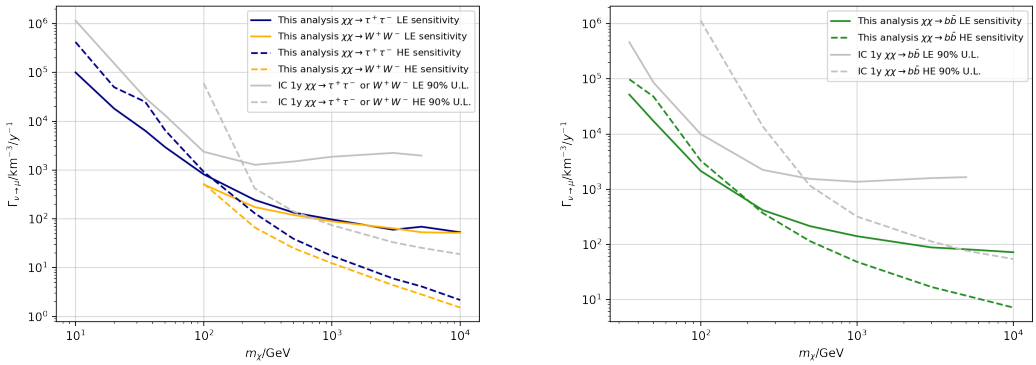

Figure 5.8 – Volumetric flux sensitivities as a function of the DM mass compared to the previous 1-year IceCube analysis limits. Left: $\chi\chi \to \tau^+\tau^-$ and $\chi\chi \to W^+W^-$ channels. Right: $\chi\chi \to b\bar{b}$ channel.

events in the generated volume from WimpSim [57] [76] simulations [103]. An effective volume V_{eff} is computed for each of the considered DM configuration for both the LE and HE selections.

Figure5.8 show the sensitivities in terms of volumetric flux for the three channels analysed and the two LE and HE analyses. showing, for comparison, the results of the IceCube 1-year analysis [103] [12].

5.3.2 Annihilation rate

The relation between volumetric flux and annihilation rate is described by [101]:

$$\Gamma_{\nu\to\mu} = \frac{\Gamma_{\text{A}}}{4\pi R^2} \int_0^\infty dE_\nu \sigma_{\nu N}(E_\mu|E_\nu)\rho_N \sum_F B_F \left(\frac{dN_\nu}{dE_\nu}\right)_{F,\mu}(E_\nu), \tag{5.23}$$

where, in this case, $R = R_\oplus$ is the Earth radius, $\sigma_{\nu N}$ is the neutrino-nucleon cross-section, ρ_N is the nucleon density at the detector, B_F are the branching fractions and $(dN_\nu/dE_\nu)_{F,\mu}$ are the neutrino spectra for the for the different DM annihilation channels. The conversion from volumetric flux to annihilation rate is computed using the WimpSim code [57] [76].

The results obtained for the annihilation rate for all channels and for the LE and HE analyses are presented, compared to the 1-year analysis [12] [103] in figure 5.9.

5.3.3 Spin-independent dark matter-nucleon cross-section

To obtain the final limits on the spin-independent DM-nucleon cross-section, the differential equation (1.37), which describes the evolution of the DM density at the centre of the Earth, is solved numerically for C_{C}. The first relation in equation (1.40) and equation (1.36) are used to quantify the ratio $t_\oplus/\tau$. In particular, equation (1.36) shows that $C_A \propto \langle\sigma_{\text{A}} v\rangle$, so that an assumption on $\langle\sigma_{\text{A}} v\rangle$ must be made. The common assumption

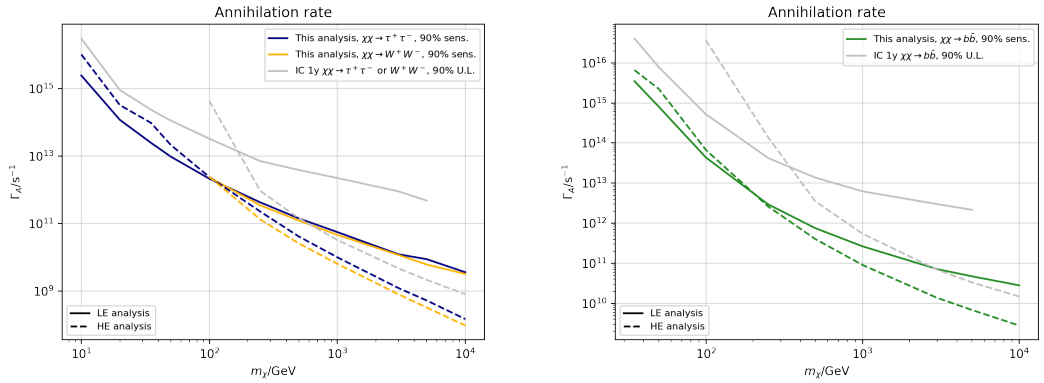

Figure 5.9 – Annihilation rate sensitivities including the 1-year IceCube analysis limits. Left: $\chi\chi \to \tau^+\tau^-$ and $\chi\chi \to W^+W^-$ channels. Right: $\chi\chi \to b\bar{b}$ channel.

in searches for dark matter from the centre of the Earth is its thermal value derived from the freeze-out mechanism (see 1.2.3): $\langle\sigma_A v\rangle = 3 \times 10^{-26}$ cm^{3}s^{-1}. Once C_C values are obtained, equation (1.33) describes the relation between C_C and $\sigma^{\chi p}_{scalar} \equiv \sigma_{SI}$, showing that the two quantities are linearly proportional. Equation (1.33) is solved for σ_{SI} with WimpSim [57] [76]. Figure 5.10 shows how the value of σ_{SI} changes depending on the choice on $\langle\sigma_A v\rangle$ for the all channel-mass configurations considered.

A unique line is drawn for each of the two LE and HE selections choosing, for each mass, the selection which gives the best sensitivity. Since only discrete values of the DM mass are evaluated, points in between the selected mass values presented in table 4.3 are computed via linear interpolation and shown only to guide the eye. Figure 5.11 presents the sensitivity results for this work, and includes, for comparison, the most recent results from ANTARES [40] and Super-Kamiokande [110].

5.4 Unblinding Plan

Once the sensitivities have been computed we can pass to the real data analysis. An unblinding plan must be defined in advance, in order to keep the analysis unbiased. The unblinding procedure has also been tested on fake data (generated in the same way as the pseudo-experiments) and on the burn sample to make sure the implementation was correct.

For each DM scenario, I only run the analysis (LE or HE) that gives the best sensitivity. Therefore, the LE analysis will be used for masses up to 100 GeV and the HE analysis for higher masses, up to 10 TeV. The configuration $\chi\chi \to \tau^+\tau^-$, $m_\chi = 10$ GeV shows a lack of statistics in building the corresponding signal PDF from MC simulations. Considering also the fact that the sensitivity for this mass is not particularly competitive, it was decided to omit this point.
For each configuration tested the best fit is found and the value t_0 is computed. The best fit result contains the measured signal fraction of the total events along with the nuisance parameters, from which the events fractions for the other components can be computed (see 5.1.1). Following the method described in 5.1.3, the z-score is com-

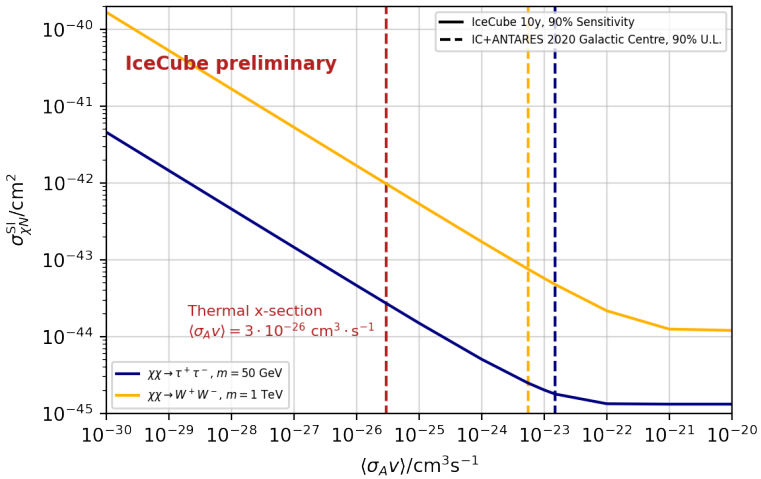

Figure 5.10 – Sensitivity value for σ_{SI} as a function of the assumption made on $\langle\sigma_{\mathrm{A}} v\rangle$ for the two LE (blue) and HE (yellow) baseline DM configurations.

puted, giving the significance of the result found. The corresponding signal fraction upper limit is computed as well. At this point, three cases are defined:

- z-score< 3: there is no evidence for signal. An upper limit is set;
- z-score< 5: evidence for signal can be claimed. The measured signal is presented;
- z-score≥ 5: a discovery can be claimed. The measured signal is presented.

In the end, we need to account for the fact that we are testing multiple DM scenarios: all the configurations with DM mass $m_\chi \leq 100$ GeV are tested with the LE selection, while the HE selection is used for all the higher masses, giving a total of 26 different DM models. Therefore, highly significant results with low p-values have a higher probability of arising simply by the fact that multiple tests are being performed in what is called the *look-elsewhere effect*. In this way, the significance of our most significant result is boosted. If all the tests are uncorrelated the result can be corrected by multiplying the obtained highest p-value by the number of tests performed (i.e. the DM configurations) so that we can write:

$$p_{\mathrm{post}} = n_{\mathrm{corr}} p_{\mathrm{pre}}, \tag{5.24}$$

where $n_{\mathrm{corr}} = 26$ for the purely uncorrelated case, while p_{pre} and p_{post} are the p-values before and after the trial correction, respectively. For this analysis, however, a correlation between the DM scenarios tested cannot be excluded. For example, the $\tau^+\tau^-$ and the W^+W^- channels have similar neutrino expectations, and all the channels are tested roughly in the same DM mass range. With a frequentist approach, we can compute the true value of this trial correction n_{corr}: the unblinding procedure is run ten thousand times on only-background pseudo-experiments; then we build the distribution of t_0 for the most significant result in each experiment and compare it to the t_0 value of the real unblinded highest significance point; the area below the trials distribution curve with a higher significance than the result gives the so-called *post-trial p-value* p_{post}, which can

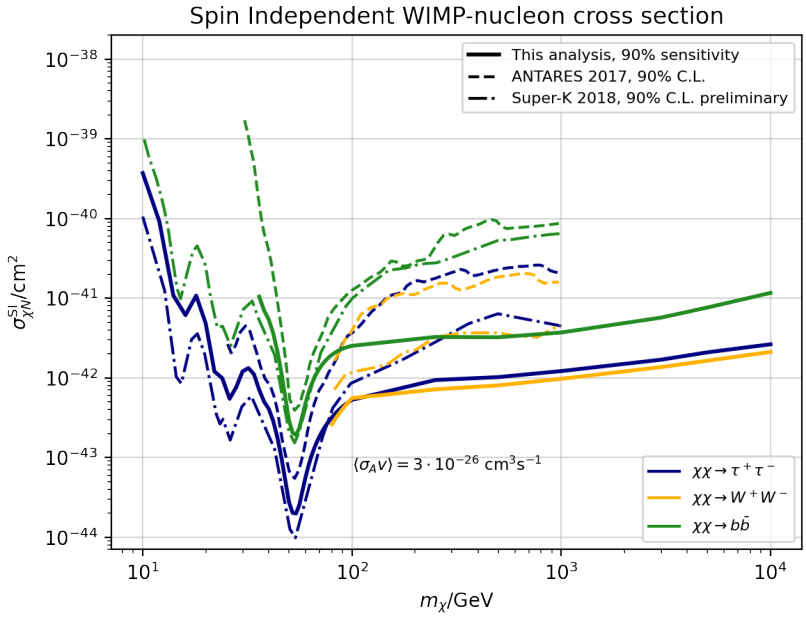

Figure 5.11 – Sensitivity on σ_{SI}, given the assumption $\langle\sigma_{\mathrm{A}} v\rangle = 3\times10^{-26}$ cm^3s^{-1}. ANTARES [40] and Super-Kamiokande [110] limits are included for comparison.

be converted in a z-score via (5.13). The value of n_{corr} can be obtained simply using equation (5.24).

CHAPTER 6

FINAL RESULTS

And if you listen very hard
The tune will come to you at last

The final chapter of this work presents the results obtained in the search for dark matter from the centre of the Earth with IceCube. Unblinded data could, at this point, be observed and analysed with the method described in chapter 5. A series of checks helped to guarantee the reliability of the results obtained. An analysis of the systematic effects has been performed, from which the final results could be obtained. In 6.1, a first overview of the results will be given, including the presentation of the unblinded IceCube data. The sanity checks and systematic variation studies will be presented in 6.2, along with the trial correction study, already mentioned in 5.4. The final results will be presented in 6.3.

6.1 Overview

6.1.1 The unblinded data

IceCube data from May 2011 to May 2020 have been processed with the event selection presented in chapter 4. The burn sample runs have been omitted from the selection, giving a total unblinded livetime $t_{\mathrm{livetime}} = 3265.88$ d $= 8.95$ y. Two final distributions have been obtained for LE and HE, respectively. The LE selection contains 1069 events, while the corresponding HE data distribution consists of 7414 events. The LE and HE distributions are shown in fig. 6.1.

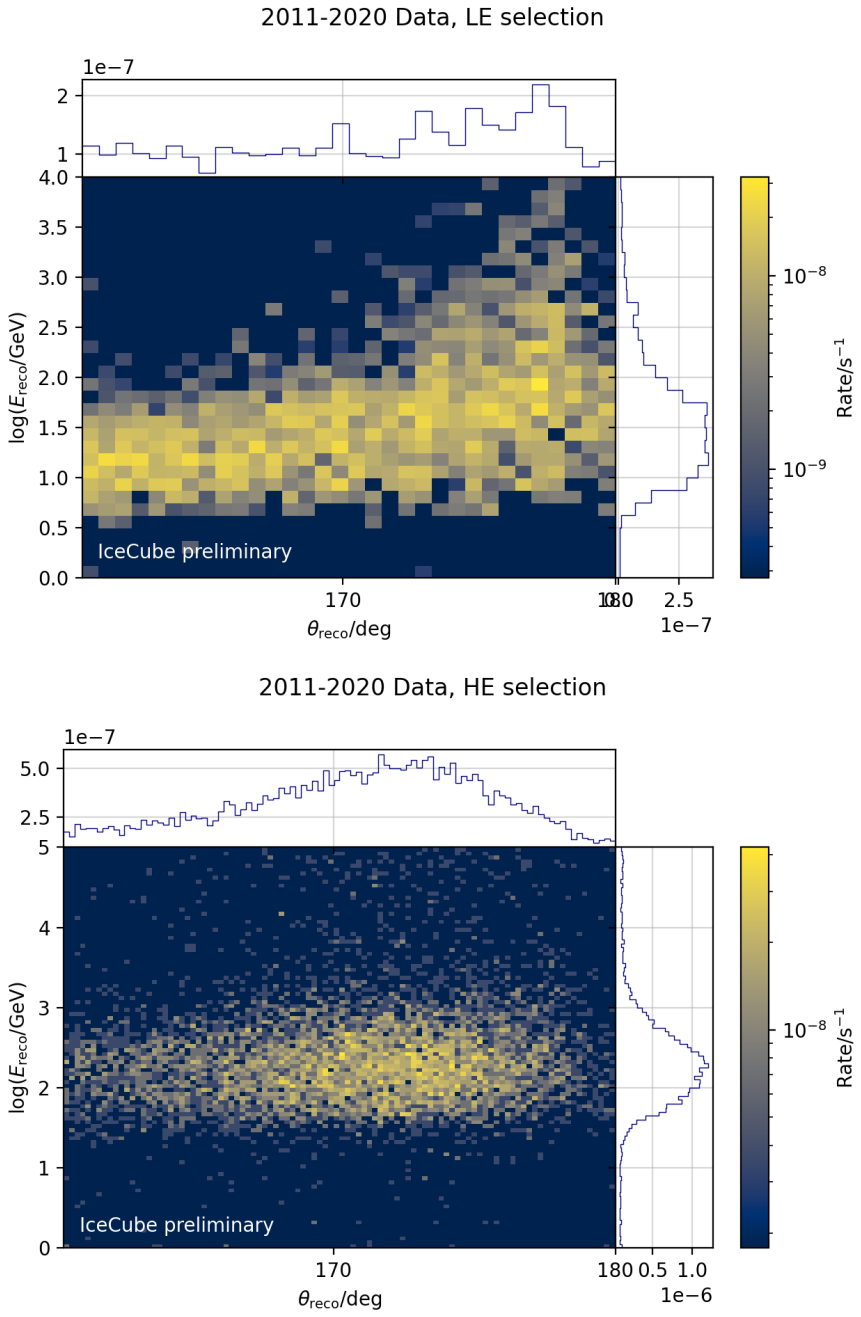

Figure 6.1 – LE (top) and HE (bottom) unblinded data distribution of the two observable parameters, the reconstructed zenith angle θ_{reco} and the reconstructed energy logarithm $\log E_{\mathrm{reco}}$.

6.1.2 Unblinding

The data unblinding has been performed following the process described in 5.4. Each DM scenario (mass and channel) has been unblinded once, depending on which of the selections (LE or HE) gives the best sensitivity at a certain mass. Sensitivities (see 5.3) indicate that the LE analysis is to be performed for masses up to 100 GeV, while the HE analysis will be performed on DM scenarios with mass above 100 GeV. The results indicate a slight excess around 100 GeV with significance around 2σ. For the $b\bar{b}$ channel, the excess is shifted towards higher energies because the energy spectrum is softer for this channel. The highest significance is 2.01σ, marked at the HE 250 GeV mass point for the $b\bar{b}$ channel. The highest LE significance is 1.99σ for $m_\chi = 100$ GeV for the $\tau^+\tau^-$ channel. No evidence for dark matter has been found, and upper limits have been computed as described in 5.3. Table 6.1 summarises all the results including the sensitivity result $\langle N_{\rm sig}^{90\%\rm CL}\rangle$, the best-fit on the unblinded data $\hat{N}_{\rm sig}$, the significance of the best-fit result in terms of z-score and the upper limit $N_{\rm sig}^{90\%\rm CL}$ set at 90% confidence level. These results do not include systematic corrections yet. The final version of the results will be given in 6.3. Figure 6.2 shows the upper limits in terms of volumetric flux, including the 1σ and 2σ bands from the sensitivities.

6.2 Post-Unblinding

6.2.1 Sanity checks

I performed some tests to assess the correctness of the results obtained. First of all, I verified that the overall MC distributions obtained with the normalisation parameters from the best fit values are in good agreement with the unblinded data distributions. To ensure the latter, I performed a chi-square agreement test between the two distributions aforementioned. Figures 6.3-6.6 show the test results, for the LE and HE analyses, for two particular cases: one where the best fit found no signal and the one where the significance of the fit signal fraction is the highest. For the same scenarios aforementioned, the distributions of the test-statistic from the ten-thousand pseudo-experiments are shown in comparison with the analytical test-statistic distribution defined in (5.10) and including the unblinded test-statistic value. As already mentioned in 5.3, for all the cases this correspondence is verified. Figures 6.7 and 6.8 show these distributions for the same cases as the previous figures. Complementary figures to the one shown in this paragraph can be found in appendix A.

A manual scan of the likelihood space allowed for verification that the minimiser is able to converge to the actual global minima of the likelihood. Since the likelihood space depends on multiple parameters, to keep a readable format I performed the scan over two of the parameters while fixing all the other parameters at the best-fit values, so that 2D likelihood plots could be produced. The scan shown in figure 6.9 for the $\tau^+\tau^-$ annihilation channel is performed in the ξ-n_1 space. The choice of the parameter n_1 is motivated by the fact that it is the one linked to the atmospheric neutrino contribution (as indicated in 5.1.1) which is the most relevant background component, and the parameter which links the NuGen and GENIE separated contributions. The plots for the other channels are included in appendix A. The plots show how the likelihood minimisation worked correctly for every DM configuration.

Mass/GeV	Selection	Channel	$\langle N_{\rm sig}^{90\%\rm CL}\rangle$	$\hat{N}_{\rm sig}$	$\hat{N}_{\rm atmo}$	$\hat{N}_{\mu}$	$\hat{N}_{\rm astro}$	z-score	$N_{\rm sig}^{90\%\rm CL}$
20	LE	$\tau^+\tau^-$	52.16	0.00	1034.29	33.83	0.97	0.00	40.71
35	LE	$\tau^+\tau^-$	47.22	26.33	1009.94	31.86	0.97	0.76	84.94
		$b\bar{b}$	38.44	0.00	1034.29	33.83	0.97	0.00	31.26
50	LE	$\tau^+\tau^-$	42.98	39.73	996.49	31.91	0.97	1.20	96.42
		$b\bar{b}$	47.47	15.42	1020.46	32.24	0.97	0.45	74.17
100	LE	$\tau^+\tau^-$	37.42	35.33	997.99	34.80	0.98	1.99	85.01
		W^+W^-	35.05	12.49	1021.24	34.40	0.98	0.41	64.09
		$b\bar{b}$	38.99	29.03	1004.96	34.14	0.98	0.94	82.44
250	HE	$\tau^+\tau^-$	46.76	66.54	7334.96	12.49	0.00	1.97	126.97
		W^+W^-	47.10	40.75	7361.27	11.98	0.00	1.17	101.05
		$b\bar{b}$	42.60	59.49	7342.12	12.39	0.00	2.01	113.88
500	HE	$\tau^+\tau^-$	40.23	20.41	7381.98	11.61	0.00	0.70	72.08
		W^+W^-	39.45	0.00	7402.83	11.17	0.00	0.01	48.92
		$b\bar{b}$	41.29	48.95	7352.87	12.18	0.00	1.71	102.01
1000	HE	$\tau^+\tau^-$	34.62	0.01	7402.88	11.11	0.00	0.00	39.56
		W^+W^-	32.73	0.00	7402.86	11.14	0.00	0.00	29.64
		$b\bar{b}$	38.59	29.13	7373.06	11.81	0.00	1.09	76.92
3000	HE	$\tau^+\tau^-$	24.50	0.00	7402.86	11.13	0.00	0.00	25.24
		W^+W^-	21.79	0.00	7402.82	11.18	0.00	0.01	23.40
		$b\bar{b}$	30.62	0.00	7402.63	11.37	0.00	0.00	35.76
5000	HE	$\tau^+\tau^-$	20.70	0.00	7402.89	11.11	0.00	0.00	22.16
		W^+W^-	18.06	0.00	7402.70	11.30	0.00	0.01	21.98
		$b\bar{b}$	27.75	5.27	7397.45	11.28	0.00	0.34	37.69
10000	HE	$\tau^+\tau^-$	15.59	0.00	7402.82	11.18	0.00	0.01	18.53
		W^+W^-	13.23	0.00	7402.86	11.14	0.00	0.00	17.09
		$b\bar{b}$	22.74	0.00	7402.89	11.11	0.00	0.00	25.51

Table 6.1 – Table of unblinding results. The columns are, from left, DM mass, selection used, DM annihilation channel, median sensitivity $\langle N_{\rm sig}^{90\%CL}\rangle$, best-fit values for the number of signal $\hat{N}_{\rm sig}$, atmsopheric neutrino $\hat{N}_{\rm atmo}$, atmospheric muon $\hat{N}_{\mu}$, and astrophysical neutrino $\hat{N}_{\rm astro}$ events, significance of the results in terms of z-score, and upper limit $N_{\rm sig}^{90\%CL}$ on the number of signal events.

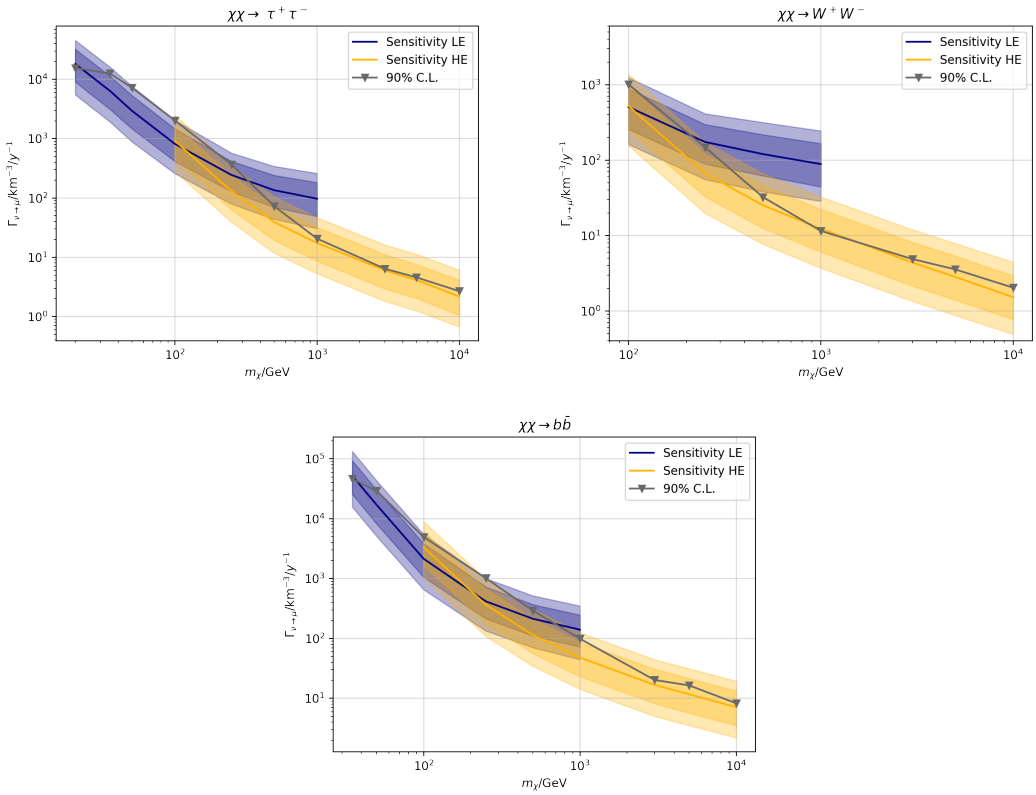

Figure 6.2 – Nominal volumetric flux upper limits (in grey) as presented in 6.1, including the 1- and 2-σ deviations of the ten-thousand pseudo-experiments upper limit distributions. Top left: $\chi\chi \to \tau^+\tau^-$ channel. Top right: $\chi\chi \to W^+W^-$ channel. Bottom: $\chi\chi \to b\bar{b}$ channel.

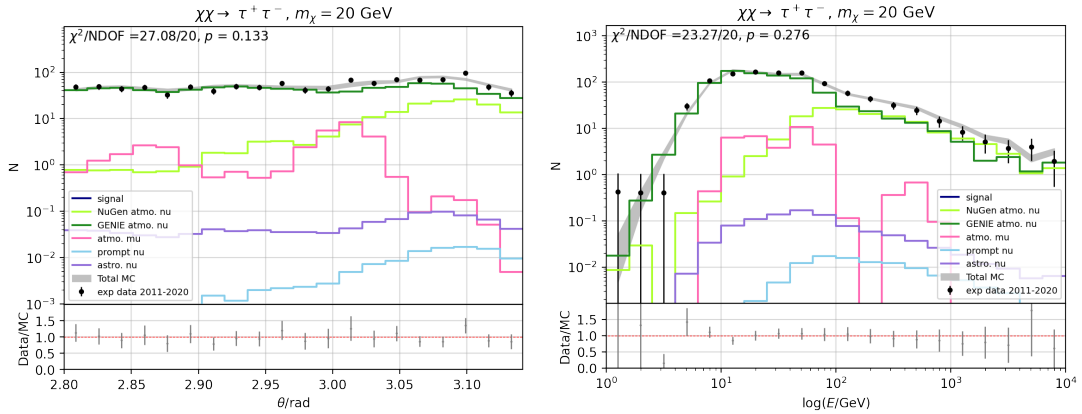

Figure 6.3 – Data/MC ratio plots, including the chi-square test results for the DM scenario $\chi\chi \to \tau^+\tau^-$, $m_\chi = 20$ GeV, where the likelihood minimisation did not fit any signal fraction.

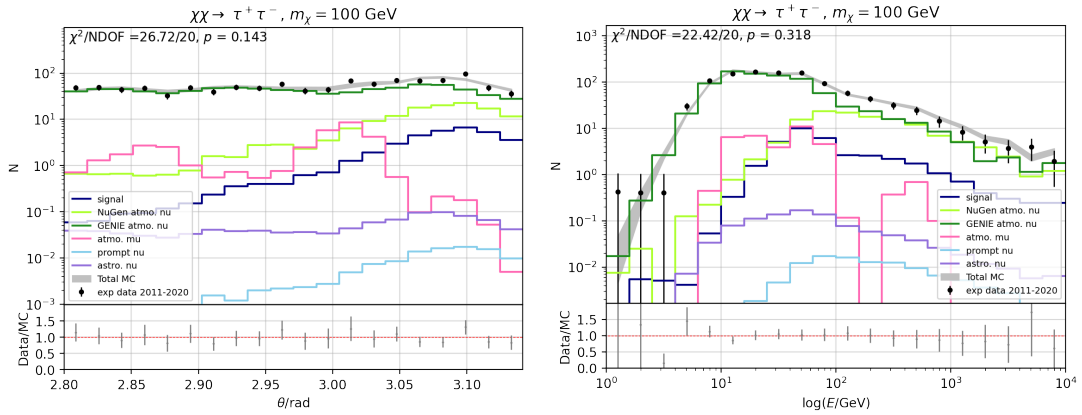

Figure 6.4 – Data/MC ratio plots, including the chi-square test results for the DM scenario $\chi\chi \to \tau^+\tau^-$, $m_\chi = 100$ GeV, where the likelihood minimisation finds a preference for a signal fraction at the level of 1.99σ.

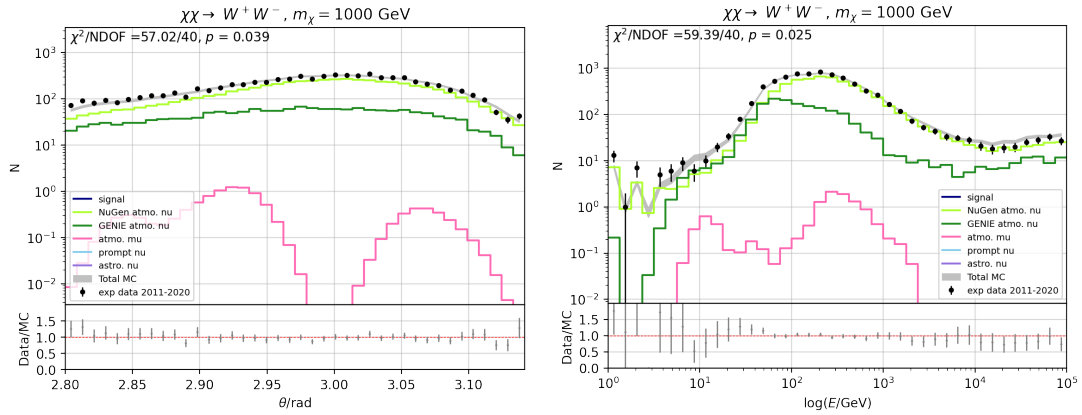

Figure 6.5 – Data/MC ratio plots, including the chi-square test results for the DM scenario $\chi\chi \to W^+W^-$, $m_\chi = 1$ TeV, where the likelihood minimisation did not fit any signal fraction.

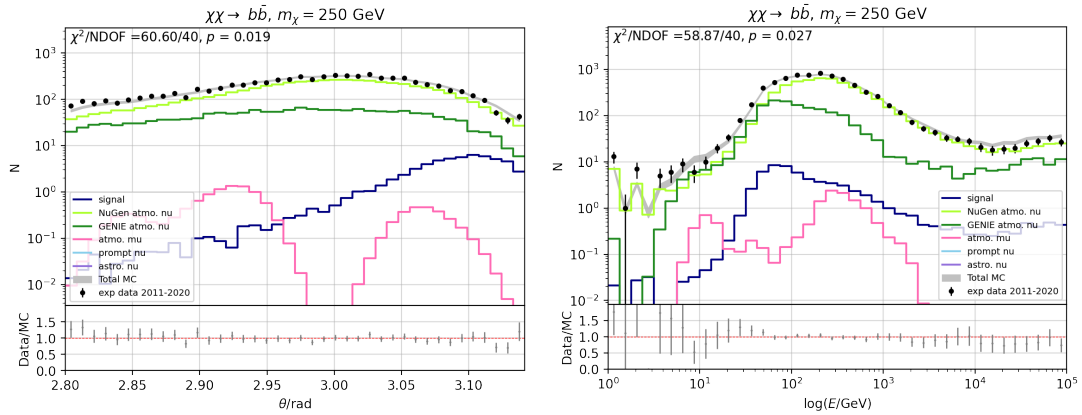

Figure 6.6 – Data/MC ratio plots, including the chi-square test results for the DM scenario $\chi\chi \to b\bar{b}$, $m_\chi = 250$ GeV, where the likelihood minimisation finds a preference for a signal fraction at the level of 2.01σ.

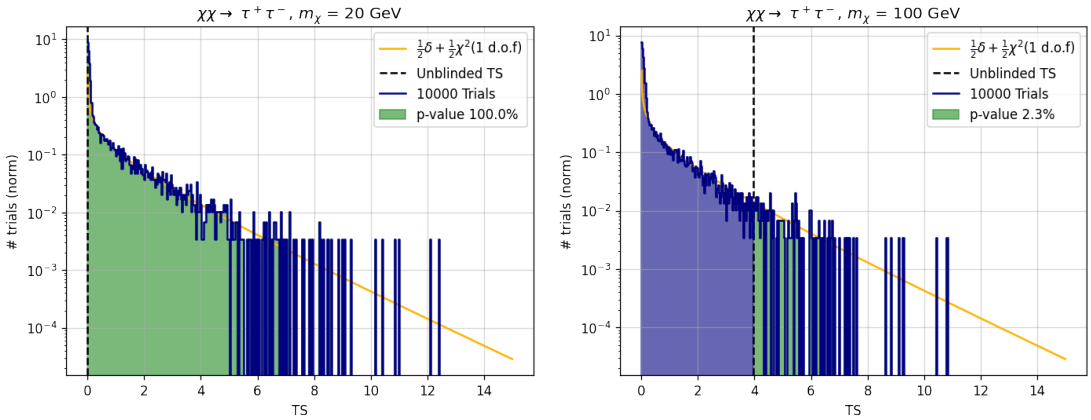

Figure 6.7 – Test statistic distributions for the LE DM scenarios $\chi\chi \to \tau^+\tau^-$, $m_\chi = 20$ GeV (left) and $m_\chi = 100$ GeV (right). The left plot shows one case where the likelihood minimisation did not fit any signal, while the right plot shows the case where the likelihood minimisation finds the highest significance result for the LE selection, at the level of 1.99σ.

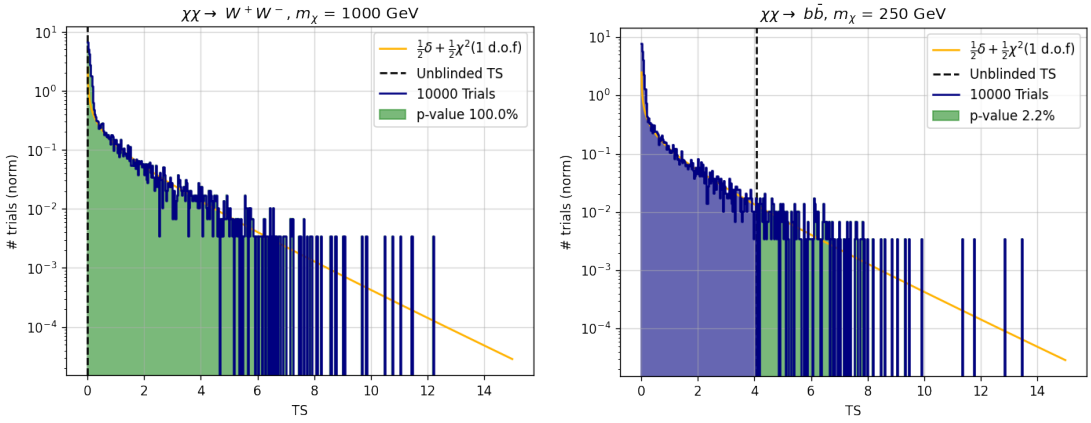

Figure 6.8 – Test statistic distributions for the HE DM scenarios $\chi\chi \to b\bar{b}$, $m_\chi = 250$ GeV (left) and $\chi\chi \to W^+W^-$, $m_\chi = 1$ TeV (right). The left plot shows one case where the likelihood minimisation did not fit any signal, while the right plot shows the case where the likelihood minimisation finds the highest significance result for the HE selection, at the level of 2.01σ.

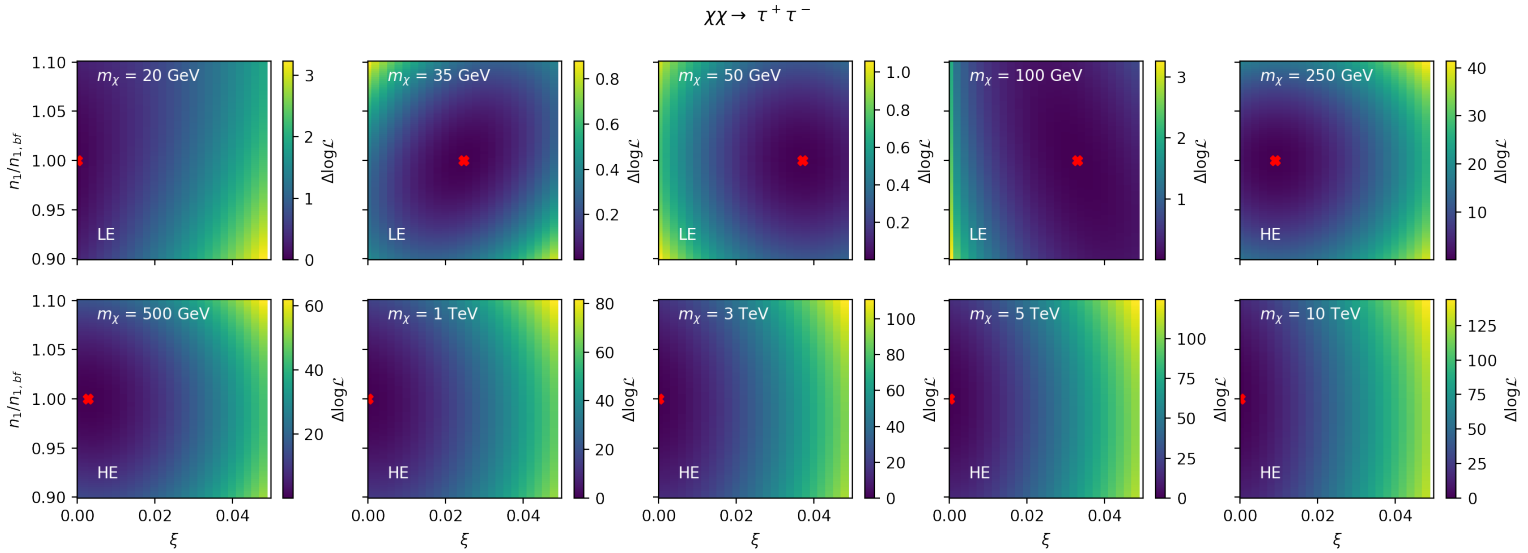

Figure 6.9 – Likelihood ξ-n_1 space scan for the $\tau^+\tau^-$ annihilation channel. The best-fit point obtained using the minimisation algorithm, marked with a red cross, is at the minimum likelihood for every DM scenario.

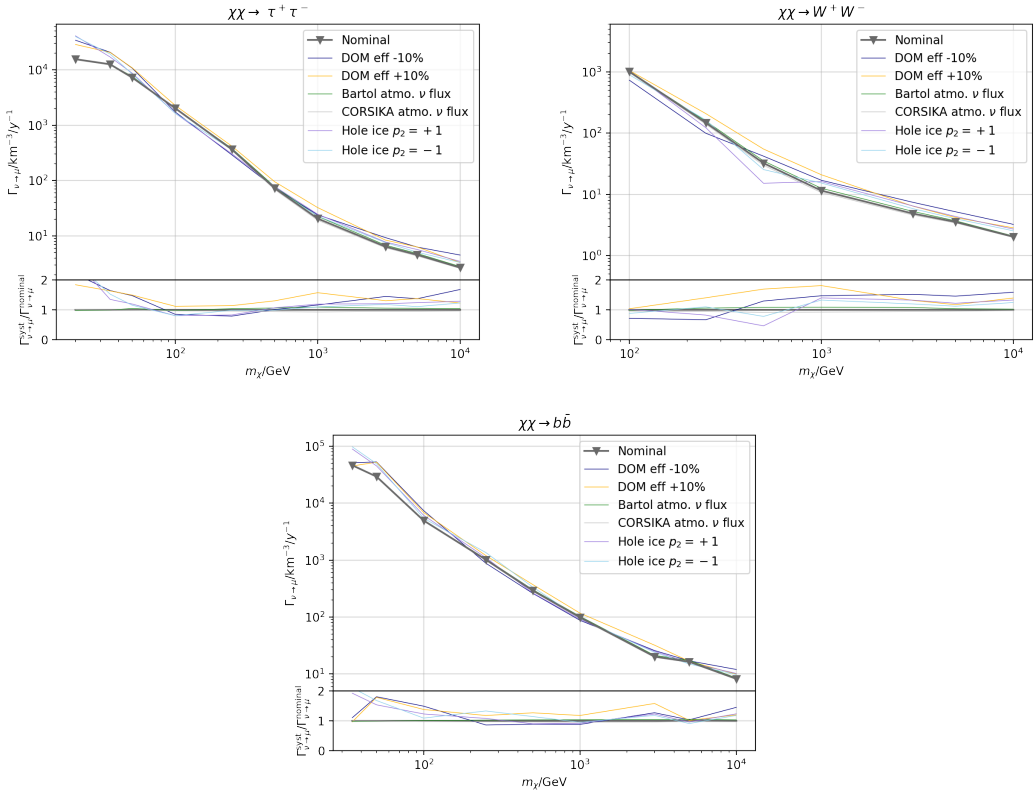

Figure 6.10 – Nominal volumetric flux upper limits (in grey) as presented in 6.1. Systematic variation limits are included for comparison with thinner, coloured lines. Top left: $\chi\chi \to \tau^+\tau^-$ channel. Top right: $\chi\chi \to W^+W^-$ channel. Bottom: $\chi\chi \to b\bar{b}$ channel.

6.2.2 Systematics

In this context, systematic variations presented in 5.2 were studied. MC distributions including one of the systematic effects were set to compose the PDF against which data should be tested, repeating the unblinding procedure for each systematic. Upper limits obtained with systematic variations are generally close to the nominal ones, as shown in figure 6.10. The value of the found best-fit likelihood is an indicator of how well the fit parameters can describe the real data. The systematic variation results giving the minimum likelihood among all the variations, including the nominal set, is hence chosen as the final result of this work. This concept can be resumed by the formula:

$$-\log \mathcal{L}_{\text{final}} = \min(-\log \mathcal{L}_{\text{nominal}}, -\log \mathcal{L}_{s1}, -\log \mathcal{L}_{s2}, ...), \tag{6.1}$$

where $\mathcal{L}_{si}$ corresponds to the best-fit likelihood value obtained applying the systematic variation i.

Figure 6.11 shows, for the $\tau^+\tau^-$ channel, the 1D likelihood scans obtained by fixing all the nuisance parameters to the best-fit values and varying only the signal parameter ξ. The plots in figure 6.11 include the best-fit likelihood values obtained applying the

different systematic variations. A lower best-fit likelihood value indicates a combination of best-fit parameter values which describes better the observed data. The same figure for the other channels is included in appendix A. These plots show as for the LE selection, where the number of events is lower and the statistical fluctuations more relevant, the systematic variations have a smaller impact compared to the same plots for the HE selection, where the number of events is bigger and the impact of systematics is more visible.

The *CORSIKA* systematic variation (see 5.2.3) is consistently the one giving the best likelihood for every DM scenario, both for LE and HE masses. Therefore, the results obtained with this variation are the corrected final results I will present in 6.3.

6.2.3 Trial correction

As explained in 5.4, the last step of the post-unblinding phase is the trial correction. The calculations here are based on the best systematic variation case, where the most significant result is found at $m_\chi = 250$ GeV, having a test-statistic $t_0 = 3.76$ which gives a pre-trial p-value of $p_{\rm pre} = 0.026$.

The unblinding procedure was performed on ten thousand only-background pseudo-experiments to build the distribution of the highest t_0 values. Figure 6.12 shows this distribution along with the value $t_0 = 3.76$ found in the real unblinding. The area below the distribution curve for $t_0 > 3.76$ is computed, giving $p_{\rm post} = 0.198$. From equation (5.24) we obtain $n_{\rm corr} = 7.62$. This result can be used to correct the significance of the final results.

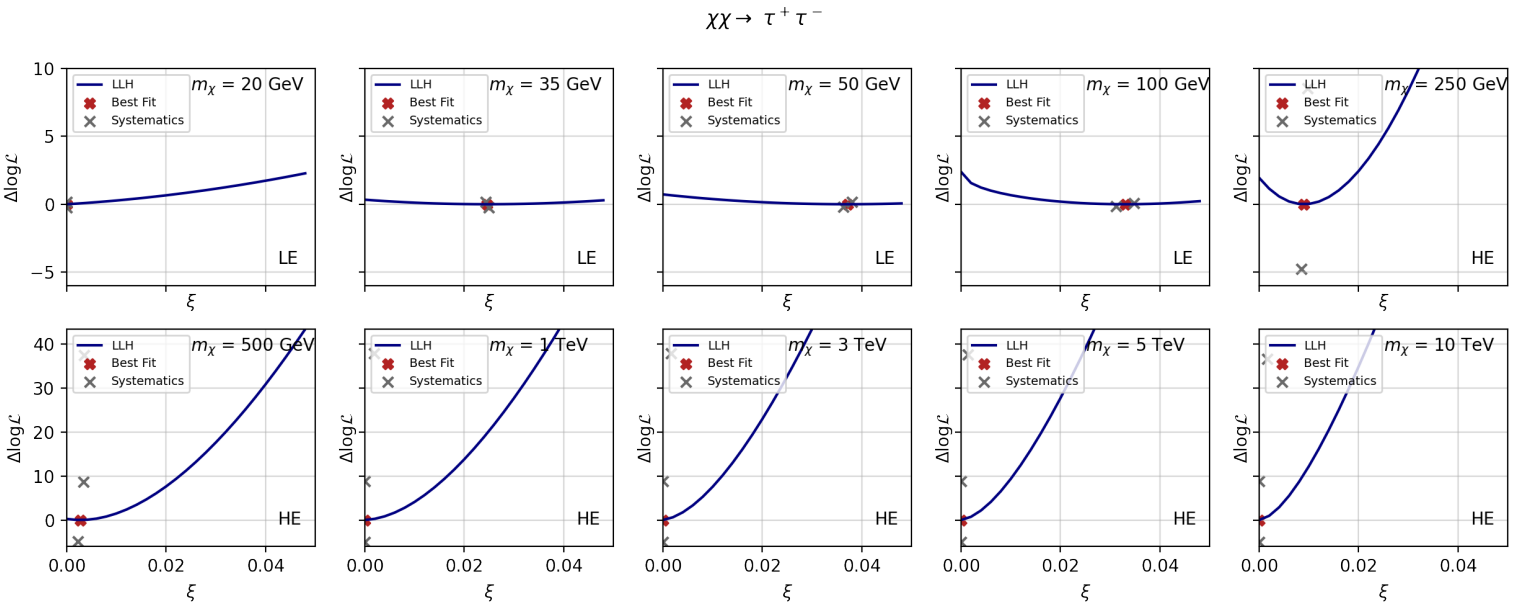

Figure 6.11 – Nominal likelihood 1D ξ space scan for the $\tau^+\tau^-$ annihilation channel. The nominal best-fit point is marked with a red cross. Grey crosses mark the best-fit likelihood minima obtained with systematic variations.

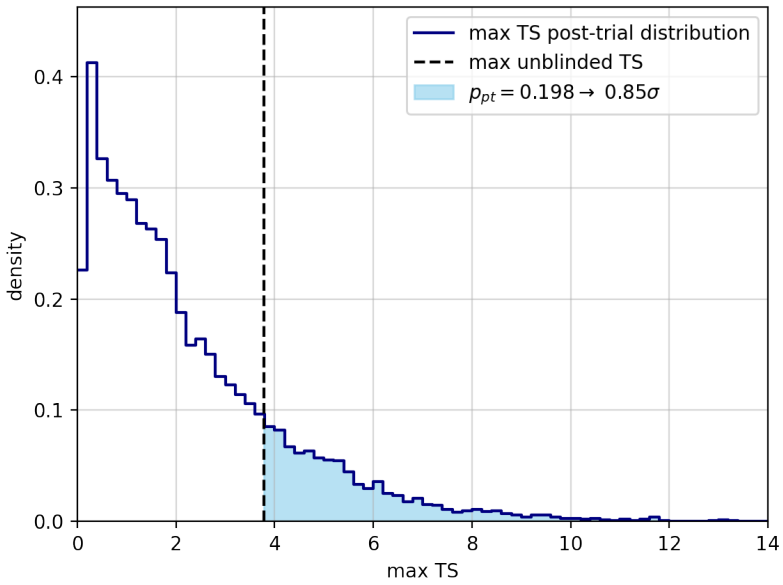

Figure 6.12 – Post-trial test-statistic distribution produced as explained in 6.2.3. The unblinded maximum value is highlighted with a vertical line. The area giving p_{post} is coloured in blue.

6.3 Summary

After all the steps described in the previous sections of this chapter, we can, at last, determine the final results of this analysis. A systematic correction has been applied, choosing to adjust the limit values and the significance with the results given by the systematic variation with the best likelihood. No evidence of dark matter was found and upper limits were set. The most significant points are at $\tau^+\tau^-$, $m_\chi = 100$ GeV and $b\bar{b}$, $m_\chi = 250$ GeV for LE and HE, respectively. These two scenarios have an equal pre-trial significance of 1.94σ. The post-trial corrected significance of this analysis is 0.85σ. The limits have been converted to spin-independent DM-nucleon cross-section and EFT values following the theories presented in 1.5.4 with the method described in 5.3. The final results are gathered in table 6.2. The following paragraphs contain the final plots I produced to represent the data in the table.

6.3.1 Annihilation rate

Limits on the annihilation rate have been computed following the steps described in 5.3. It is worth noticing that these limits are independent of further assumptions, as opposed to the cross-section limits case. The limits are compared with the 1-year IceCube analysis [12] and show a larger improvement than the expectation from the simple addition of more years. The improvement is mostly ascribable to the new event selection developed, which is $\sim 90\%$ neutrino pure, and to the use of two variables, zenith angle and energy, in contrast with the only zenith angle used in the past. The limits, which are resumed in table 6.2, are shown in figures 6.13 and 6.14.

6.3.2 Cross-section

As explained in 5.3, limits on the spin-independent scattering cross-section σ_{SI} can be obtained by solving (1.37) and converting the capture rates C_{C} found via `wimpsim` [57] [76]. As stated in 5.3, the form of (1.37) implies the necessity to make an assumption on the velocity averaged annihilation cross-section $\langle \sigma_{\mathrm{A}} v \rangle$. Figures 6.15-6.17 illustrate how the σ_{SI} limits are affected by the assumption made for different dark matter masses (colored lines). The plots also show how, for a high enough annihilation cross-section, the process described by (1.31) reaches equilibrium, visible as a horizontal plateau of the lines. The relation between the two cross-sections is due to the fact that the DM density in the centre of the Earth is not in equilibrium

Assuming the value $\langle \sigma_{\mathrm{A}} v \rangle = 3 \times 10^{-26}$ cm^{3}s (see 5.3), we can compute the final limits on the spin-independent scattering cross-section σ_{SI}. The results are presented in table 6.2 and figure 6.18 and represent the world best limits for searches from the centre of the Earth at $m_\chi > 100$ GeV. Below 100 GeV the results are competitive with the other neutrino detectors.

Mass/GeV	Analysis	Channel	$\hat{N}_{\rm sig}$	σ	$N_{\rm sig}^{90\%\rm CL}$	$\Gamma_{\rm A}/{\rm s}^{-1}$	$\sigma_{\rm SI}/{\rm cm}^2$
20	LE	$\tau^+\tau^-$	0.00	0.00	41.41	$1.02 \cdot 10^{14}$	$4.46 \cdot 10^{-42}$
35	LE	$\tau^+\tau^-$	26.62	0.77	85.10	$4.83 \cdot 10^{13}$	$1.20 \cdot 10^{-42}$
		$b\bar{b}$	0.00	0.00	31.51	$3.13 \cdot 10^{15}$	$1.01 \cdot 10^{-41}$
50	LE	$\tau^+\tau^-$	38.86	1.18	95.79	$2.32 \cdot 10^{13}$	$1.05 \cdot 10^{-42}$
		$b\bar{b}$	15.96	0.46	74.30	$1.38 \cdot 10^{15}$	$7.18 \cdot 10^{-42}$
100	LE	$\tau^+\tau^-$	33.27	1.94	82.49	$5.11 \cdot 10^{12}$	$6.17 \cdot 10^{-43}$
		W^+W^-	9.69	0.32	61.59	$4.48 \cdot 10^{12}$	$3.63 \cdot 10^{-43}$
		$b\bar{b}$	27.62	0.90	81.10	$9.93 \cdot 10^{13}$	$5.86 \cdot 10^{-42}$
250	HE	$\tau^+\tau^-$	62.41	1.85	122.38	$6.10 \cdot 10^{11}$	$9.21 \cdot 10^{-43}$
		W^+W^-	35.53	1.03	95.70	$2.77 \cdot 10^{11}$	$4.02 \cdot 10^{-43}$
		$b\bar{b}$	56.67	1.94	110.79	$7.00 \cdot 10^{12}$	$4.17 \cdot 10^{-42}$
500	HE	$\tau^+\tau^-$	16.83	0.58	68.02	$7.21 \cdot 10^{10}$	$1.52 \cdot 10^{-42}$
		W^+W^-	0.01	0.00	45.17	$3.03 \cdot 10^{10}$	$4.41 \cdot 10^{-43}$
		$b\bar{b}$	46.25	1.63	98.75	$9.93 \cdot 10^{11}$	$2.58 \cdot 10^{-42}$
1000	HE	$\tau^+\tau^-$	0.00	0.00	36.93	$1.10 \cdot 10^{10}$	$1.75 \cdot 10^{-42}$
		W^+W^-	0.00	0.00	27.57	$5.57 \cdot 10^{09}$	$4.82 \cdot 10^{-43}$
		$b\bar{b}$	26.59	1.01	73.81	$1.80 \cdot 10^{11}$	$1.45 \cdot 10^{-42}$
3000	HE	$\tau^+\tau^-$	0.00	0.00	24.04	$1.24 \cdot 10^{09}$	$1.53 \cdot 10^{-42}$
		W^+W^-	0.00	0.00	22.13	$8.40 \cdot 10^{08}$	$5.22 \cdot 10^{-43}$
		$b\bar{b}$	0.00	0.01	34.52	$1.59 \cdot 10^{10}$	$7.51 \cdot 10^{-43}$
5000	HE	$\tau^+\tau^-$	0.00	0.00	21.09	$5.50 \cdot 10^{08}$	$1.01 \cdot 10^{-42}$
		W^+W^-	0.00	0.01	21.12	$3.90 \cdot 10^{08}$	$5.63 \cdot 10^{-43}$
		$b\bar{b}$	4.56	0.28	37.01	$9.42 \cdot 10^{09}$	$4.02 \cdot 10^{-43}$
10000	HE	$\tau^+\tau^-$	0.00	0.00	17.89	$1.74 \cdot 10^{08}$	$7.29 \cdot 10^{-43}$
		W^+W^-	0.00	0.00	16.70	$1.23 \cdot 10^{08}$	$6.05 \cdot 10^{-43}$
		$b\bar{b}$	0.00	0.01	24.81	$3.15 \cdot 10^{09}$	$2.85 \cdot 10^{-43}$

Table 6.2 – Final results table. The columns are, from left, DM mass, analysis performed, DM annihilation channel, best-fit $\hat{N}_{\rm sig}$ and significance σ, and upper limits in terms of number of events $N_{\rm sig}^{90\%CL}$, annihilation rate $\Gamma_{\rm A}$, and spin-independent DM-nucleon cross-section $\sigma_{\rm SI}$.

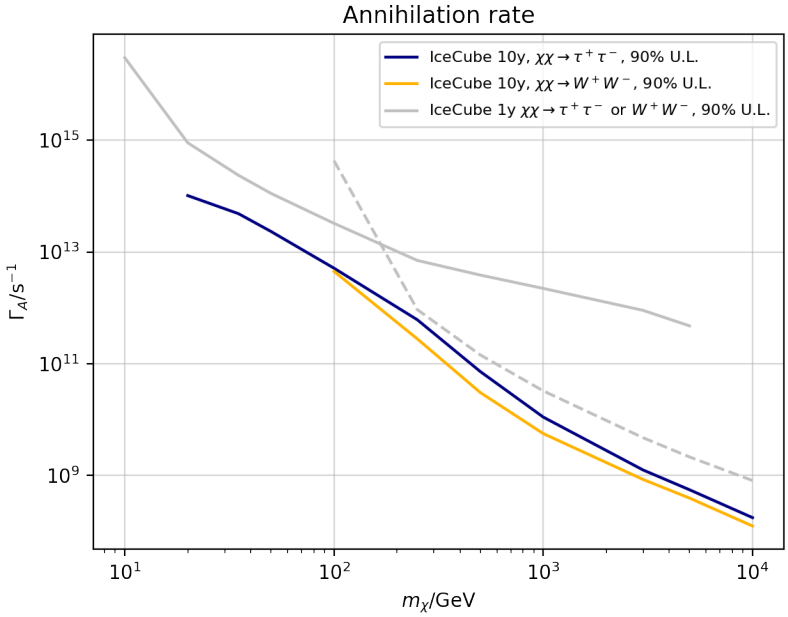

Figure 6.13 – Annihilation rate final limits for this work (blue and yellow for the $\tau^+\tau^-$ and W^+W^- channels, respectively), compared to the one-year limits from [12] (in grey).

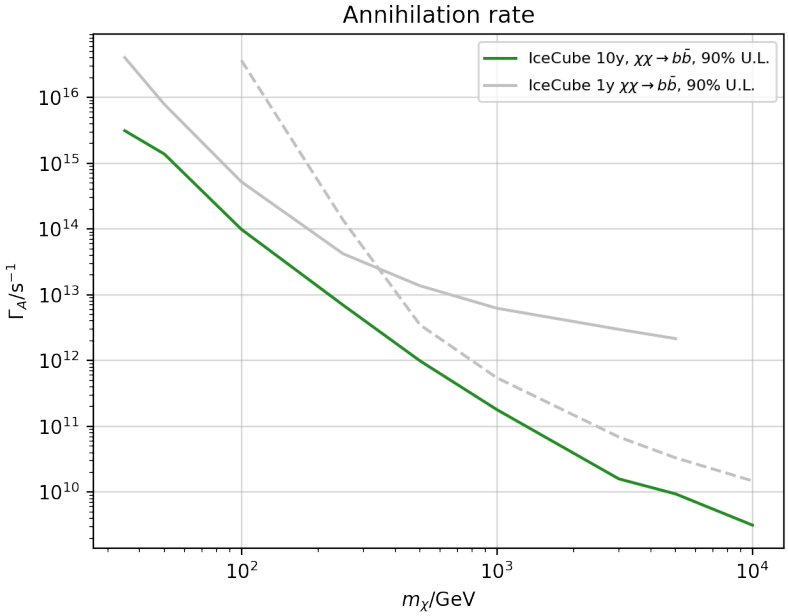

Figure 6.14 – Annihilation rate final limits for this work for the $b\bar{b}$ channel (in green), compared to the one year limits from [12] (in grey).

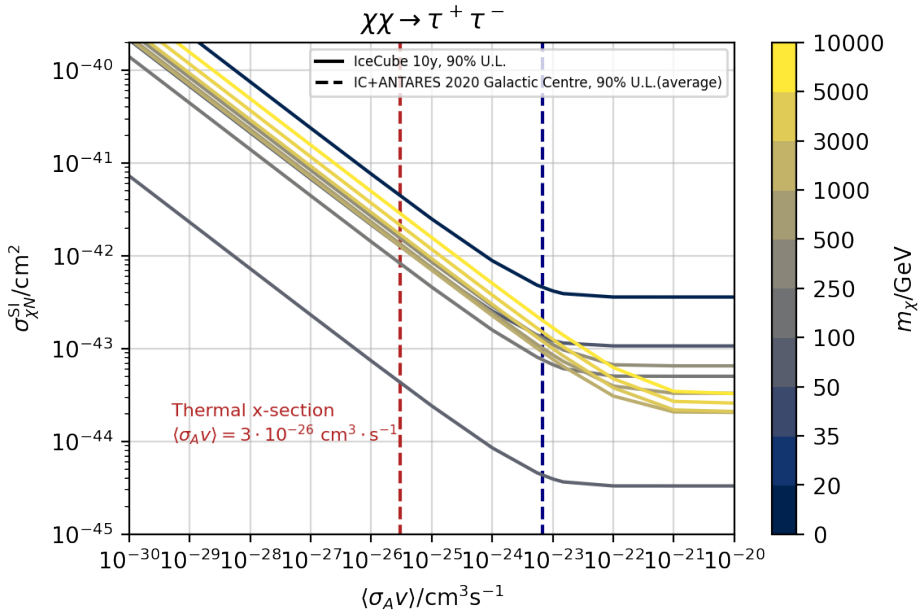

Figure 6.15 – $\tau^+\tau^-$ channel. Spin-independent scattering cross-section $\sigma_{\rm SI}$ as a function of the annihilation cross-section $\langle\sigma_{\rm A}v\rangle$. The colour gradient indicates the mass of the DM particle (blue for low mass, yellow for high mass). The vertical blue line is a reference limit from [41]. The assumption made for this work is marked by the red vertical line at $\langle\sigma_{\rm A}v\rangle = 3 \times 10^{-26}$ cm^{3}s^{-1}. The limits exclude the area above the coloured lines and to the right of the vertical blue line.

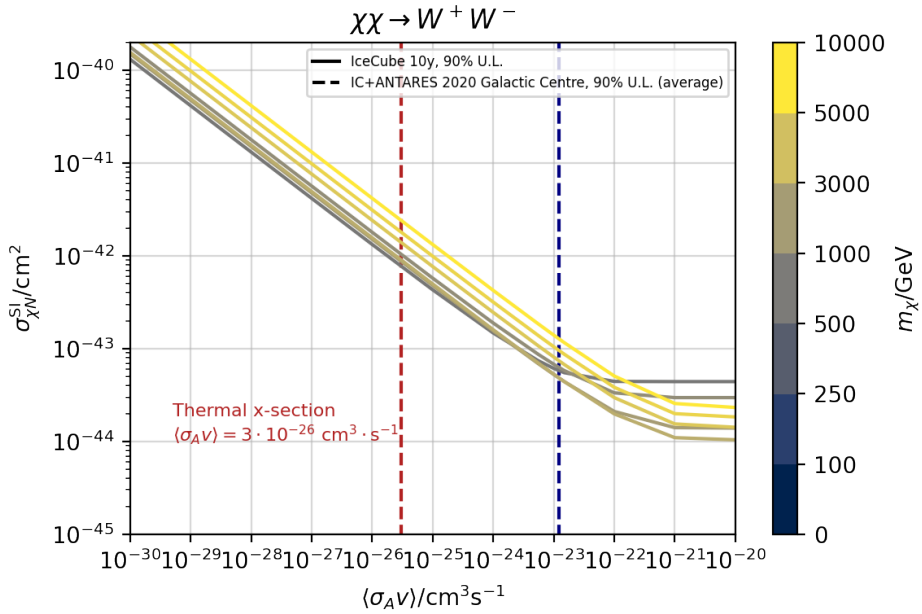

Figure 6.16 – W^+W^- channel. Spin-independent scattering cross-section σ_{SI} as a function of the annihilation cross-section $\langle\sigma_{\mathrm{A}}v\rangle$. The colour gradient indicates the mass of the DM particle (blue for low mass, yellow for high mass). The vertical blue line is a reference limit from [41]. The assumption made for this work is marked by the red vertical line at $\langle\sigma_{\mathrm{A}}v\rangle = 3 \times 10^{-26}$ cm^{3}s. The limits exclude the area above the coloured lines and to the right of the vertical blue line.

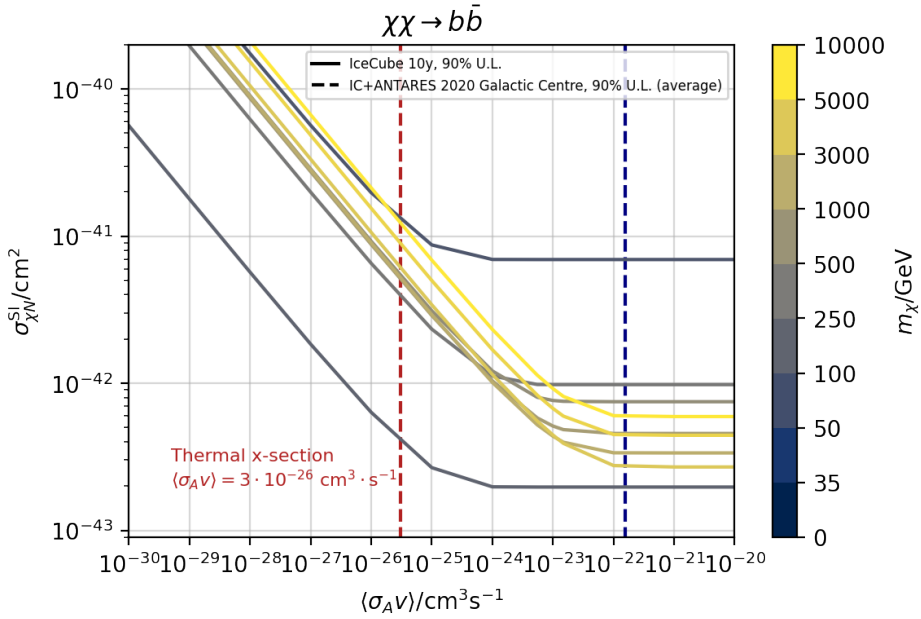

Figure 6.17 – $b\bar{b}$ channel. Spin-independent scattering cross-section σ_{SI} as a function of the annihilation cross-section $\langle\sigma_{\mathrm{A}}v\rangle$. The colour gradient indicates the mass of the DM particle (blue for low mass, yellow for high mass). The vertical blue line is a reference limit from [41]. The assumption made for this work is marked by the red vertical line at $\langle\sigma_{\mathrm{A}}v\rangle = 3 \times 10^{-26}$ cm^{3}s. The limits exclude the area above the coloured lines and to the right of the vertical blue line.

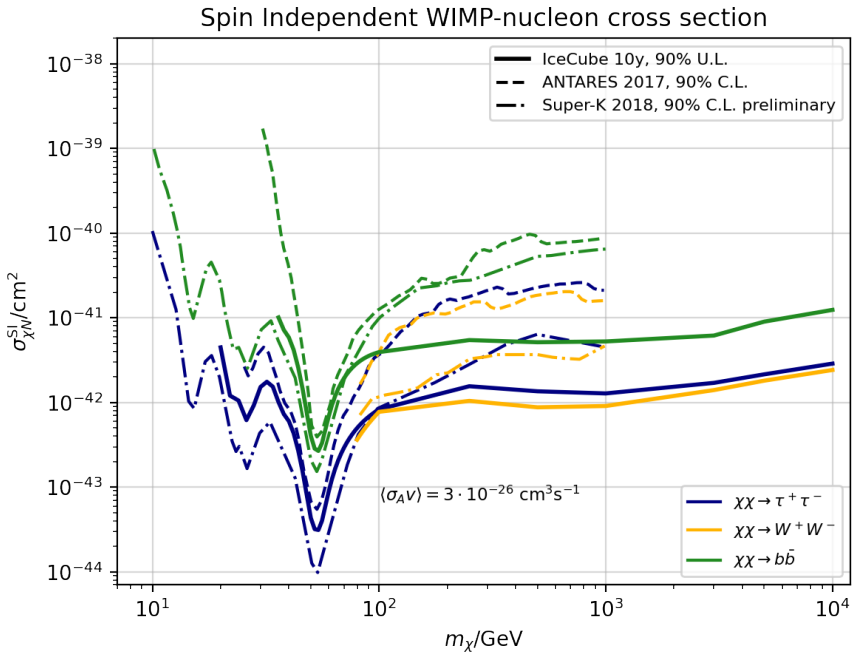

Figure 6.18 – Spin-independent scattering cross-section limits for this work. Annihilation channels are shown in blue, yellow, and green for $\tau^+\tau^-$, W^+W^-, and $b\bar{b}$, respectively. The results are compared with limits from ANTARES [40] and SuperKamiokande [110].

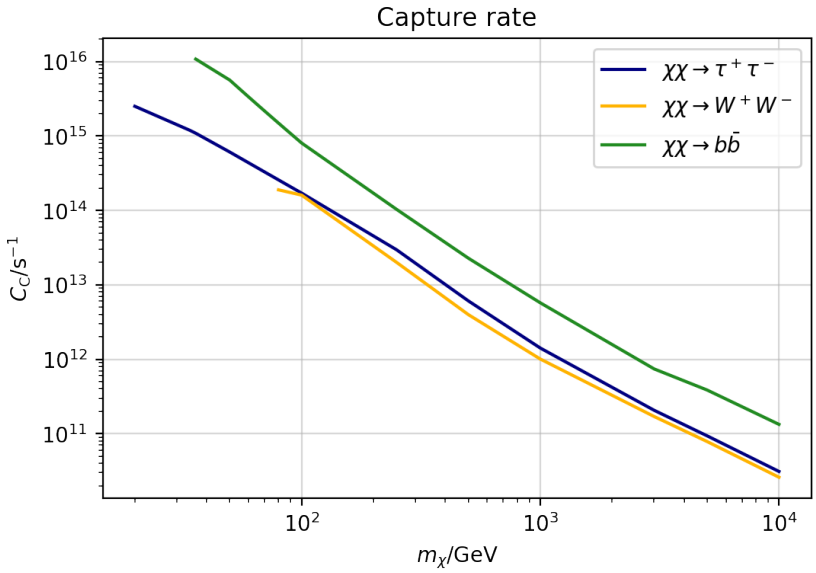

Figure 6.19 – Limits on the capture rate for the three channels $\tau^+\tau^-$ (blue), W^+W^- (yellow), and $b\bar{b}$ (green).

6.3.3 EFT coupling constants

Limits on the effective field theory coupling constants can be computed with a simple conversion of the capture rate limits [61], exploiting the proportionality of the capture rate to the coupling constants:

$$\left(c_i^{\mathrm{lim}}\right)^2 = \frac{C_{\mathrm{C}}^{\mathrm{lim}}}{C_{\mathrm{C},i}} c_0^2, \tag{6.2}$$

where $m_v = 246.2$ GeV is the electroweak scale. The parameter $c_0 = 10^{-3} m_v^{-2}$ is the common arbitrary assumption and comes from the reference cross-section value $(\mu_{\chi N}^2/m_v^4)/4\pi \sim 7 \times 10^{-45}$, though the results can be easily rescaled. $C_{\mathrm{C}}^{\mathrm{lim}}$ are the capture rate limits while $C_{\mathrm{C},i}$ is the capture rate when all the coupling constants are set to zero except the i-th one. The capture rates $C_{\mathrm{C},i}$ where presented in 1.5.4 and we use tabulated versions of the $C_{\mathrm{C},i}$ lines in [61], some of which can be found in figure (1.35).
Capture rate limits were computed in the process to find the σ_{SI} limits (see 5.3.3 for more details) presented in the previous paragraph and are shown in figure 6.19. Limits on selected coupling constants are shown in figure 6.20 and 6.21. Limits for all the constants show an improvement compared to limits computed in [61], which is expected since those limits were computed using the results from the one-year analysis [12]. The coupling constants shown here are those for which the limits are competitive with the Sun limits [123] in some parts of the mass m_χ range. Limits on other coupling constants can be found in appendix B.

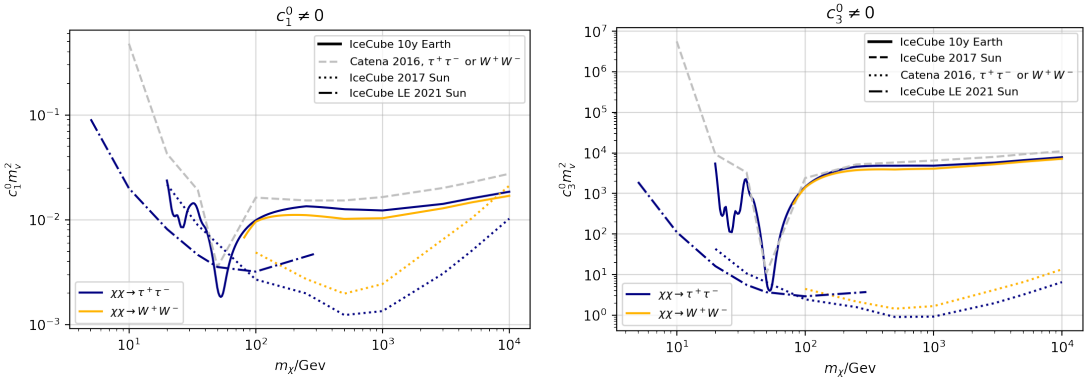

Figure 6.20 – Limits for the coupling constants c_1^0 and c_3^0. For comparison, limits from [61] and [123] are shown.

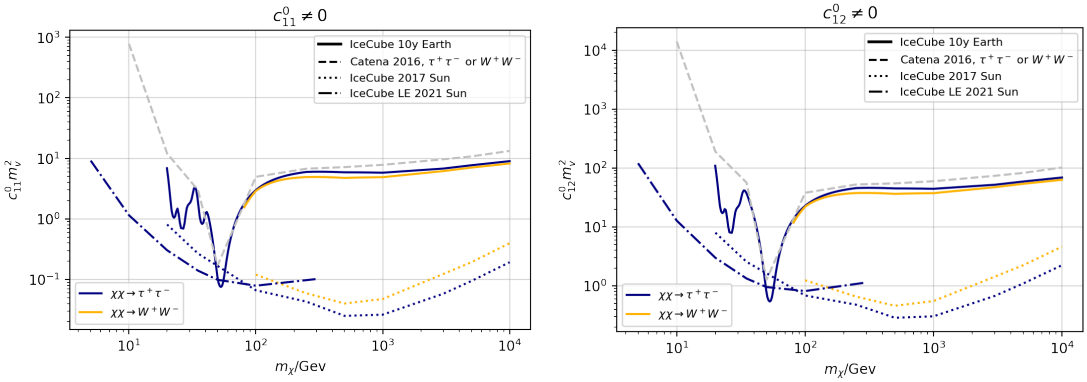

Figure 6.21 – Limits for the coupling constants c_{11}^0 and c_{12}^0. For comparison, limits from [61] and [123] are shown.

6.3.4 Results discussion

As previously mentioned, the results presented in this chapter show that this analysis reached the world's best limits for searches for dark matter from the centre of the Earth with neutrino telescopes for $m_\chi > 100$ GeV. In the LE part of the analysis, although the results for this analysis are competitive, SuperKamiokande [110] is able to set better limits. This is probably due to the denser detector unit structure of the detector, which favours the detection of low-energy events, and the use of an all-neutrino-flavours selection. Improvement of the LE energy results of this analysis can be expected with an all-flavours selection as well as with the potentialities of the upcoming IceCube Upgrade [99].

Figures 6.13 and 6.14 show the improvement of this analysis compared to the 1-year IceCube analysis [12]: while we expect an improvement of factor 3 from simply extending the old analysis to multiple years, we observe, for all masses and channels, a factor $>$3, reaching a factor $\sim$10 for the lowest and highest masses tested for all channels.

Figure 6.22 shows how this analysis' limits on the spin-independent scattering cross-section $\sigma^{\mathrm{SI}}_{\chi N}$ are compared to direct detection results. This analysis could set better limits than the crystal experiments, such as COSINE100 [25] and exclude, once again, the DAMA/LIBRA dark matter claim [53]. However, the best direct detection upper limits, from XENONIT [45], are orders of magnitude lower than this analysis. Nonetheless, we can consider the two results as complementary, as these two detection techniques test diferent regions of the local dark matter velocity distribution: direct detection experiments need high-velocity dark matter particles to scatter off nuclei and produce a detectable recoil while, for this analysis, low-velocity particles are more likely to fall in the Earth gravitational field after scattering and losing velocity (for more details see [15]).

Finally, as visible in figures 6.15-6.17, the limits from this analysis can improve by up to 2 orders of magnitude when considering annihilation enhancements (e.g. the Sommerfeld effect [73]) or other effects that could lead to an earlier equilibrium state between the capture and annihilation processes at Earth. An enghancement of the annihilation rate or the local DM density will sale accordingly limits in Earth searches, while results for the Sun [9] [66] [28] will be unaffected since equilibrium is already reached.

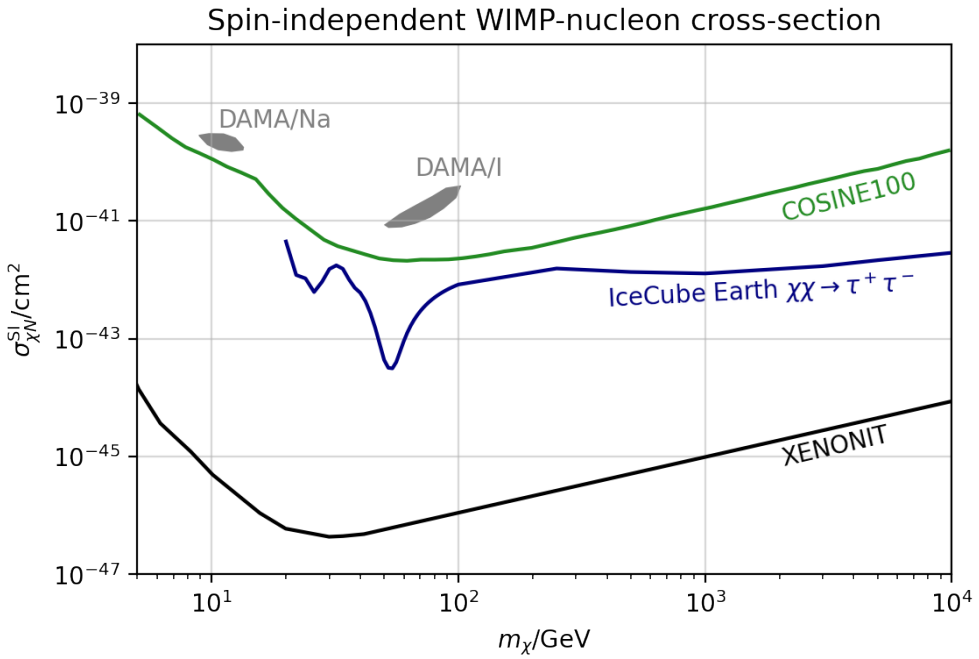

Figure 6.22 – Limits on the spin-independent scattering cross-section $\sigma^{\mathrm{SI}}_{\chi N}$ for the annihilation channel $\chi\chi \to \tau^+\tau^-$ compared to selected direct detection results from DAMA [53], COSINE100 [25] and XENONIT [45].

CONCLUSION

At the end of this work, I would like to draw some final considerations and discuss possible future developments. An indirect search for dark matter annihilation in the centre of the Earth with ten years of IceCube data has been presented, looking for a possible excess in the neutrino flux from the direction of the source. This search is part of the effort in the exploration of the dark matter possibilities with neutrino telescopes, which is complementary to other dark matter detection techniques. The Earth searches peculiarity is the non-equilibrium between the processes of capture and annihilation of dark matter, which means that the neutrino production from annihilation is not at its maximum yet, linking the final results on the dark matter-nucleon scattering cross-section to the choice of a value of the annihilation cross-section.

The peculiar position of the source required the development of a dedicated event selection based on Monte-Carlo simulations, with a burn sample of ~ 353 days of data for verification purposes. Over a dark matter mass range of 20 GeV-10 TeV, three dark matter channels were considered: $\chi\chi \to \tau^+\tau^-$, $\chi\chi \to W^+W^-$, and $\chi\chi \to b\bar{b}$. After preliminary stages mainly composed of cuts on variables to reduce the overall rates of events while saving the most possible of the signal events, the selection had to be split into a low- and a high-energy part, due to the important differences in the signal characteristics at different energies. A random forest algorithm demonstrated to be a powerful tool in discriminating the artificial background composed of atmospheric muons misreconstructed as up-going from the neutrino-induced events. The final neutrino purity achieved was of $\sim 87\%$ and $\sim 90\%$ for the low- and high-energy selections, respectively.

A statistical method was elaborated for the analysis of 2D representations of the distributions of the final selections. This is the first time this kind of analysis is performed on two variables, which were the reconstructed zenith angle θ and energy in the form $\log_{10} E$. PDFs were built on the final MonteCarlo distributions for six components: dark matter signal, low- and high-energy atmospheric neutrino background based on two different simulation generators, atmospheric muon background, prompt atmospheric neutrino background, and astrophysical neutrino background. The model was based on one signal parameter and four nuisance parameters linked to the background components and an algorithm was implemented for the minimisation of the Poisson likelihood over the parameters.

After sensitivities, computed on ten thousand pseudo-experiments, were asserted, data from ten years (minus the one-year burn sample) of IceCube were unblinded. No

significant excess was found, as the highest significance is found to be 1.94σ pre-trial and 0.85σ post-trial for the high-energy dark matter configuration $\chi\chi \to b\bar{b}$, $m_\chi = 250$ GeV. Therefore, upper limits were set, giving competitive results all over the dark matter mass range and the world's best limits for dark matter searches from the centre of the Earth for masses $m_\chi > 100$ GeV. The limits on the dark matter effective field theory coupling constants were also updated in this context, showing competitiveness in the area of the Fe resonance around ~ 50 GeV for some of the constants.

We expected an improvement on the limits from the previous search [12] with one year of IceCube data of at least a factor $\sqrt{9} = 3$ from the fact that this new analysis was performed on nine years of data. Nevertheless, we observed a bigger improvement factor over almost the whole mass range and for all the channels, indicating that the new event selection and analysis brought an enhancement of the IceCube potentialities in this kind of search. As this event selection is mostly a muon neutrino selection and compared to the result from the all-neutrino-flavours analysis from SuperKamiokande [110], further improvement in the low-energy selection mass range could be achieved by developing an all-neutrino-flavours selection.

It is important to underline how, although these results were produced based on a specific dark matter model, the limits obtained can be recast to a broad set of models which predict dark matter from the centre of the Earth. A practical example was presented with the conversion of the limits into limits on the coupling constants of the dark matter effective field theory. Some models predict an enhanced flux of dark matter from annihilation in the centre of the Earth. For example, as mentioned above, in the model analysed in this work the processes of capture and annihilation are not in equilibrium for the Earth case. The theory of the Sommerfeld effect [73] predicts a shorter equilibrium time which allows for equilibrium for the Earth at the current age.

The current limits on dark matter are shrinking more or more the phase space where dark matter could be found, encouraging the arising of a crescent number of dark matter models and the improvement of analysis techniques toward the solution of this century-old puzzle.

APPENDIX A

FURTHER UNBLINDING CHECK PLOTS

This appendix is meant to complete the set of unblinding verification plots. The 2D ξ-n_1 likelihood space scans for the W^+W^- and $b\bar{b}$ channel are shown in figure A.1 and A.2, respectively. The 1D likelihood scans on xi, including best-fit results from systematic variations, are presented in figure A.3 and A.4 for the W^+W^- and $b\bar{b}$ channel, respectively. For both the plot types and both channels, the correctness of the likelihood minimisation implementation stated in 6.2.1 is confirmed.
The test-statistic plots not shown in the main body are presented here in figures A.5-A.15 for completeness, for all the LE and HE dark matter scenarios analysed.

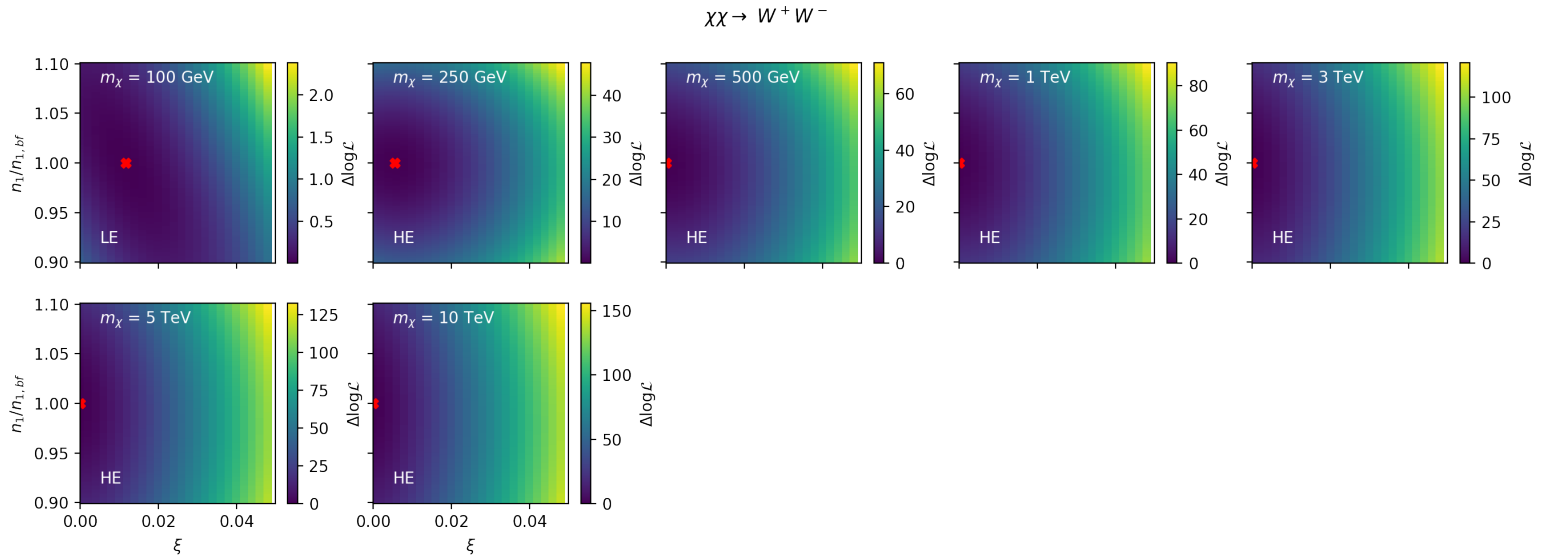

Figure A.1 – Likelihood ξ-n_1 space for the W^+W^- annihilation channel. The best-fit point obtained using the minimisation algorithm, marked with a red cross, is at the minimum likelihood for every DM scenario.

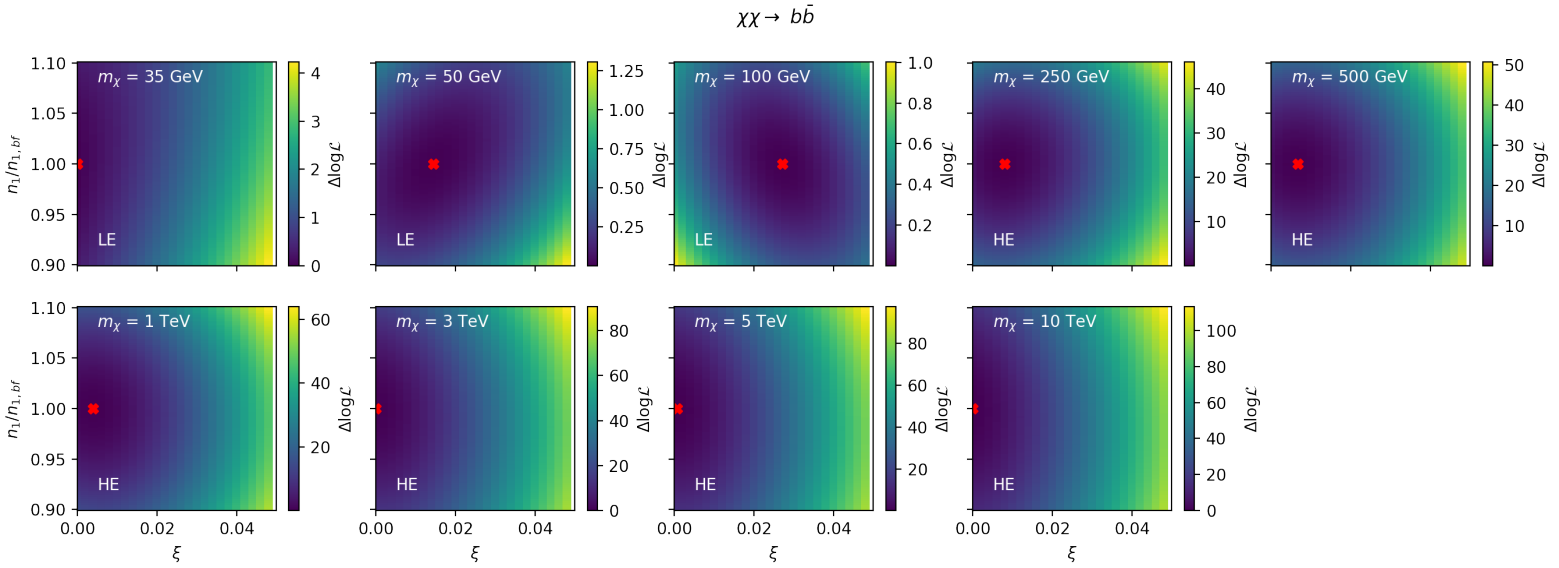

Figure A.2 – Likelihood ξ-n_1 space for the $b\bar{b}$ annihilation channel. The best-fit point obtained using the minimisation algorithm, marked with a red cross, is at the minimum likelihood for every DM scenario.

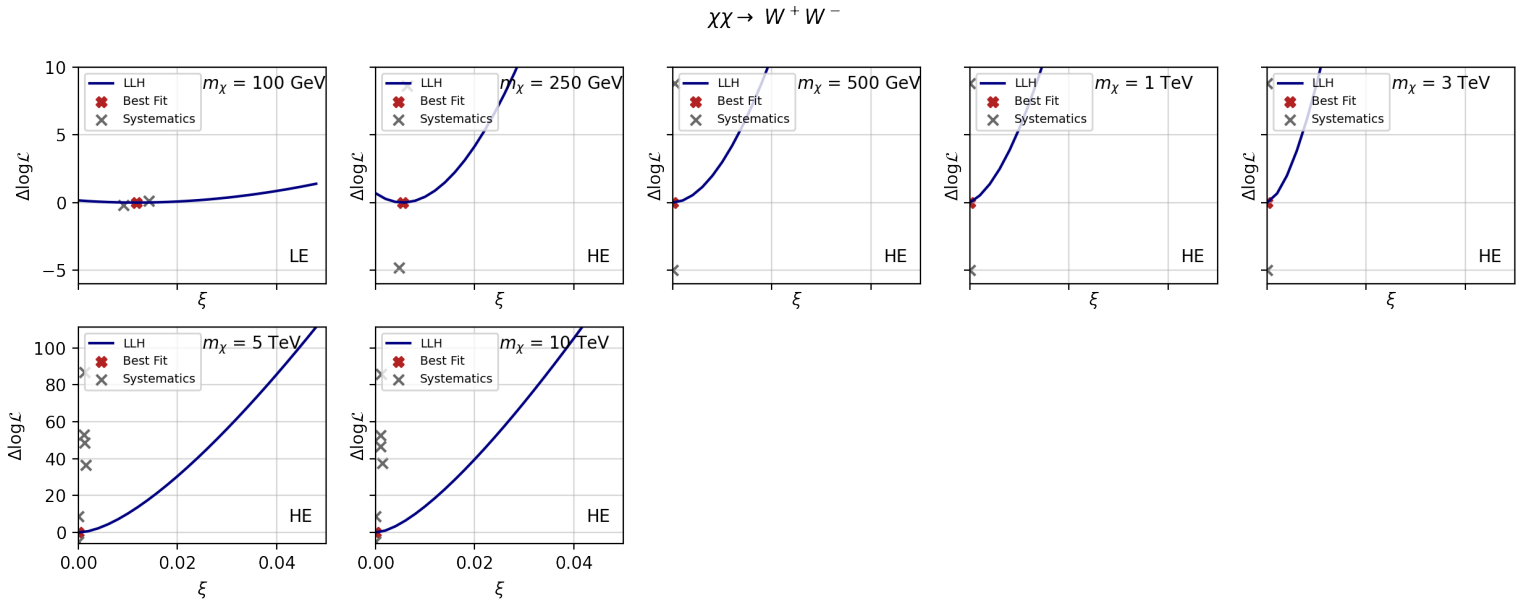

Figure A.3 – Nominal likelihood 1D ξ space scan for the W^+W^- annihilation channel. The best-fit point is marked with a red cross. Grey crosses mark the best-fit likelihood minima obtained with systematic variations.

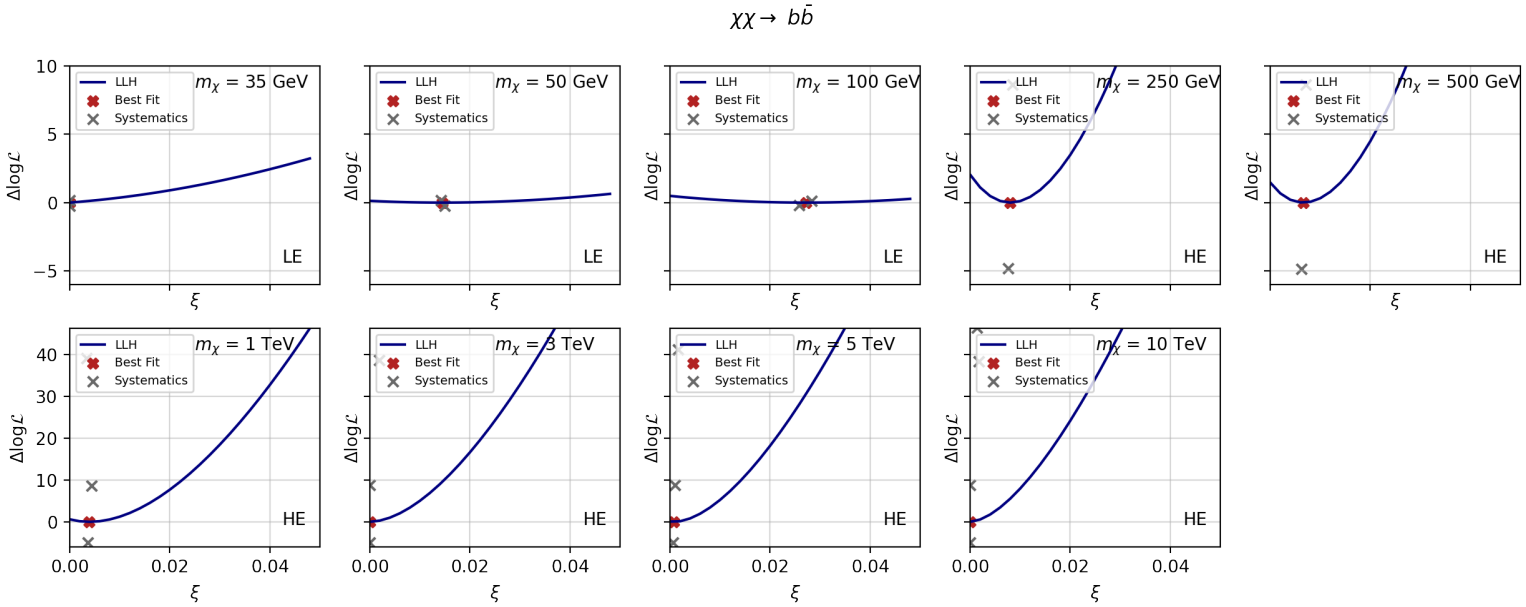

Figure A.4 – Nominal likelihood 1D ξ space scan for the $b\bar{b}$ annihilation channel. The best-fit point is marked with a red cross. Grey crosses mark the best-fit likelihood minima obtained with systematic variations.

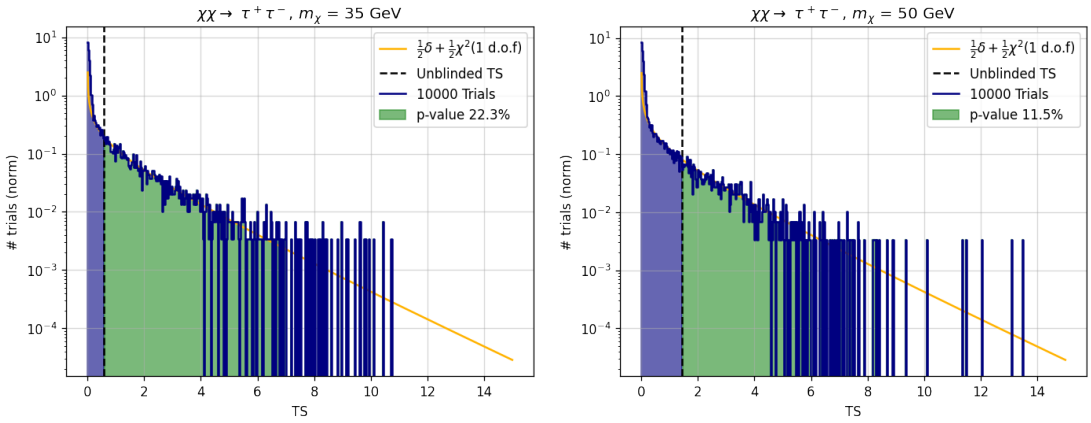

Figure A.5 – Test statistic distributions for the LE DM scenarios $\chi\chi \to \tau^+\tau^-$, $m_\chi = 35$ GeV (left) and $m_\chi = 50$ GeV (right).

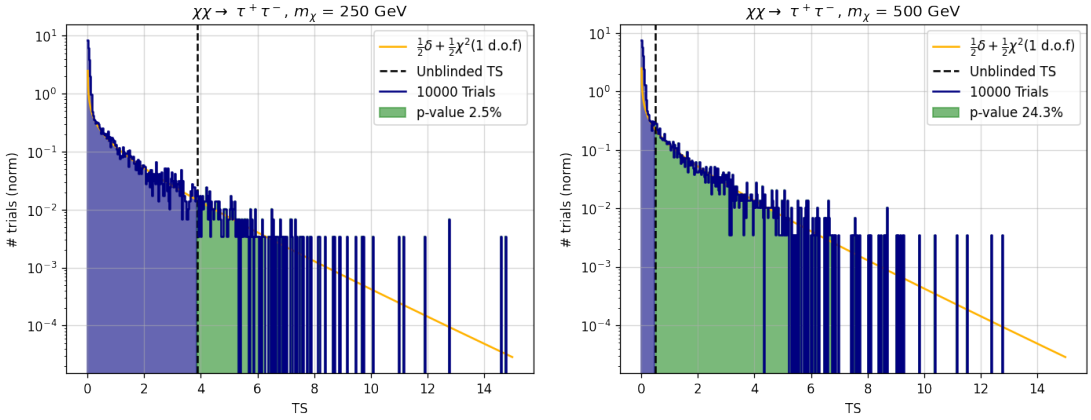

Figure A.6 – Test statistic distributions for the HE DM scenarios $\chi\chi \to \tau^+\tau^-$, $m_\chi = 250$ GeV (left) and $m_\chi = 500$ GeV (right).

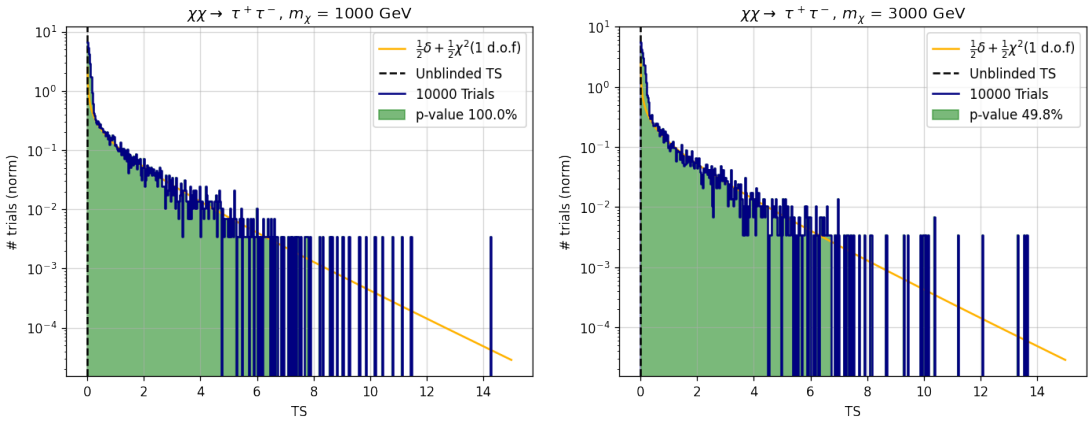

Figure A.7 – Test statistic distributions for the HE DM scenarios $\chi\chi \to \tau^+\tau^-$, $m_\chi = 1$ TeV (left) and $m_\chi = 3$ TeV (right).

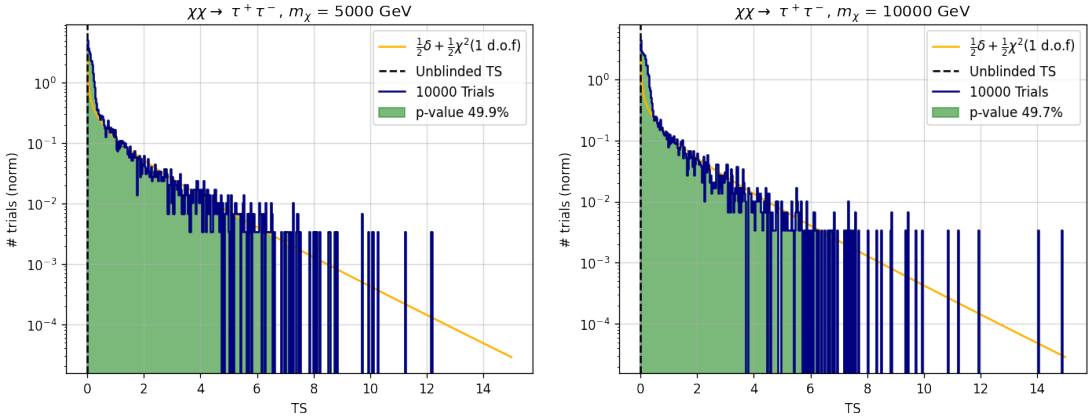

Figure A.8 – Test statistic distributions for the HE DM scenarios $\chi\chi \to \tau^+\tau^-$, $m_\chi = 5$ TeV (left) and $m_\chi = 10$ TeV (right).

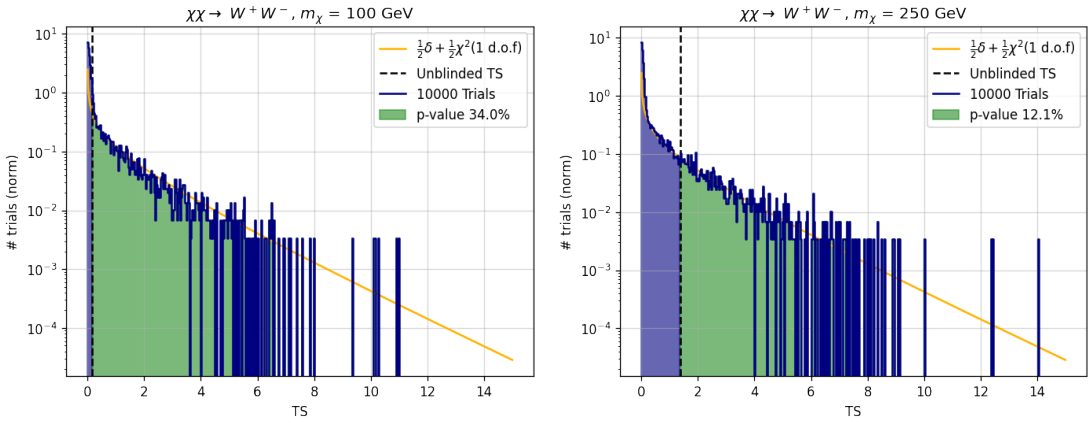

Figure A.9 – Test statistic distributions for the LE DM scenario $\chi\chi \to W^+W^-$, $m_\chi = 100$ GeV (left) and HE scenario $\chi\chi \to W^+W^-$, $m_\chi = 250$ GeV (right).

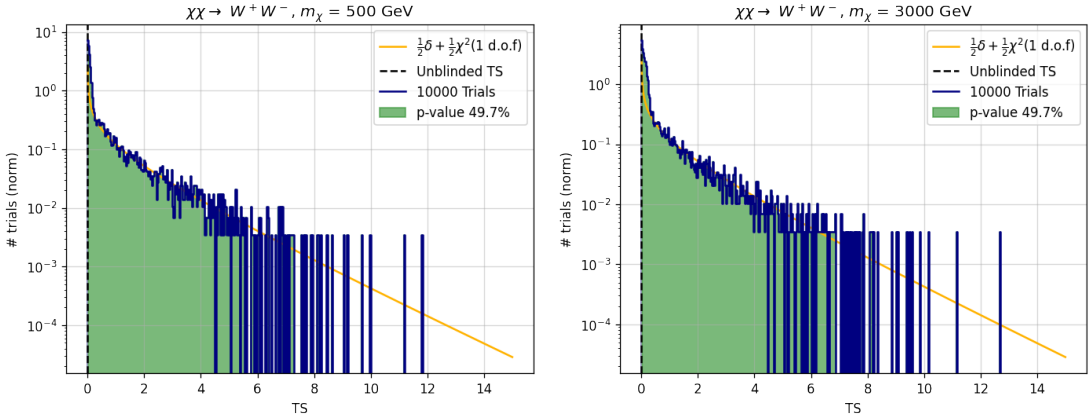

Figure A.10 – Test statistic distributions for the HE DM scenarios $\chi\chi \to W^+W^-$, $m_\chi = 500$ GeV (left) and $m_\chi = 3$ TeV (right).

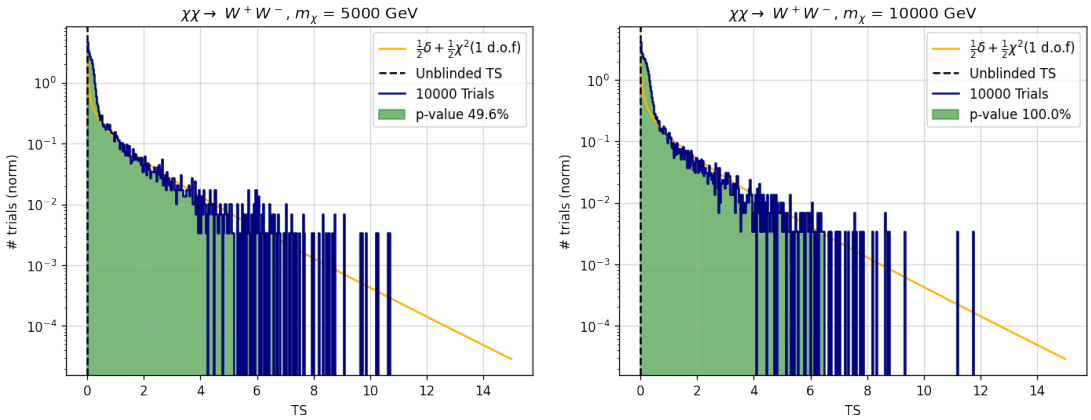

Figure A.11 – Test statistic distributions for the HE DM scenarios $\chi\chi \to W^+W^-$, $m_\chi = 5$ TeV (left) and $m_\chi = 10$ TeV (right).

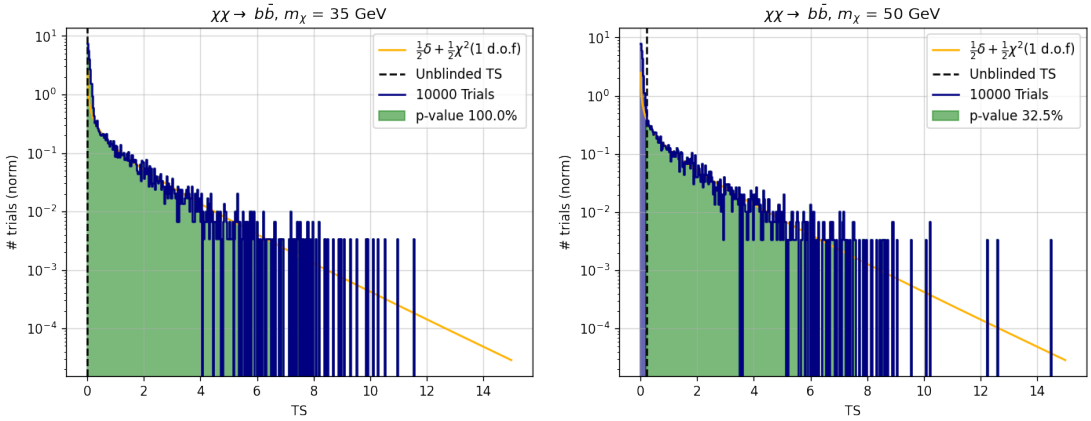

Figure A.12 – Test statistic distributions for the LE DM scenarios $\chi\chi \to b\bar{b}$, $m_\chi = 35$ GeV (left) and $m_\chi = 50$ GeV (right).

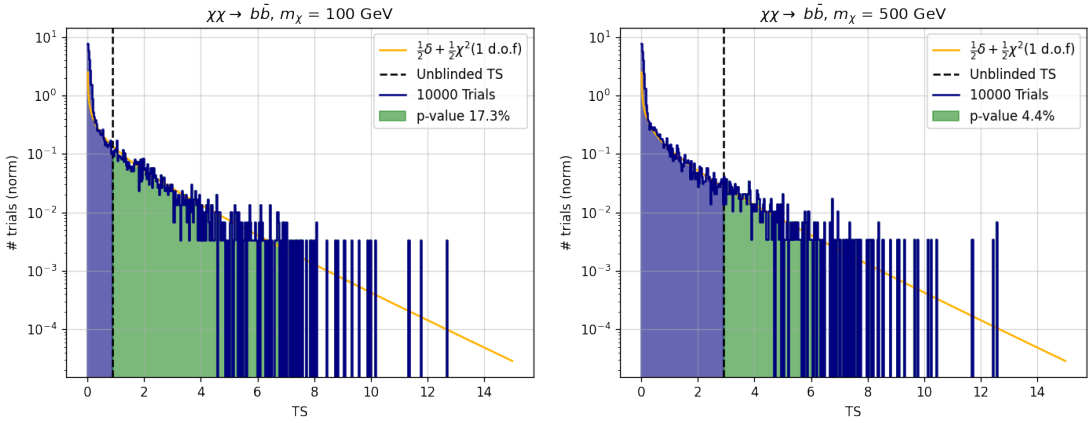

Figure A.13 – Test statistic distributions for the LE DM scenario $\chi\chi \to b\bar{b}$, $m_\chi = 100$ GeV (left) and HE scenario $m_\chi = 500$ GeV (right).

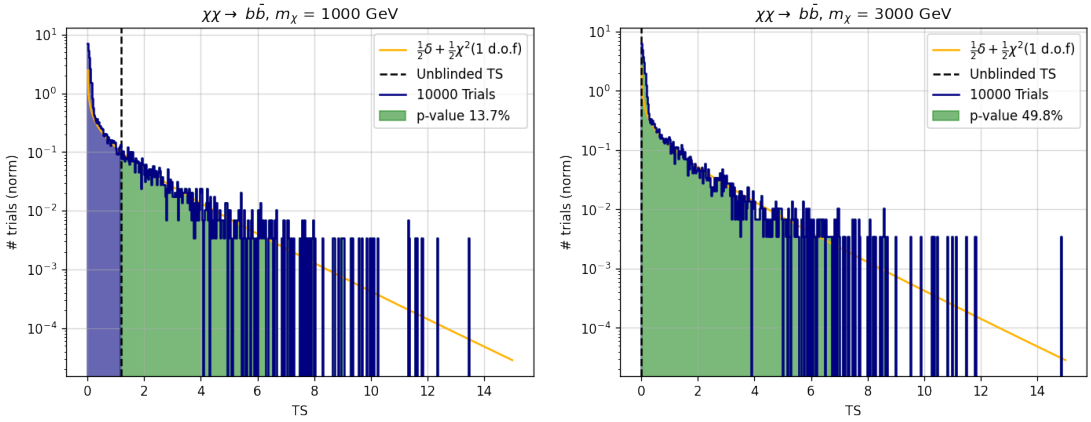

Figure A.14 – Test statistic distributions for the HE DM scenarios $\chi\chi \to b\bar{b}$, $m_\chi = 1$ TeV (left) and $m_\chi = 3$ TeV (right).

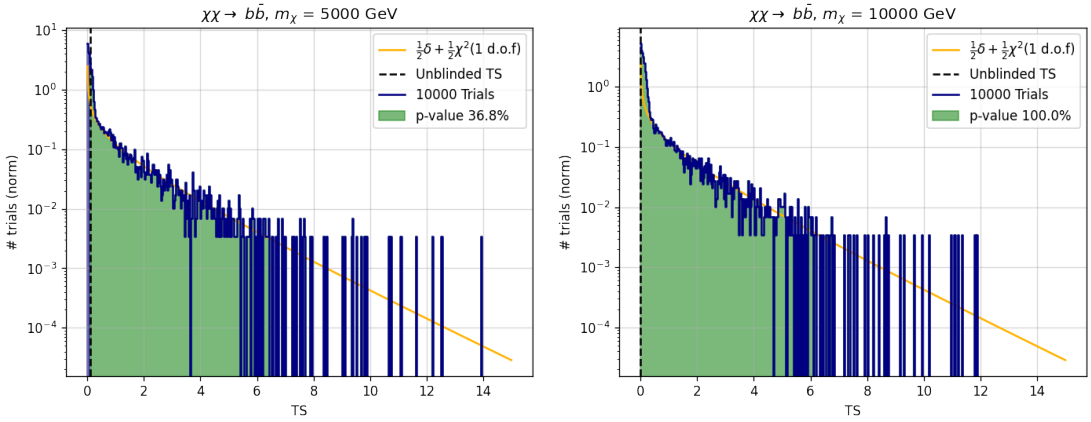

Figure A.15 – Test statistic distributions for the HE DM scenarios $\chi\chi \to b\bar{b}$, $m_\chi = 5$ TeV (left) and $m_\chi = 10$ TeV (right).

APPENDIX B

FURTHER EFT LIMITS

Further limits on the effective theory coupling constants are presented here. This limits show that the improvement with respect to results from [61] corresponds to expectations (see 6.3).

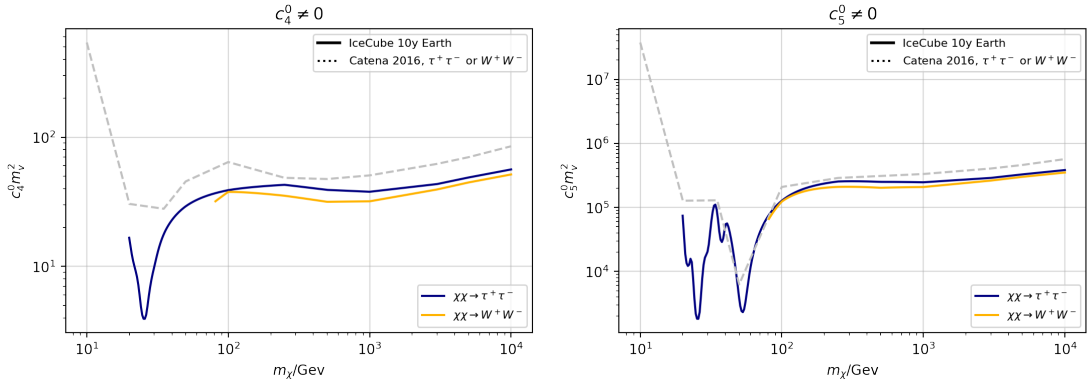

Figure B.1 – Limits for the coupling constants c_4^0 (left) and c_5^0 (right). For comparison, limits from [61] are shown.

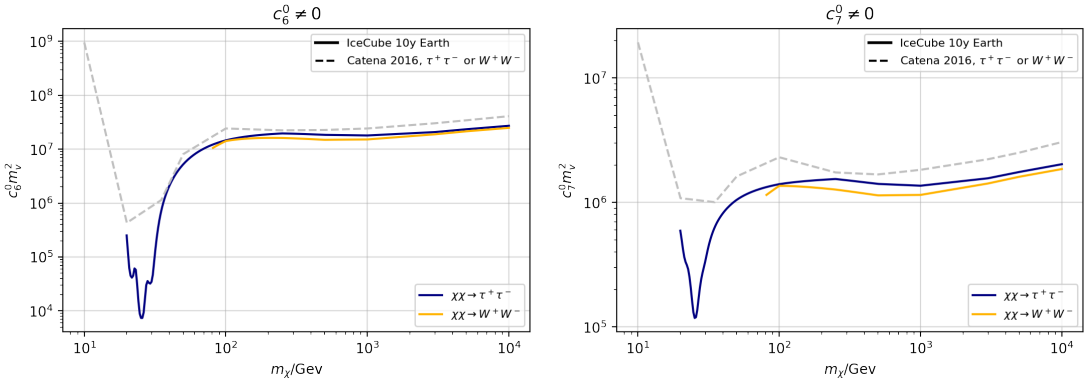

Figure B.2 – Limits for the coupling constants c_6^0 and c_7^0 (right). For comparison, limits from [61] are shown.

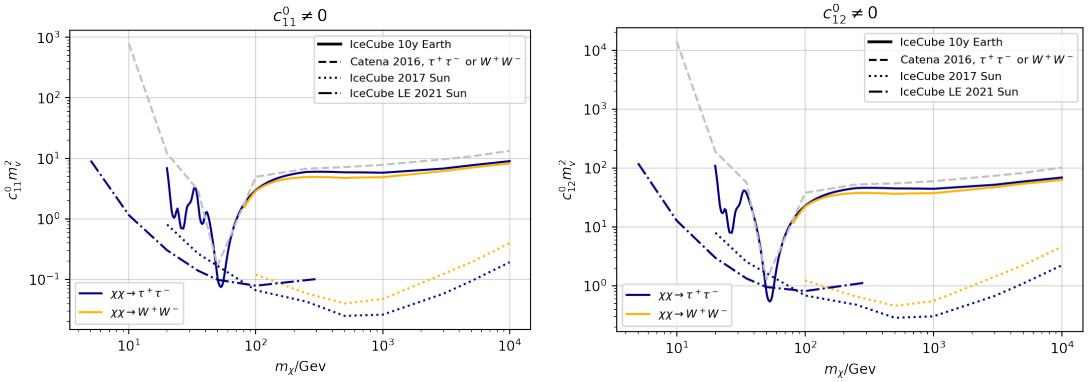

Figure B.3 – Limits for the coupling constants c_8^0 and c_9^0 (right). For comparison, limits from [61] and [123] (only for c_9^0) are shown.

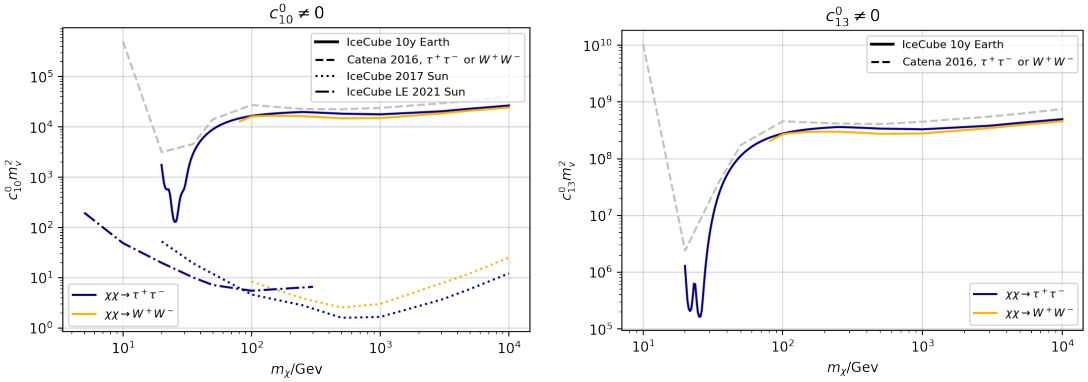

Figure B.4 – Limits for the coupling constants c_{10}^0 and c_{13}^0 (right). For comparison, limits from [61] and [123] (only for c_{10}^0) are shown.

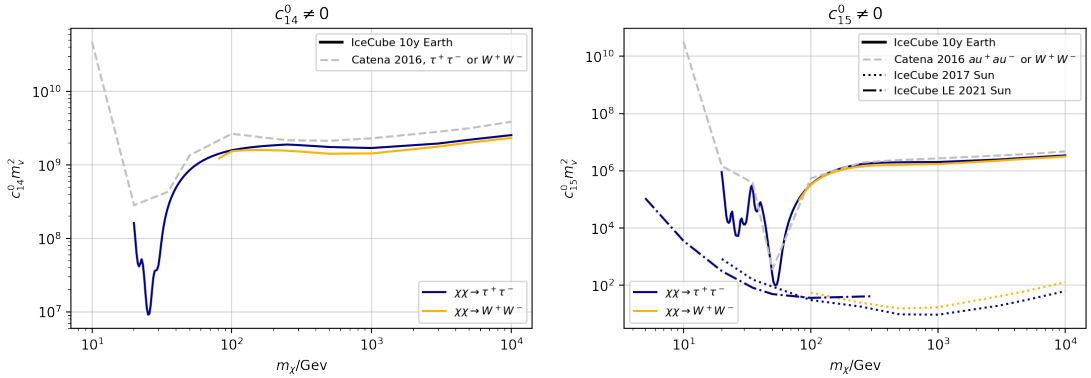

Figure B.5 – Limits for the coupling constants c_{14}^0 and c_{15}^0 (right). For comparison, limits from [61] and [123] (only for c_{15}^0) are shown.

BIBLIOGRAPHY

[1] Aartsen, M., *et al.* (2013). Evidence for High-Energy Extraterrestrial Neutrinos at the IceCube Detector. *Science*, *342*(6161), 1242856. doi:10.1126/science.1242856.

[2] Aartsen, M., *et al.* (2013). South Pole glacial climate reconstruction from multi-borehole laser particulate stratigraphy. *Journal of Glaciology*, *59*(218), 1117–1128. doi:10.3189/2013JoG13J068.

[3] Aartsen, M., *et al.* (2016). Search for annihilating dark matter in the Sun with 3 years of IceCube data. *European Physical Journal C*, *77*, 146. doi:10.1140/epjc/s10052-017-4689-9.

[4] Aartsen, M., *et al.* (2017). Search for Neutrinos from Dark Matter Self-Annihilations in the center of the Milky Way with 3 years of IceCube/DeepCore. *The European Physical Journal C*, *77*. doi:10.1140/epjc/s10052-017-5213-y.

[5] Aartsen, M., *et al.* (2018). Multimessenger observations of a flaring blazar coincident with high-energy neutrino IceCube-170922A. *Science*, *361*(6398), eaat1378. doi:10.1126/science.aat1378.

[6] Aartsen, M., *et al.* (2018). Neutrino emission from the direction of the blazar TXS 0506+056 prior to the IceCube-170922A alert. *Science*, *361*. doi:10.1126/science.aat2890.

[7] Aartsen, M., *et al.* (2018). Search for neutrinos from decaying dark matter with IceCube: IceCube Collaboration. *The European Physical Journal C*, *78*. doi:10.1140/epjc/s10052-018-6273-3.

[8] Aartsen, M., *et al.* (2021). Detection of a particle shower at the Glashow resonance with IceCube. *Nature*, *591*, 220–224. doi:10.1038/s41586-021-03256-1.

[9] Aartsen, M., *et al.* (2021). Searches for neutrinos from cosmic-ray interactions in the Sun using seven years of IceCube data. *Journal of Cosmology and Astroparticle Physics*, *2021*(2). ISSN 1475-7516. doi:10.1088/1475-7516/2021/02/025. Publisher Copyright: © 2021 IOP Publishing Ltd and Sissa Medialab.

[10] Aartsen, M. G., Ackermann, M., Adams, J., Aguilar, J. A., *et al.* (2020). Time-Integrated Neutrino Source Searches with 10 Years of IceCube Data. *Phys. Rev. Lett.*, *124*, 051103. doi:10.1103/PhysRevLett.124.051103.

[11] Aartsen, M. G., *et al.* (2013). Measurement of South Pole ice transparency with the IceCube LED calibration system. *Nucl. Instrum. Meth. A*, *711*, 73–89. doi:10.1016/j.nima.2013.01.054.

[12] Aartsen, M. G., *et al.* (2017). First search for dark matter annihilations in the Earth with the IceCube Detector. *EPJ C*, *77*(2), 82. doi:10.1140/epjc/s10052-016-4582-y.

[13] Aartsen, M. G., *et al.* (2017). The IceCube Neutrino Observatory: Instrumentation and Online Systems. *JINST*, *12*(03), P03012. doi:10.1088/1748-0221/12/03/P03012.

[14] Aartsen, M. G., *et al.* (2018). Measurement of Atmospheric Neutrino Oscillations at 6-56 GeV with IceCube DeepCore. *Phys. Rev. Lett.*, *120*, 071801. doi:10.1103/PhysRevLett.120.071801.

[15] Aartsen, M. G., *et al.* (2020). Velocity Independent Constraints on Spin-Dependent DM-Nucleon Interactions from IceCube and PICO. *Eur. Phys. J. C*, *80*(9), 819. doi:10.1140/epjc/s10052-020-8069-5.

[16] Abazajian, K. N., Kaplinghat, M. (2012). Detection of a gamma-ray source in the Galactic Center consistent with extended emission from dark matter annihilation and concentrated astrophysical emission. *Phys. Rev. D*, *86*, 083511. doi:10.1103/PhysRevD.86.083511.

[17] Abbasi, R., *et al.* (2021). IceCube high-energy starting event sample: Description and flux characterization with 7.5 years of data. *Phys. Rev. D*, *104*, 022002. doi:10.1103/PhysRevD.104.022002.

[18] Abbasi, R., *et al.* (2021). A muon-track reconstruction exploiting stochastic losses for large-scale Cherenkov detectors. *Journal of Instrumentation*, *16*, P08034. doi:10.1088/1748-0221/16/08/P08034.

[19] Abbasi, R., *et al.* (2022). Improved Characterization of the Astrophysical Muon–neutrino Flux with 9.5 Years of IceCube Data. *Astrophys. J.*, *928*(1), 50. doi:10.3847/1538-4357/ac4d29.

[20] Abdallah, H., *et al.* (2016). Search for Dark Matter Annihilations towards the Inner Galactic Halo from 10 Years of Observations with H.E.S.S. *Phys. Rev. Lett.*, *117*, 111301. doi:10.1103/PhysRevLett.117.111301.

[21] Abe, K., Bronner, C., Haga, Y., Hayato, Y., Ikeda, M., Imaizumi, S., *et al.* (2020). Indirect search for dark matter from the Galactic Center and halo with the Super-Kamiokande detector. *Phys. Rev. D*, *102*, 072002. doi:10.1103/PhysRevD.102.072002.

[22] Accardo, L., Aguilar, M., Aisa, D., *et al.* (2014). High Statistics Measurement of the Positron Fraction in Primary Cosmic Rays of 0.5–500 GeV with the Alpha Magnetic Spectrometer on the International Space Station. *Phys. Rev. Lett.*, *113*, 121101. doi:10.1103/PhysRevLett.113.121101.

[23] Ackermann, M., *et al.* (2015). Searching for Dark Matter Annihilation from Milky Way Dwarf Spheroidal Galaxies with Six Years of Fermi Large Area Telescope Data. *Phys. Rev. Lett.*, *115*, 231301. doi:10.1103/PhysRevLett.115.231301.

[24] Ackermann, M., *et al.* (2017). The Fermi Galactic Center GeV Excess and Implications for Dark Matter. *The Astrophysical Journal*, *840*, 43. doi:10.3847/1538-4357/aa6cab.

[25] Adhikari, G., *et al.* (2019). Search for a Dark Matter-Induced Annual Modulation Signal in NaI(Tl) with the COSINE-100 Experiment. *Physical Review Letters*, *123*. doi:10.1103/PhysRevLett.123.031302.

[26] Adrián-Martínez, S., Ageron, M., Aharonian, F., *et al.* (2016). Letter of intent for KM3NeT 2.0. *Journal of Physics G: Nuclear and Particle Physics*, *43*(8), 084001. doi:10.1088/0954-3899/43/8/084001.

[27] Adrián-Martínez, S., *et al.* (2016). A search for Secluded Dark Matter in the Sun with the ANTARES neutrino telescope. *JCAP*, *05*, 016. doi:10.1088/1475-7516/2016/05/016.

[28] Adrian-Martinez, S., *et al.* (2016). Limits on Dark Matter Annihilation in the Sun using the ANTARES Neutrino Telescope. *Phys. Lett. B*, *759*, 69–74. doi:10.1016/j.physletb.2016.05.019.

[29] Adriani, O., *et al.* (2009). An anomalous positron abundance in cosmic rays with energies 1.5-100 GeV. *Nature*, *458*, 607–609. doi:10.1038/nature07942.

[30] Aghanim, N., *et al.* (2020). Planck 2018 results. VI. Cosmological parameters. *Astron. Astrophys.*, *641*, A6. doi:10.1051/0004-6361/201833910.

[31] Agnes, P., *et al.* (2018). DarkSide-50 532-day Dark Matter Search with Low-Radioactivity Argon. *Phys. Rev. D*, *98*(10), 102006. doi:10.1103/PhysRevD.98.102006.

[32] Agnes, P., *et al.* (2018). Low-Mass Dark Matter Search with the DarkSide-50 Experiment. *Phys. Rev. Lett.*, *121*(8), 081307. doi:10.1103/PhysRevLett.121.081307.

[33] Agostini, M., Böhmer, M., Bosma, J., *et al.* (2020). The Pacific Ocean Neutrino Experiment. *Nature Astronomy*, *4*, 913–915. doi:10.1038/s41550-020-1182-4.

[34] Aguilar, J., Allison, P., Beatty, J., *et al.* (2021). Design and sensitivity of the Radio Neutrino Observatory in Greenland (RNO-G). *Journal of Instrumentation*, *16*(03), P03025. doi:10.1088/1748-0221/16/03/p03025.

[35] Ahnen, M., *et al.* (2016). Limits to Dark Matter Annihilation Cross-Section from a Combined Analysis of MAGIC and Fermi-LAT Observations of Dwarf Satellite Galaxies. *JCAP*, *02*, 039. doi:10.1088/1475-7516/2016/02/039.

[36] Akerib, D. S., *et al.* (2017). Results from a search for dark matter in the complete LUX exposure. *Phys. Rev. Lett.*, *118*(2), 021303. doi:10.1103/PhysRevLett.118.021303.

[37] Akerib, D. S., *et al.* (2019). Results of a Search for Sub-GeV Dark Matter Using 2013 LUX Data. *Phys. Rev. Lett.*, *122*(13), 131301. doi:10.1103/PhysRevLett.122.131301.

[38] Akrami, Y., *et al.* (2020). Planck 2018 results: VII. Isotropy and statistics of the CMB. *Astron. Astrophys.*, *641*. doi:10.1051/0004-6361/201935201.

[39] Albert, A., *et al.* (2017). Results from the search for dark matter in the Milky Way with 9 years of data of the ANTARES neutrino telescope. *Physics Letters B*, *769*, 249–254. ISSN 0370-2693. doi:https://doi.org/10.1016/j.physletb.2017.03.063.

[40] Albert, A., *et al.* (2017). Search for Dark Matter Annihilation in the Earth using the ANTARES Neutrino Telescope. *Phys. Dark Univ.*, *16*, 41–48. doi:https://doi.org/10.1016/j.dark.2017.04.005.

[41] Albert, A., *et al.* (2020). Combined search for neutrinos from dark matter self-annihilation in the Galactic Center with ANTARES and IceCube. *Phys. Rev. D*, *102*, 082002. doi:10.1103/PhysRevD.102.082002.

[42] Aleksić, J., *et al.* (2013). Optimized dark matter searches in deep observations of Segue 1 with MAGIC. *Journal of Cosmology and Astroparticle Physics*, *2014*, 008. doi:10.1088/1475-7516/2014/02/008.

[43] Amole, C., *et al.* (2019). Dark matter search results from the complete exposure of the PICO-60 C 3 F 8 bubble chamber. *Physical Review D*, *100*. doi:10.1103/PhysRevD.100.022001.

[44] Andreopoulos, C., Barry, C., Dytman, S., Gallagher, H., Golan, T., Hatcher, R., Perdue, G., Yarba, J. (2015). The GENIE Neutrino Monte Carlo Generator: Physics and User Manual.

[45] Aprile, E., *et al.* (2018). Dark Matter Search Results from a One Ton-Year Exposure of XENON1T. *Phys. Rev. Lett.*, *121*(11), 111302. doi:10.1103/PhysRevLett.121.111302.

[46] Aprile, E., *et al.* (2019). Constraining the spin-dependent WIMP-nucleon cross sections with XENON1T. *Phys. Rev. Lett.*, *122*(14), 141301. doi:10.1103/PhysRevLett.122.141301.

[47] Archambault, S., *et al.* (2017). Dark matter constraints from a joint analysis of dwarf Spheroidal galaxy observations with VERITAS. *Phys. Rev. D*, *95*, 082001. doi:10.1103/PhysRevD.95.082001.

[48] Avrorin, A., *et al.* (2016). A search for neutrino signal from dark matter annihilation in the center of the Milky Way with Baikal NT200. *Astroparticle Physics*, *81*, 12–20. ISSN 0927-6505. doi:https://doi.org/10.1016/j.astropartphys.2016.04.004.

[49] Barr, G. D., Gaisser, T. K., Lipari, P., Robbins, S., Stanev, T. (2004). Three-dimensional calculation of atmospheric neutrinos. *Phys. Rev. D*, *70*, 023006. doi:10.1103/PhysRevD.70.023006.

[50] Bartolo, N., De Luca, V., Franciolini, G., Lewis, A., Peloso, M., Riotto, A. (2019). Primordial Black Hole Dark Matter: LISA Serendipity. *Phys. Rev. Lett.*, *122*, 211301. doi:10.1103/PhysRevLett.122.211301.

[51] Batell, B., Pospelov, M., Ritz, A., Shang, Y. (2010). Solar gamma rays powered by secluded dark matter. *Phys. Rev. D*, *81*, 075004. doi:10.1103/PhysRevD.81.075004.

[52] Baur, S., for the IceCube Collaboration (2019). Dark matter searches with the IceCube Upgrade. *PoS*, *ICRC2019*(506).

[53] Bernabei, R., *et al.* (2018). First model independent results from DAMA/LIBRA-phase2. *Universe*, *4*(11), 116. doi:10.3390/universe4110116.

[54] Bertone, G., Hooper, D., Silk, J. (2005). Particle Dark Matter: Evidence, Candidates and Constraints. *Phys.Rept.*, *405*, 279–390.

[55] Betti, M., Biasotti, M., Boscá, A., *et al.* (2019). Neutrino physics with the PTOLEMY project: active neutrino properties and the light sterile case. *Journal of Cosmology and Astroparticle Physics*, *2019*(07), 047. doi:10.1088/1475-7516/2019/07/047.

[56] Billard, J., Boulay, M., Cebrián, S., Covi, L., *et al.* (2021). Direct Detection of Dark Matter – APPEC Committee Report.

[57] Blennow, M., Edsjö, J., Ohlsson, T. (2008). Neutrinos from WIMP annihilations obtained using a full three-flavor Monte Carlo approach. *JCAP, WimpSim Neutrino Monte Carlo, http://wimpsim.astroparticle.se/*(01), 021. doi:10.1088/1475-7516/2008/01/021.

[58] Bringmann, T., Edsjo, J., Gondolo, P., Ullio, P., Bergstrom, L. (2018). DarkSUSY 6 : An Advanced Tool to Compute Dark Matter Properties Numerically. *Journal of Cosmology and Astroparticle Physics*, *2018*. doi:10.1088/1475-7516/2018/07/033.

[59] Burkert, A. (1995). The Structure of Dark Matter Halos in Dwarf Galaxies. *arXiv*, *447*, L25. doi:10.1086/309560.

[60] Carroll, S. M. (2019). *Spacetime and Geometry*. Cambridge University Press. ISBN 978-0-8053-8732-2, 978-1-108-48839-6, 978-1-108-77555-7.

[61] Catena, R. (2017). WIMP capture and annihilation in the Earth in effective theories. *Journal of Cosmology and Astroparticle Physics*, *2017*(01), 059–059. doi:10.1088/1475-7516/2017/01/059.

[62] Cheng, H.-C., Feng, J. L., Matchev, K. T. (2002). Kaluza-Klein Dark Matter. *Phys. Rev. Lett.*, *89*, 211301. doi:10.1103/PhysRevLett.89.211301.

[63] Cherenkov, P. A. (1934). Visible luminescence of pure liquids under the influence of γ-radiation. *Dokl. Akad. Nauk SSSR*, *2*(8), 451–454. doi:10.3367/UFNr.0093.196710n.0385.

[64] Chernyshov, D. O., Egorov, A. E., Dogiel, V. A., Ivlev, A. V. (2021). On a Possible Origin of the Gamma-ray Excess around the Galactic Center. *Symmetry*, *13*(8). ISSN 2073-8994. doi:10.3390/sym13081432.

[65] Chirkin, D., IceCube Collaboration (2013). Evidence of optical anisotropy of the South Pole ice. In *International Cosmic Ray Conference*, *International Cosmic Ray Conference*, Bd. 33, (3338).

[66] Choi, K., *et al.* (2015). Search for Neutrinos from Annihilation of Captured Low-Mass Dark Matter Particles in the Sun by Super-Kamiokande. *Phys. Rev. Lett.*, *114*, 141301. doi:10.1103/PhysRevLett.114.141301.

[67] Clowe, D., Bradac, M., Gonzalez, A. H., Markevitch, M., Randall, S. W., Jones, C., Zaritsky, D. (2006). A direct empirical proof of the existence of dark matter. *Astrophys. J. Lett.*, *648*, L109–L113. doi:10.1086/508162.

[68] Cocco, A. G., Mangano, G., Messina, M. (2008). Probing low energy neutrino backgrounds with neutrino capture on beta decaying nuclei. *Journal of Physics: Conference Series*, *110*(8), 082014. doi:10.1088/1742-6596/110/8/082014.

[69] Cooper-Sarkar, A., Mertsch, P., Sarkar, S. (2011). The high energy neutrino cross-section in the Standard Model and its uncertainty. *JHEP*, *08*, 042. doi:10.1007/JHEP08(2011)042.

[70] Cotner, E., Kusenko, A. (2017). Primordial Black Holes from Supersymmetry in the Early Universe. *Phys. Rev. Lett.*, *119*, 031103. doi:10.1103/PhysRevLett.119.031103.

[71] Cowan, G., Cranmer, K., Gross, E., Vitells, O. (2013). Asymptotic formulae for likelihood-based tests of new physics (vol 71, pg 1554, 2011). *European Physical Journal C*, *73*. doi:10.1140/epjc/s10052-013-2501-z.

[72] Cremonesi, L., Connolly, A., Allison, P., *et al.* (2019). The simulation of the sensitivity of the Antarctic Impulsive Transient Antenna (ANITA) to Askaryan radiation from cosmogenic neutrinos interacting in the Antarctic Ice. *Journal of Instrumentation*, *14*(08), P08011–P08011. doi:10.1088/1748-0221/14/08/p08011.

[73] Delaunay, C., Fox, P. J., Perez, G., Fox, P. J. (2009). Probing dark matter dynamics via earthborn neutrinos at IceCube. *Journal of High Energy Physics*, *2009*(05), 099 – 099. doi:10.1088/1126-6708/2009/05/099. 5 pages and 3 figures.

[74] Dembinski, H., et al., P. O. (2020). scikit-hep/iminuit. doi:10.5281/zenodo.3949207.

[75] Edsjö, J., Bringmann, T., Gondolo, P., P. Ullio, Bergström, L., Schelke, M., Baltz, E., Duda, G. DarkSusy, http://www.darksusy.org.

[76] Edsjö, J., Elevant, J., Niblaeus, C. WimpSim Neutrino Monte Carlo, http://wimpsim.astroparticle.se/.

[77] Enberg, R., Reno, M. H., Sarcevic, I. (2008). Prompt neutrino fluxes from atmospheric charm. *Phys. Rev. D*, *78*, 043005. doi:10.1103/PhysRevD.78.043005.

[78] Evans, L., Bryant, P. (2008). LHC Machine. *Journal of Instrumentation*, *3*(08), S08001–S08001. doi:10.1088/1748-0221/3/08/s08001.

[79] Feng, J. L., Kumar, J., Marfatia, D., Sanford, D. (2011). Isospin-Violating Dark Matter. *Phys. Lett. B*, *703*, 124–127. doi:10.1016/j.physletb.2011.07.083.

[80] Fermi, E. (1934). An attempt of a theory of beta radiation. 1. *Z. Phys.*, *88*, 161–177. doi:10.1007/BF01351864.

[81] Fitzpatrick, A. L., Haxton, W., Katz, E., Lubbers, N., Xu, Y. (2013). The effective field theory of dark matter direct detection. *Journal of Cosmology and Astroparticle Physics*, *2013*(02), 004–004. doi:10.1088/1475-7516/2013/02/004.

[82] Fixsen, D. J. (2009). The Temperature of the Cosmic Microwave Background. , *707*(2), 916–920. doi:10.1088/0004-637X/707/2/916.

[83] Formaggio, J. A., Zeller, G. P. (2012). From eV to EeV: Neutrino cross sections across energy scales. *Rev. Mod. Phys.*, *84*, 1307–1341. doi:10.1103/RevModPhys.84.1307.

[84] Frank, I. M., Tamm, I. E. (1937). Coherent visible radiation of fast electrons passing through matter. *Compt. Rend. Acad. Sci. URSS*, *14*(3), 109–114. doi:10.3367/UFNr.0093.196710o.0388.

[85] Garani, R., Palomares-Ruiz, S. (2021). Evaporation of dark matter from celestial bodies.

[86] Gazizov, A., Kowalski, M. (2005). ANIS: High energy neutrino generator for neutrino telescopes. *Computer Physics Communications*, *172*(3), 203–213. ISSN 0010-4655. doi:https://doi.org/10.1016/j.cpc.2005.03.113.

[87] Gil, A., Segura, J., Temme, N. M. (2007). *Numerical Methods for Special Functions*. Society for Industrial and Applied Mathematics. doi:10.1137/1.9780898717822.

[88] Gondolo, P., Edsjo, J., Ullio, P., Bergstrom, L., Schelke, M., Baltz, E. (2004). DarkSUSY: Computing Supersymmetric Dark Matter Properties Numerically. *Journal of Cosmology and Astroparticle Physics*, *2004*. doi:10.1088/1475-7516/2004/07/008.

[89] Gott, I., J. Richard, Jurić, M., Schlegel, D., Hoyle, F., Vogeley, M., Tegmark, M., Bahcall, N., Brinkmann, J. (2005). A Map of the Universe. , *624*(2), 463–484. doi:10.1086/428890.

[90] Green, A. M., Kavanagh, B. J. (2021). Primordial black holes as a dark matter candidate. *Journal of Physics G: Nuclear and Particle Physics*, *48*(4), 043001. doi:10.1088/1361-6471/abc534.

[91] Greisen, K. (1966). End to the Cosmic-Ray Spectrum? *Phys. Rev. Lett.*, *16*, 748–750. doi:10.1103/PhysRevLett.16.748.

[92] Griest, K., Seckel, D. (1987). Dark matter disc enhanced neutrino fluxes from the Sun and Earth. *Nucl. Phys. B*, *283*, 681.

[93] Hagiwara, K., Okamura, N., Senda, K.-i. (2011). The earth matter effects in neutrino oscillation experiments from Tokai to Kamioka and Korea. *Journal of High Energy Physics*, *2011*, 1–40. doi:10.1007/JHEP09(2011)082.

[94] Heck, D., Knapp, J., Capdevielle, J., Schatz, G., Thouw, T. (1998). CORSIKA: A Monte Carlo Code to Simulate Extensive Air Showers. *FZKA, 6019*.

[95] Pérez de los Heros, C. (2020). Status, Challenges and Directions in Indirect Dark Matter Searches. *Symmetry*, *12*(10), 1648. ISSN 2073-8994.

[96] Honda, M., Athar, M. S., Kajita, T., Kasahara, K., Midorikawa, S. (2015). Atmospheric neutrino flux calculation using the NRLMSISE-00 atmospheric model. *Phys. Rev. D*, *92*, 023004. doi:10.1103/PhysRevD.92.023004.

[97] Honda, M., Kajita, T., Kasahara, K., Midorikawa, S., Sanuki, T. (2007). Calculation of atmospheric neutrino flux using the interaction model calibrated with atmospheric muon data. *Phys. Rev. D*, *75*, 043006. doi:10.1103/PhysRevD.75.043006.

[98] Iovine, N., for the IceCube Collaboration (2021). Indirect search for dark matter in the Galactic Centre with IceCube. *PoS*, *ICRC2021*(524).

[99] Ishihara, A., for the IceCube collaboration (2021). The IceCube Upgrade - Design and Science Goals. *PoS*, *ICRC2019*, 1031. doi:10.22323/1.358.1031.

[100] James, F., Roos, M. (1975). Minuit: A System for Function Minimization and Analysis of the Parameter Errors and Correlations. *Comput. Phys. Commun.*, *10*, 343–367. doi:10.1016/0010-4655(75)90039-9.

[101] Jungman, G., Kamionkowski, M., Griest, K. (1996). Supersymmetric dark matter. *Phys. Rept.*, *267*, 195–373.

[102] Kajita, T. (1999). Atmospheric neutrino results from Super-Kamiokande and Kamiokande — Evidence for $\nu\mu$ oscillations. *Nuclear Physics B - Proceedings Supplements*, *77*(1), 123–132. ISSN 0920-5632. doi:https://doi.org/10.1016/S0920-5632(99)00407-7.

[103] Kunnen, J. (2015). *A search for Dark Matter in the center of the Earth with the IceCube neutrino detector*. Dissertation, Vrije Universiteit Brussel.

[104] Learned, J. G., Mannheim, K. (2000). High-Energy Neutrino Astrophysics. *Annual Review of Nuclear and Particle Science*, *50*(1), 679–749. doi:10.1146/annurev.nucl.50.1.679.

[105] Leuermann, M. (2018). *Testing the Neutrino Mass Ordering with IceCube DeepCore*. Dissertation, RWTH Aachen U. doi:10.18154/RWTH-2018-231554.

[106] Lisanti, M. (2017). Lectures on Dark Matter Physics. In *Theoretical Advanced Study Institute in Elementary Particle Physics: New Frontiers in Fields and Strings*, (399–446). doi:10.1142/9789813149441_0007.

[107] Liu, Z. Z., *et al.* (2019). Constraints on Spin-Independent Nucleus Scattering with sub-GeV Weakly Interacting Massive Particle Dark Matter from the CDEX-1B Experiment at the China Jinping Underground Laboratory. *Phys. Rev. Lett.*, *123*(16), 161301. doi:10.1103/PhysRevLett.123.161301.

[108] Markov, M., Zheleznykh, I. (1961). On high energy neutrino physics in cosmic rays. *Nuclear Physics*, *27*(3), 385–394. ISSN 0029-5582. doi:https://doi.org/10.1016/0029-5582(61)90331-5.

[109] McDonough, W. (2003). Compositional Model for the Earth's Core. *Treatise on Geochemistry*, *2*, 547–568. doi:10.1016/B0-08-043751-6/02015-6.

[110] Mijakowski, P. (2020). Dark Matter Searches at Super-Kamiokande. *Journal of Physics: Conference Series*, *1342*, 012075. doi:10.1088/1742-6596/1342/1/012075.

[111] Mikheyev, S. P., Smirnov, A. Y. (1985). Resonance Amplification of Oscillations in Matter and Spectroscopy of Solar Neutrinos. *Sov. J. Nucl. Phys.*, *42*, 913–917.

[112] "MissMj", "Cush". *Wikipedia, the free encyclopedia*. Accessed on September, 22nd, 2021 at `https://commons.wikimedia.org/wiki/File:Standard_Model_of_Elementary_Particles.svg`.

[113] Mocioiu, I., Shrock, R. (2000). Matter effects on neutrino oscillations in long baseline experiments. *Phys. Rev. D*, *62*, 053017. doi:10.1103/PhysRevD.62.053017.

[114] Navarro, J. F., Frenk, C. S., White, S. D. M. (1996). The Structure of Cold Dark Matter Halos. *The Astrophysical Journal*, *462*, 563. doi:10.1086/177173.

[115] Necib, L., Lisanti, M., Belokurov, V. A. (2019). Inferred Evidence for Dark Matter Kinematic Substructure with SDSS–Gaia. *The Astrophysical Journal*, *874*.

[116] Oakes, L., Armand, C., Charles, E., *et al.* (2019). Combined Dark Matter searches towards dwarf spheroidal galaxies with Fermi-LAT, HAWC, HESS, MAGIC and VERITAS. *PoS*, *ICRC2019*.

[117] Page, J. P., Plant, R. (1971). Stairway To Heaven. *Untitled. Led Zeppelin*.

[118] Patrignani, C., *et al.* (2016). Review of Particle Physics. *Chinese Physics C*, *40*(10), 100001. doi:10.1088/1674-1137/40/10/100001.

[119] Pauli, W. (1930). Radioactivity of Tübingen.

[120] Peccei, R. D., Quinn, H. R. (1977). Constraints imposed by CP conservation in the presence of pseudoparticles. *Phys. Rev. D*, *16*, 1791–1797. doi:10.1103/PhysRevD.16.1791.

[121] Pedregosa, F., Varoquaux, G., Gramfort, A., Michel, V., Thirion, B., Grisel, O., Blondel, M., Prettenhofer, P., Weiss, R., Dubourg, V., Vanderplas, J., Passos, A., Cournapeau, D., Brucher, M., Perrot, M., Duchesnay, E. (2011). Scikit-learn: Machine Learning in Python. *Journal of Machine Learning Research*, *12*, 2825–2830.

[122] Penzias, A. A., Wilson, R. W. (1965). A Measurement of Excess Antenna Temperature at 4080 Mc/s. , *142*, 419–421. doi:10.1086/148307.

[123] Peters, L. (2021). *Constraining generalized Dark Matter-Nucleon Interactions based on Dark Matter Capture in the Sun with IceCube*. Dissertation, RWTH Aachen University.

[124] Peters, L., for the IceCube collaboration (2021). Constraining non-standard Dark Matter-Nucleon Interactions with IceCube. *PoS*, *ICRC2021*, 522. doi:10.22323/1.395.0522.

[125] Planck Collaboration, Aghanim, N., Akrami, Y., Arroja, F. (2020). Planck 2018 results - I. Overview and the cosmological legacy of Planck. *A&A*, *641*, A1. doi:10.1051/0004-6361/201833880.

[126] Pontecorvo, B. (1958). Mesonium and Antimesonium. *Soviet Journal of Experimental and Theoretical Physics*, *6*, 429.

[127] Reines, F., Cowan, C. L., Harrison, F. B., McGuire, A. D., Kruse, H. W. (1960). Detection of the Free Antineutrino. *Phys. Rev.*, *117*, 159–173. doi:10.1103/PhysRev.117.159.

[128] Rich, J. (2009). *Fundamentals of Cosmology. 2nd Edition*.

[129] Richman, M. (2015). *A search for muon neutrinos cincident with northern Gamma-Ray Bursts using IceCube*. Dissertation, University of Maryland.

[130] Rubin, V. C., Ford, J., W. Kent (1970). Rotation of the Andromeda Nebula from a Spectroscopic Survey of Emission Regions. *Astrophys. J.*, *159*, 379. doi:10.1086/150317.

[131] Schöneberg, S. (2016). *The spectrum of atmospheric neutrinos above GeV energies*. Dissertation, Ruhr U., Bochum (main).

[132] Servant, G., Tait, T. M. (2003). Is the lightest Kaluza–Klein particle a viable dark matter candidate? *Nuclear Physics B*, *650*(1), 391–419. ISSN 0550-3213. doi:https://doi.org/10.1016/S0550-3213(02)01012-X.

[133] Springel, V., Frenk, C., White, S. (2006). The large-scale structure of the Universe. *Nature*, *440*, 1137–44. doi:10.1038/nature04805.

[134] Stettner, J. (2019). Measurement of the diffuse astrophysical muon-neutrino spectrum with ten years of IceCube data. *PoS*, *ICRC2019*.

[135] Supanitsky, A. D. (2022). Determination of the Cosmic-Ray Chemical Composition: Open Issues and Prospects. *Galaxies*, *10*(3), 75. doi:10.3390/galaxies10030075.

[136] Thomson, M. (2013). *Modern Particle Physics*. Cambridge University Press. doi:10.1017/CBO9781139525367.

[137] Tian, W., for the IceCube Collaboration (2022). Posteriori analysis on IceCube double pulse tau neutrino candidates. 1146.

[138] Tisserand, P., Le Guillou, L., Afonso, C., *et al.* (2007). Limits on the Macho Content of the Galactic Halo from the EROS-2 Survey of the Magellanic clouds. *Astronomy and Astrophysics*, *469*, 387–404. doi:10.1051/0004-6361:20066017.

[139] Tucker, W., Blanco, P., Rappoport, S., David, L., Fabricant, D., Falco, E. E., Forman, W., Dressler, A., Ramella, M. (1998). 1e0657-56: a contender for the hottest known cluster of galaxies. *Astrophys. J. Lett.*, *496*, L5. doi:10.1086/311234.

[140] Tumasyan, A., *et al.* (2021). Search for new particles in events with energetic jets and large missing transverse momentum in proton-proton collisions at $\sqrt{s} =$ 13 TeV. *JHEP*, *11*, 153. doi:10.1007/JHEP11(2021)153.

[141] Venumadhav, T., Cyr-Racine, F.-Y., Abazajian, K. N., Hirata, C. M. (2016). Sterile neutrino dark matter: Weak interactions in the strong coupling epoch. *Phys. Rev. D*, *94*, 043515. doi:10.1103/PhysRevD.94.043515.

[142] Vitagliano, E., Tamborra, I., Raffelt, G. (2020). Grand unified neutrino spectrum at Earth: Sources and spectral components. *Rev. Mod. Phys.*, *92*, 045006. doi:10.1103/RevModPhys.92.045006.

[143] Whitehorn, N., van Santen, J., Lafebre, S. (2013). Penalized splines for smooth representation of high-dimensional Monte Carlo datasets. *Computer Physics Communications*, *184*(9), 2214–2220. ISSN 0010-4655. doi:https://doi.org/10.1016/j.cpc.2013.04.008.

[144] Wilks, S. S. (1938). The Large-Sample Distribution of the Likelihood Ratio for Testing Composite Hypotheses. *Annals Math. Statist.*, *9*(1), 60–62. doi:10.1214/aoms/1177732360.

[145] Wolfenstein, L. (1978). Neutrino oscillations in matter. *Phys. Rev. D*, *17*, 2369–2374. doi:10.1103/PhysRevD.17.2369.

[146] Woosley, S. E., Phillips, M. M. (1988). Supernova 1987A! *Science*, *240*(4853), 750–759. doi:10.1126/science.240.4853.750.

[147] Wu, D.-d. (1991). A brief introduction to the strong CP problem.

[148] Zatsepin, G. T., Kuz'min, V. A. (1966). Upper Limit of the Spectrum of Cosmic Rays. *Soviet Journal of Experimental and Theoretical Physics Letters*, *4*, 78.

[149] Zwicky, F. (1933). Die Rotverschiebung von extragalaktischen Nebeln. *Helv. Phys. Acta*, *6*, 110–127. doi:10.1007/s10714-008-0707-4.

[150] Zyla, P., *et al.* (2020). Review of Particle Physics. *PTEP*, *2020*(8), 083C01. doi: 10.1093/ptep/ptaa104. And 2021 update.